Half a century of satellite remote sensing of sea-surface temperature

P J Minnett, A Alvera-Azcárate, T M Chin, G K Corlett, C L Gentemann, I Karagali, X Li, A Marsouin, S Marullo, E Maturi, et al.

To cite this version:

P J Minnett, A Alvera-Azcárate, T M Chin, G K Corlett, C L Gentemann, et al.. Half a century of satellite remote sensing of sea-surface temperature. Remote Sensing of Environment, 2019, 233, 10.1016/j.rse.2019.111366 . meteo-03376392

HAL Id: meteo-03376392
https://meteofrance.hal.science/meteo-03376392v1

Remote Sensing of Environment 233 (2019) 111366

Contents lists available at ScienceDirect

Remote Sensing of Environment

journal homepage: www.elsevier.com/locate/rse

Half a century of satellite remote sensing of sea-surface temperature

P.J. Minnett[a,*], A. Alvera-Azcárate[b], T.M. Chin[c], G.K. Corlett[d], C.L. Gentemann[e], I. Karagali[f], X. Li[g], A. Marsouin[h], S. Marullo[i], E. Maturi[j], R. Santoleri[k], S. Saux Picart[h], M. Steele[l], J. Vazquez-Cuervo[c]

[a] Rosenstiel School of Marine and Atmospheric Science, University of Miami, 4600 Rickenbacker Causeway, Miami, FL 33149, USA
[b] AGO-GHER-MARE, University of Liège, Allée du Six Août 17, Sart Tilman, Liège, 4000, Belgium
[c] Jet Propulsion Laboratory, California Institute of Technology, 4800 Oak Grove Drive, Pasadena, CA 91109, USA
[d] EUMETSAT, Eumetsat Allee 1, D-64295 Darmstadt, Germany
[e] Earth & Space Research, 2101 4th Ave #1310, Seattle, WA 98121, USA
[f] DTU Wind Energy, Technical University of Denmark, Risø Campus, Frederiksborgvej 399, Roskilde 4000, Denmark
[g] IMSG at Environmental Modeling Center, National Center for Environmental Prediction, NOAA, 5830 University Research Court, College Park, MD 20740, USA
[h] CNRM, Université de Toulouse, Météo-France, CNRS, Lannion, France
[i] Italian National Agency for New Technologies, Energy and Sustainable Economic Development - ENEA - Division Models and Technologies for Risk Reduction - Laboratory for Climate Modelling - Centro Ricerche Frascati, Frascati, Italy
[j] NOAA/NESDIS/STAR, NOAA Center for Weather and Climate Prediction (NCWCP), 5830 University Research Court, Rm 3711, College Park, MD 20740, USA
[k] Consiglio Nazionale Ricerche - CNR - Institute of Marine sciences (ISMAR), Venezia, Italy
[l] Polar Science Center/Applied Physics Laboratory, University of Washington, 1013 NE 40th Street, Seattle, WA 98105, USA

ARTICLE INFO

Keywords:
Sea surface temperature
Fifty year review

ABSTRACT

Sea-surface temperature (SST) was one of the first ocean variables to be studied from earth observation satellites. Pioneering images from infrared scanning radiometers revealed the complexity of the surface temperature fields, but these were derived from radiance measurements at orbital heights and included the effects of the intervening atmosphere. Corrections for the effects of the atmosphere to make quantitative estimates of the SST became possible when radiometers with multiple infrared channels were deployed in 1979. At the same time, imaging microwave radiometers with SST capabilities were also flown. Since then, SST has been derived from infrared and microwave radiometers on polar orbiting satellites and from infrared radiometers on geostationary spacecraft. As the performances of satellite radiometers and SST retrieval algorithms improved, accurate, global, high resolution, frequently sampled SST fields became fundamental to many research and operational activities. Here we provide an overview of the physics of the derivation of SST and the history of the development of satellite instruments over half a century. As demonstrated accuracies increased, they stimulated scientific research into the oceans, the coupled ocean-atmosphere system and the climate. We provide brief overviews of the development of some applications, including the feasibility of generating Climate Data Records. We summarize the important role of the Group for High Resolution SST (GHRSST) in providing a forum for scientists and operational practitioners to discuss problems and results, and to help coordinate activities world-wide, including alignment of data formatting and protocols and research. The challenges of burgeoning data volumes, data distribution and analysis have benefited from simultaneous progress in computing power, high capacity storage, and communications over the Internet, so we summarize the development and current capabilities of data archives. We conclude with an outlook of developments anticipated in the next decade or so.

1. Introduction

Sea-surface temperature (SST) is a very important variable in the earth's climate system. Being at the interface of the ocean and the atmosphere, SST is critical to both, and to the exchanges of heat, moisture, momentum, and gases between the two (e.g. Bentamy et al., 2017; Wanninkhof et al., 2009). The patterns of SST reveal subsurface dynamics, at least those with a surface thermal expression such as fronts and eddies (e.g. Tandeo et al., 2014), and the modulation of the surface momentum exchanges across the temperature gradients modify

---

* Corresponding author at: Ocean Sciences, Rosenstiel School of Marine and Atmospheric Science, University of Miami, 4600 Rickenbacker Causeway, Miami, FL 33149, USA.

E-mail address: pminnett@rsmas.miami.edu (P.J. Minnett).

https://doi.org/10.1016/j.rse.2019.111366
Received 6 December 2018; Received in revised form 7 August 2019; Accepted 8 August 2019

Fig. 1. An extract of the Franklin-Folger Map of the currents of the North Atlantic showing the position of the strong surface current named here as the Gulf Stream. From the Library of Congress (https://www.loc.gov/resource/g9112g.ct000753/).

the atmospheric boundary layer on the mesoscale (e.g. O'Neill et al., 2010; Perlin et al., 2014) and larger (e.g. McPhaden et al., 2006; Minobe et al., 2008). Temporal changes in patterns of SST on the basin scales can reveal large-scale perturbations to the global circulation (Dong et al., 2018) and multi-decadal changes in the climate (e.g. Jha et al., 2014). Since all processes in nature exhibit a temperature dependence, variations in the SST influence many components of the climate, including the Ocean Primary Production (OPP; Behrenfeld and Falkowski, 1997; Behrenfeld et al., 2006), which is important to the flow of carbon through the global environment, and is the base of the ocean food web. Global sampling of the SST is feasible only from earth-observation satellites, with sensors on geostationary satellites providing rapid sampling in the tropics and mid-latitudes, and those on polar orbiting satellites generating global data but less frequently. Satellites in geostationary orbits rotate about the earth in the equatorial plane with a period equal to that of the earth's rotation on its axis, and thus appear to be at an approximately fixed longitude. The satellites are at about 35,900 km above the equator. Measurements from geostationary satellites sample diurnal changes. The term “polar-orbiting satellite” is often used as short-hand for “near-polar orbiting, sun-synchronous satellites”. Such satellites orbit the earth at a height of 700–800 km and have an inclination of ~98°, meaning when they cross the equator, they travel in the direction of ~98° measured from east. The choice of altitude and inclination is determined by the effects of the earth's equatorial bulge on its gravity field, and results in the plane in which the satellite orbits precessing in space once per year meaning the satellite passes overhead at a given latitude at about the same times in a day, once going north (in the ascending arc) and again going south (in the descending arc), hence the “sun-synchronous” aspect. This has the advantage that measurements of the same place are taken at about the same local time, but it means that diurnal changes are poorly resolved by a single satellite. Details of earth satellite orbits are given by Montenbruck and Gill (2000).

Since significant progress in knowledge and understanding are often stimulated by developments of new or improved instruments, we include a section on the development of satellite instruments and on improvements in the accuracy of the satellite retrievals of SST. The remarkable contributions these instruments have made to further our understanding of the oceans, air-sea interactions, and the climate system, are dealt with in a wealth of papers in the primary literature and in many books (e.g. Robinson, 2004; Robinson, 2010; Martin, 2014) and encyclopedias (e.g. Njoku et al., 2014).

In this review, a Historical Background section is followed by a discussion of the meaning of "SST" and a summary of the techniques of retrieving SST from measurments of satellite radiometers. The satellite radiometers used over the last half century are then presented, leading to a discussion of the instruments and approaches used to assess the accuracies of the satellite-derived SSTs. There follows a brief explanation of the various processing levels of the derived SSTs in which the data are delivered to users. Two regions, the Mediterranean Sea and the Arctic Ocean, are highlighted as examples of where deriving accurate SST retrievals is challenging but where satellite data have produced significant results. Three specific applications of satellite-derived SST with direct societal benefit are then briefly discussed: Numerical Weather Prediction, Ocean Heat Content and its relationship to severe storms, and sea-level rise. The relatively new field of Operational Oceanography, in which satellite-derived SSTs have immediate applications, is introduced, followed by the contribution of accurate SSTs from satellites to a longer term application, that of generating Climate Data Records. Synergistic analyses of satellite-derived SSTs with other remotely sensed data are then discussed. The role of the Group for High-Resolution SST (GHRSST) in coordinating research and operational applications of SST is presented before a discussion of the facilities at various data centers from where users can access satellite data. The review concludes with an outlook into anticipated developments in the foreseeable future.

For more information than is possible in this review, the interested reader is referred to, for example, Chapters 7 and 8 of Robinson (2004), Chapters 7 to 9 of Martin (2014), and Robinson (2010).

2. Historical background

It is generally accepted that one of the first depictions of a strong SST signal is the Franklin-Folger chart of the Gulf Stream published in 1768 (Fig. 1; Franklin et al., 1768). Benjamin Franklin, who was deputy Postmaster General of the American colonies and was based in London, had wondered why sailing ships going to America took longer than the ships coming from the colonies. His cousin, Timothy Folger, a whaling captain, told Franklin that this was because of the strong current flowing to the east and was well known to local navigators, but apparently not to captains of ships crossing the Atlantic Ocean. The temperature gradients at the sides of the "Gulf Stream," named in recognition of its origin in the Gulf of Florida, were known to be good areas for fishing and whaling (Lacouture, 1995). Although the Franklin-Folger chart is the first recognized graphical representation of the Gulf Stream, it had been remarked upon by the Spanish Explorer, Juan Ponce de León, in 1513 when he landed and named Florida, near present-day St. Augustine (Lacouture, 1995).

The history of knowledge about the analogous current in the Pacific Ocean, the Kuroshio, is much longer, going back to the seventh century (Kawai, 1998) with evidence of the current being based on flotsam and hapless castaways being washed up on islands having come from the south. The connection with SST was not made until much later, but was known by the mid-nineteenth century when mention of warm waters of the Kuroshio was made in ships' log books (Kawai, 1998).

The depiction of the Gulf Stream in the Franklin-Folger map is remarkably congruent with the mean position of the Gulf Stream, as now known, but the current is not constant in position or strength. Measurements taken from ships were indicative of a very spatially and temporally variable current, which defied simple representation as a synoptic feature (Fuglister, 1955; Fuglister, 1963); the same is true of the Kuroshio (Fuglister, 1955).

It was not until the advent of infrared (IR) remote sensing from satellites that the spatial complexity of the surface signature of the Gulf Stream was revealed (Legeckis, 1975). Infrared scanning radiometers on geostationary satellites were capable of making images of the earth's disk at half hourly intervals, even in the 1970s. These provided frequent images for compositing cloud-free sections over a day or so to reduce the obscuration of the sea surface by clouds over the Gulf Stream (Legeckis, 1975) and to reveal strong features elsewhere, such as Tropical Instability Waves in the eastern equatorial Pacific (Legeckis, 1977). But it was the higher resolution and superior sensitivity of IR radiometers on polar-orbiting satellites that gave a better depiction of the SST features, not only of the Gulf Stream (Legeckis, 1979), but of many other strong SST gradients associated with upper ocean currents and eddies (Legeckis and Gordon, 1982; Legeckis, 1978).

3. Sea-surface temperature

Although there have been marine observations since the mid-eighteenth-century (Worley et al., 2005) and there are records of the near-surface temperature for nearly two centuries using thermometers in a bucket of sea water hauled onto the deck of ships, it is generally recognized that the reliable time series of measurements began in the mid-1850s (Rayner et al., 2006). With time the measurement approaches improved and at about the same time as quantitative retrievals of SST from IR radiometers on satellites began, arrays of drifting buoys carrying thermometers and using satellite data transmission were being deployed in significant numbers. Subsurface temperatures from these buoys were used to assess the accuracy of the satellite-derived SSTs, and while differences had a standard deviation of ~0.5 K (McClain et al., 1985), details of the vertical structure of the near-surface temperature could be ignored. But, as the differences between satellite-derived SSTs and in situ measurements diminished, the temperature structure took on a new importance.

Although SST is not a single variable, it is considered by many to be the temperature within the mixed layer (approximately the upper 10 m). Air-sea fluxes of heat, moisture and momentum, as well as ocean turbulence means the temperature variation through the "mixed layer" can be complex and variable. This complexity and variability need to be considered when comparing or combining measurements of SST from different satellites and in situ sensors. To facilitate such activities, a set of definitions of SST were developed by the GHRSST Science Team (Section 13). These definitions achieve the closest possible agreement between what is defined and what can be measured, taking into account our current understanding of near surface thermal variability. The definitions are in agreement with the Climate and Forecast (CF) metadata convention and are now used across GHRSST-format SST products. The definitions are shown schematically in Fig. 2 and are briefly summarized below. Further details on their derivation are discussed by Minnett and Kaiser-Weiss (2012).

Five different SST definitions are specified: (1) The interface temperature (SST_{int}) – the temperature at the air-sea interface on molecular scales; (2) the skin sea surface temperature (SST_{skin}) - the temperature measured by an IR radiometer typically operating at wavelengths 3.7–12 μm (chosen for consistency with the majority of IR satellite measurements), which represents the temperature within the conductive diffusion-dominated sub-layer at a depth of ~10–20 μm; (3) the subskin sea surface temperature ($SST_{subskin}$) - the temperature at the base of the conductive laminar sub-layer of the ocean surface, which for practical purposes can be well approximated to the measurement of surface temperature by a microwave radiometer operating in the 6–11 GHz frequency range; (4) the surface temperature at depth (SST_z or SST_{depth}) - all measurements of water temperature beneath $SST_{subskin}$; and (5) the foundation temperature (SST_{fnd}) - the temperature free of diurnal temperature variability, i.e., SST_{fnd} is defined as the temperature at the first time of the day when the heat gain from the solar radiation absorption exceeds the heat loss at the sea surface.

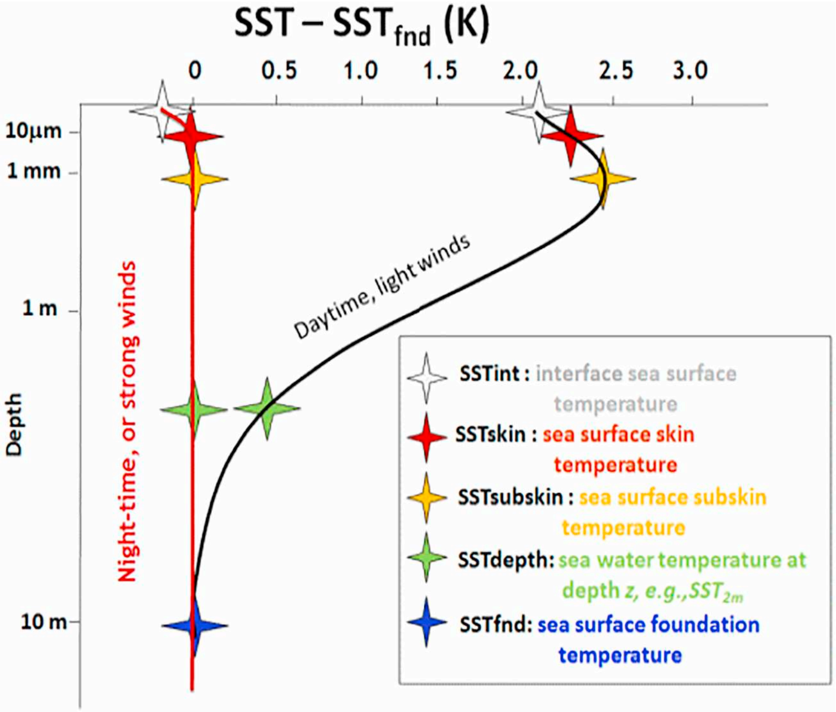

Fig. 2. Near-surface oceanic temperature gradients. From Minnett and Kaiser-Weiss (2012).

3.1. *Thermal skin effect*

The ocean surface is nearly everywhere and under nearly all conditions warmer than the atmosphere in contact with it, resulting in a heat flow from the ocean to atmosphere. The upwards flow of heat in the water is accomplished in the top hundred micrometers or so of the water (Wong and Minnett, 2018) by molecular conduction as the air-sea density difference and near surface viscous layer on the aqueous side of the interface suppress the turbulent heat transfer (Soloviev and Lukas, 2014). Thus, there is a vertical temperature gradient in the water just beneath the interface leading to decreasing temperature closer to the interface; this is referred to as the thermal skin layer. The IR emission from the sea surface emerges from a thin layer, an electromagnetic skin layer, that is of comparable thickness in the IR (Bertie and Lan, 1996) to the thermal skin layer (Wong and Minnett, 2018). The radiance emitted by the sea surface and measured by an IR radiometer is nearly always characteristic of a temperature lower than that measured by an in situ thermometer (Donlon et al., 2002; Minnett et al., 2011). The average temperature drop across the thermal skin layer is ~0.17 K, with much larger values seen at very low winds (ibid), so, given the target accuracy of satellite-derived SSTs for climate change studies of 0.1 K (Ohring et al., 2005), the variable thermal skin effect should be taken into account, and retrievals of SST in the IR should be considered as SST_{skin}. The electromagnetic skin depths at microwave frequencies used to derive SST are greater (see Fig. 2 of Minnett and Kaiser-Weiss, 2012) so even though the thermal skin layer is embedded in the microwave electromagnetic skin layer, the microwave-derived SST is not an SST_{skin} and can be considered as an approximation to $SST_{subskin}$.

3.2. *Diurnal variability*

A significant part of the solar radiation entering the ocean is absorbed at the top few meters. During day-time and in the absence of strong enough winds to drive vertical mixing of heat, diurnal warming causes a relatively shallow warm layer to be formed (Fig. 2).

Driven by solar heating, diurnal variability of SST occurs under moderately low wind speeds in all ocean basins. While in situ observations provided the first reported cases of diurnal variability (e.g. Stommel et al., 1969; Halpern and Reed, 1976; Kaiser, 1978), SST retrievals from space resulted in a significant increase of diurnal cycle characterization and understanding. Diurnal warming has been identified in the Arctic (Eastwood et al., 2011), the North and Baltic Sea (Karagali et al., 2012), various regions of the Atlantic Ocean (Fig. 3; Cornillon and Stramma, 1985; Stramma et al., 1986; Price et al., 1987; Gentemann and Minnett, 2008; Le Borgne et al., 2012a; Karagali and Høyer, 2014), the Mediterranean Sea (Deschamps and Frouin, 1984; Böhm et al., 1991; Buongiorno Nardelli et al., 2005; Merchant et al., 2008a; Marullo et al., 2014a), the Tropics (Clayson and Weitlich, 2007; Marullo et al., 2010) and Tropical Warm Pool (Zhang et al., 2016a; Zhang et al., 2016b), the Gulf of California (Flament et al., 1994; Ward, 2006), the Indian and South Pacific Ocean (Gentemann and Minnett, 2008) and the Arabian Sea (Stuart-Menteth et al., 2005b). Advances in space-borne SST retrievals allowed basin-scale studies of diurnal warming spanning several years and extended comparisons with in situ observations (Stuart-Menteth et al., 2003; Gentemann and Minnett, 2008; Castro et al., 2014; Karagali and Høyer, 2014), with detailed characterization of number of occurrences, peak warming time and seasonal patterns. The abundance of SST retrievals from space and improvements in understanding of the diurnal cycle allowed for numerical simulations to reproduce the diurnal variability of the upper ocean layer, first developed shortly after the first observational evidence was reported. Based on parameterizations of solar heating of the upper ocean (Woods et al., 1984), Woods and Barkmann (1986) modeled the response of a layered ocean to daily and seasonal modulation of solar heating. Price et al. (1986) developed a mixed layer model using observational evidence from a measurement campaign. A simplified version of this model was developed a decade later by Fairall et al. (1996) and similar approaches were adopted by Zeng and Beljaars (2005), Schiller and Godfrey (2005), and Gentemann et al. (2009). A simpler approach to reproducing the diurnal variability was adopted through parameterizations derived from wind and surface warming observations (Webster et al., 1996; Clayson and Curry, 1996; Kawai and Kawamura, 2002; Gentemann et al., 2003; Stuart-Menteth et al., 2005a; Filipiak et al., 2010). A selection of these models has been

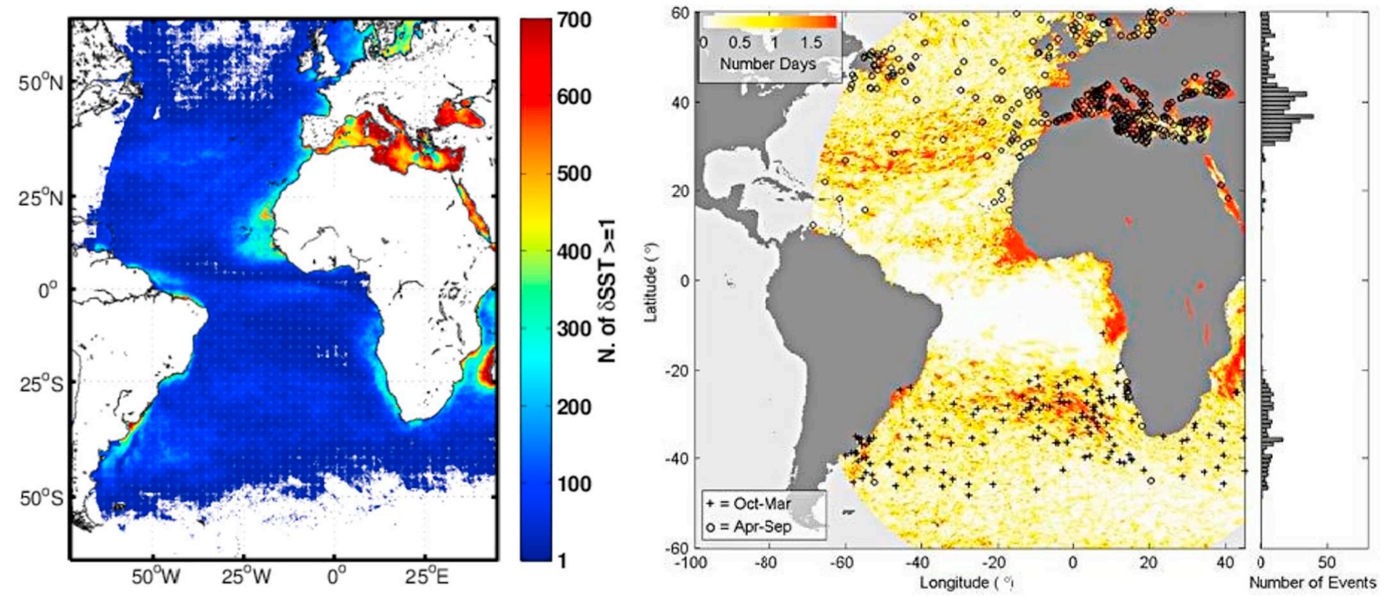

Fig. 3. Left: Spatial extent of hours of diurnal heating of SST ≥ 1 K (defined as the difference between a given daytime hourly SST value and the corresponding foundation temperature of the previous night) from SEVIRI hourly retrievals for 2006–2011. White areas indicate zero occurrences. After Karagali and Høyer (2014). Right: Location of diurnal events over 5 K (black '+' and 'o'). Events generally occur in the summer. The background color shows the days in a year (on average) that wind speed was < 1 $\mathrm{m\,s^{-1}}$ at 14:00 LMT. From Gentemann et al. (2008) with permission.

intercompared in various regions (Karagali and Høyer, 2013; Zhang et al., 2018). Furthermore, turbulence closure models solving the equations for the distribution of heat, momentum, and salt across the water column, have been found to successfully reproduce diurnal SST signals (Kantha and Clayson, 1994; Hallsworth, 2005; Karagali et al., 2017). Identification and characterization of diurnal variability in all ocean basins promoted not only attempts for its numerical simulation but also impact studies to assess the importance of accounting for the formation of diurnal warm layers in large scale modelling systems. The implications associated with the lack of a properly resolved SST daily cycle in atmospheric, oceanic and climate models have been evaluated in terms of heat budget errors in the Tropics (Danabasoglu et al., 2006; Bellenger and Duvel, 2009; Ham et al., 2010; Clayson and Bogdanoff, 2013), the Mediterranean Sea (Marullo et al., 2016), and the North Sea (Fallmann et al., 2017).

4. Satellite retrieval of sea-surface temperature

The spectral distribution of radiation emitted by the sea surface at absolute temperature, T, is given by Planck's Function:

$$B_\lambda(T) = 2hc^2\,\lambda^{-5}(e^{hc/(\lambda kT)} - 1)^{-1} \tag{1}$$

where h is Planck's constant, c is the speed of light in a vacuum, k is Boltzmann's constant, and λ is the wavelength. Planck's Function is for a perfectly emitting surface, a blackbody, whereas all natural surfaces emit imperfectly with the ratio of emitted radiance to Planck's Function being the emissivity, ε, which is a function of the wavelength of the emitted radiation and the angle of emission relative to normal to the surface, θ. The tilting of the facets of the sea surface by wind generated waves (Cox and Munk, 1954) introduces an apparent wind speed dependence of ε (Hanafin and Minnett, 2005; Nalli et al., 2008b; Nalli et al., 2008a). The emissivity of seawater at IR wavelengths where measurements of SST are made is high (~0.985 at $\lambda = 10\,\mu$m at an emission angle of 40° and 0.970 at 55°; Hanafin and Minnett, 2005) and exhibit small apparent wind speed dependence, at least for emission angles < 60°. An important property of Planck's Function is that the emitted radiance at any wavelength increases as the emitting temperature increases. Thus, a measurement of radiance at a known wavelength can be used to derive the emitting temperature through Eq. (1).

4.1. SST retrievals in the infrared

The temperatures derived from the radiance measurements of satellite radiometers, using Planck's Function (Eq. (1), modulated by the spectral response of the radiometer), are called brightness temperatures, and because of the effects of the intervening atmosphere these are not the same as would be measured by a radiometer of comparable accuracy just above the sea surface. The initial step in deriving SST from brightness temperatures requires the confident identification of pixels that include radiance from clouds, or aerosols, before clear-sky atmospheric correction algorithms can be applied.

4.1.1. Atmospheric transmission

As the IR radiation propagates through the atmosphere to reach the satellite sensors, the photons may interact with the components of the atmosphere. As in the visible, IR radiation does not propagate unhindered through clouds, and, even in cloud-free conditions, the photons can be absorbed or scattered by molecules and aerosols, and the atmospheric components emit photons into the beam that reaches the satellite radiometer. The transmissivity of the clear-sky atmosphere in the IR is very variable with wavelength and with the concentrations of atmospheric gases. The term "atmospheric window" is used to describe wavelength intervals where the atmosphere is relatively transparent and it is measurements by satellite radiometers in these intervals that permit the estimation of SST from top-of-atmosphere measurements.

In the IR, the peak of Planck's Function at temperatures typical of the SST is close to $\lambda = 10\,\mu$m, where the atmosphere is relatively transparent. Fig. 4 shows the spectral dependence of the atmospheric transmission for three characteristic atmospheres derived from a radiative transfer model with relatively coarse spectral resolution. The lower panel of Fig. 4 shows the spectral radiance calculated for four temperatures - 0, 10, 20, and 30 °C with the relative spectral response functions (RSRs), normalized to a maximum value of 1 for five bands of the MODerate-resolution Imaging Spectroradiometer (MODIS, see Section 5.1.4) on the *Aqua* satellite. The RSRs are defined by transmission filters and the responsivity of the detectors. The spectrum of the radiance measured at the top of the atmosphere depends on the product

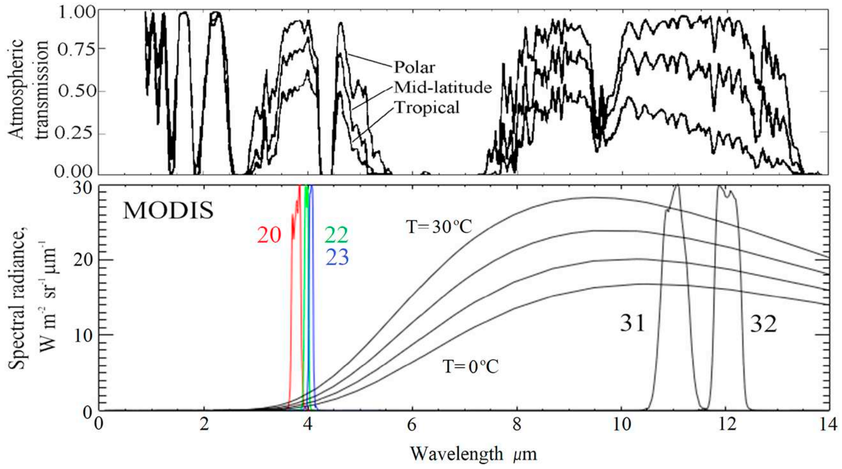

Fig. 4. Spectral dependence of the atmospheric transmission for wavelengths of electromagnetic radiation from about 1 to 14 µm, for three characteristic atmospheres (above), and (below) the black-body emission for temperatures of 0, 10, 20 and 30 °C, and the relative spectral response functions of the bands of MODIS on Aqua used to derive SST. The upper panel is adapted from Llewellyn-Jones et al. (1984) and the lower panel is taken from Kilpatrick et al. (2015).

of the value of the RSR, the intensity of the emitted radiance at the sea surface, and the atmospheric transmission at each wavelength. The signal generated is the integral across wavelength of the top-of-atmosphere spectrum. A second atmospheric window used for IR remote sensing of SST is in the mid-IR between $\lambda = 3.5$ to 4.1 µm. At these wavelengths, the signal is much smaller than in the "thermal infrared" at $\lambda = 9.5$–13 µm, but the sensitivity to changes in temperature is much higher, giving these measurements advantage for accurate and sensitive SST estimation. However, the low radiance means these measurements are very susceptible to contamination by reflected and scattered solar radiation and so SST can only be derived using measurements in the mid-IR window when conditions limit solar effects, which usually means only at night.

The transmission of dry, cold polar atmospheres is high in both transmission windows, but as the water vapor increases, the transmission decreases so that more of the signal originates in the atmosphere and less at the surface. Fig. 4 shows in broad terms the regional variations in the clear-sky atmospheric transmission, but there are significant seasonal variations at any location. An example of seasonal variations is given in Fig. 5, which shows the atmospheric transmission spectra in the 10–12 µm range derived by a high spectral resolution radiative transfer model (Závody et al., 1995). The atmospheric water vapor and temperature profiles were those measured by radiosondes launched from Ocean Weather Ship Mike at 66°N, 2°E in February (left) and in July (right). The February conditions are very dry and cold, and the atmospheric transmission is high; the narrow lines to lower transmission are the signatures of quantized molecular absorption of photons propagating upwards. The July conditions are moister and while the same line absorption is apparent, the baseline is not at high transmission as in February and shows a gradient with wavenumber. This baseline transmission is caused by the anomalous water vapor continuum absorption (Shine et al., 2012).

4.1.2. Cloud screening

Clear sky conditions are required for the derivation of SST from IR measurements so the identification and exclusion of cloud-contaminated pixels is critical for accurate retrievals. Historically, identification of clouds in IR measurements from satellites has been driven primarily by binary tests in a decision tree based on brightness temperature (BT) uniformity, BT minima, and comparisons with lower-resolution gap-free reference fields (Kilpatrick et al., 2001; Kilpatrick et al., 2015). The efficacy of these tests often decreases near ocean thermal fronts, at cloud edges, in the presence of small cirrus clouds, and low-level, uniform stratus clouds when cloud temperature can be close to that of the sea surface particularly at high latitudes. This reliance on stringent uniformity thresholds often has the unintended consequence of misidentifying strong SST frontal regions as clouds. Differences in detecting clouds between day when visible reflectance can be used and at night, when it cannot, lead to systematic erroneous irregularities in the cloud masks (Liu and Minnett, 2016; Liu et al., 2017).

An alternative, probabilistic approach to cloud identification in IR imagery based on Bayes' Theorem was developed by Merchant et al. (2005). Joint probability distributions of BTs in two IR channels were

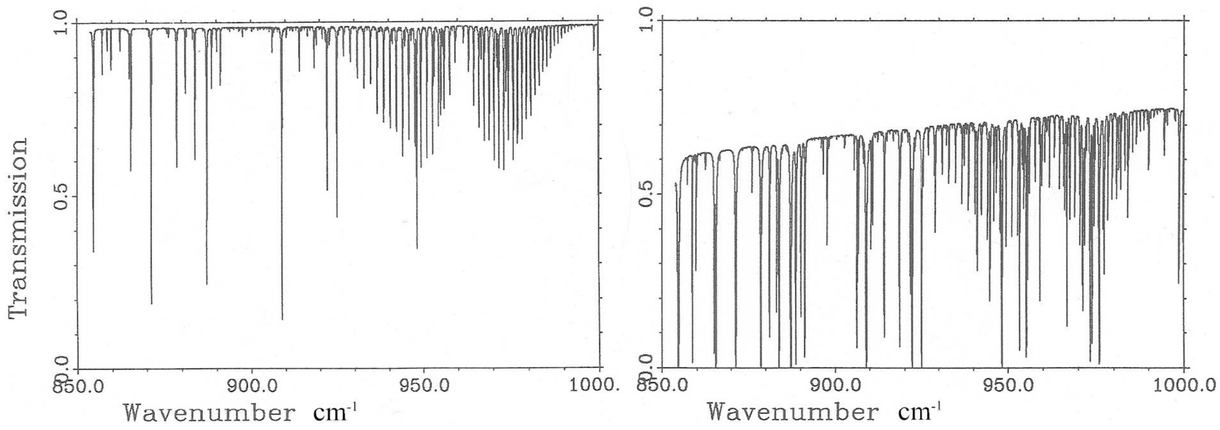

Fig. 5. Simulated spectra of atmospheric transmission in the thermal IR transmission window for dry winter conditions (left) and moister summer conditions (right) at the same location (66°N, 2°E) in the Norwegian Sea. The atmospheric conditions were given by radiosondes. Note the units on the abscissa are in wavenumber units; 850 cm^{-1} corresponds to $\lambda = 12$ µm and 1000 cm^{-1} to $\lambda = 10$ µm.

derived by radiative transfer simulations in clear sky conditions, and of cloudy conditions by visual inspection of satellite imagery. Radiative transfer simulations with weather prediction model output to give the atmospheric state are used to give an expectation of clear-sky BTs which are compared with probability distributions of cloudy measurements, the measured BTs are assigned a probability of having been influenced by clouds. This approach has been widely used for several satellite missions including for the (A)ATSR ((Advanced) Along-Track Scanning Radiometer) series (Merchant et al., 2012), the NOAA GOES (Geostationary Operational Environmental Satellite; Maturi et al., 2008), and Himawari-8 satellite (Kurihara et al., 2016) of the Japan Meteorological Agency (JMA).

To address the specific cases where the decision-tree approach to cloud screening resulted in erroneous classification (Liu and Minnett, 2016; Liu et al., 2017), a new algorithm has been developed, called the Alternating Decision Tree (ADT) (Freund and Mason, 1999; Kilpatrick et al., 2019). Unlike in the decision-tree approach where a pixel identified as being cloud-free has to pass every test, in the ADT the output of each test is considered in determining the likelihood of a pixel being identified as being clear or cloudy. The threshold values and the weighting given to each test were determined by a Machine Learning algorithm (Hall et al., 2009) applied to a subset of matchup data in four conditions: night-time, daytime, moderate sun-glitter and strong sun-glitter. When applied to MODIS and VIIRS (Visible and Infrared Imaging Radiometer Suite; see Section 5.1.6) data, the ADT algorithm improves on the decision-tree approach for all metrics considered (Kilpatrick et al., 2019).

4.1.3. *Correction of clear-sky atmospheric effects*

The differential atmospheric transmission across the "atmospheric windows" at $\lambda = 3.5–4.1\,\mu m$ and $\lambda = 9.5–12.5\,\mu m$ were recognized early on as a potential mechanism for providing a correction for the effect of the cloud-free atmosphere (McMillin, 1975). By placing two distinct spectral channels in a window, the BT measured in each would be different, being lower in the channel with lower atmospheric transmissivity, and the BT difference would be indicative of the attenuation of the IR signal intensity, caused primarily by water vapor in the $\lambda = 9.5–12.5\,\mu m$ window but which is much less influential in the shorter wavelength window. Linearization of Planck's Function and the radiative transfer equation leads to a simple expression in which the BT difference is related to the drop in temperature from the SST_{skin} and one of the BTs (McMillin and Crosby, 1984; McMillin and Crosby, 1985; Barton, 1995):

$$SST = aT_i + \gamma\,(T_i - T_j) + c \tag{2}$$

where T_i and T_j are the BTs measured in the two channels, c is an offset, and γ is the "differential absorption" coefficient of McMillin (1975). Eq. (2) is called the Multi-Channel SST (MCSST) algorithm. The coefficients are dependent on the atmospheric state at the time of the measurement, particularly the profiles of temperature and water vapor, and can be determined by a simple regression analysis of collocated, coincident measurements (matchups) of BTs and in situ measurements, or by using radiative transfer simulations. The statistical approach requires a large number of matchups in conditions that sample the global atmospheric and SST variability (McClain et al., 1985). The temporal and spatial variability of the SST fields are inherent in the matchups. To limit undesirable consequences in determining both the coefficients in the MCSST and the accuracy of the retrieved SSTs, restricted time and spatial intervals are applied: typically 10 km and less than an hour (Minnett, 1991). The radiative transfer approach to determine the coefficients requires an accurate radiative transfer model to predict the spectra of the emitted IR radiation at the satellite height (Závody et al., 1995) through a representative set of atmospheric profiles, generally derived from radiosonde profiles (Minnett, 1986; Minnett et al., 1987), modulated by the relative spectral response function of the channels of the IR radiometer in question to produce simulated BTs (Llewellyn-Jones et al., 1984).

Missing from the MCSST algorithm is provision for the effects of increasing path lengths. This was subsequently accommodated by adding a term of the form $(\sec(\theta) - 1)$, where θ is the satellite zenith angle measured at the surface, scaled by an additional coefficient. The characteristic of the errors in the derived SSTs indicated a regional dependence on the split window brightness temperature differences suggestive that this difference is not sufficiently accurate in representing the effects of water vapor. Given that there is a strong correlation between the atmospheric water vapor content and SST, scaling the differential absorption coefficient with SST produced a very robust algorithm called the Non-Linear SST algorithm (Walton et al., 1998; Walton, 2016), which is based on the slightly non-linear combination of top-of-atmosphere brightness temperatures measured in the 10–12 μm wavelength interval where the atmosphere is relatively transmissive:

$$\begin{aligned} SST = {} & a_0 + a_1 * T_{11} + a_2 * (T_{11} - T_{12}) * T_{sfc} + a_3 * (\sec(\theta) - 1.0) \\ & * (T_{11} - T_{12}) \end{aligned} \tag{3}$$

where T_n are brightness temperatures measured in the channels at n μm wavelength, and T_{sfc} is a 'first guess' estimate of the SST in the area.

While Eq. (3) can be used both during day and night, more accurate night-time retrievals are feasible using the measurements in the mid-IR transmission window. For sensors such as VIIRS, the night-time algorithm takes the form:

$$SST_{triple} = a_0 + a_1 * T_{11} + a_2 * (T_{3.7} - T_{12}) * T_{sfc} + a_3 * (\sec(\theta) - 1) \tag{4}$$

For MODISs, which have two narrow bands in the mid-IR transmission window, the most accurate night-time algorithm has been found to be:

$$SST4 = a_0 + a_1 * T_{3.95} + a_2 * (T_{3.95} - T_{4.05}) + a_3 * (\sec(\theta) - 1) \tag{5}$$

where the symbols have the same meaning as in Eq. (3) but coefficients a_0–a_3 are of course different (Kilpatrick et al., 2015).

More complex forms of the atmospheric correction algorithm have been developed using additional channels, such as $\lambda = 8.6\,\mu m$ (Petrenko et al., 2014).

There are two approaches for deriving the coefficients: numerical simulations of the BT measurements (Llewellyn-Jones et al., 1984), and collocated and contemporaneous match-ups with in situ measurements (Kilpatrick et al., 2001; Kilpatrick et al., 2015). To attempt to accommodate the seasonal and regional variations in the atmospheric water vapor distributions, sets of coefficients that depend on month of the year and latitude bands can be used (Minnett, 1990; Kilpatrick et al., 2001; Kilpatrick et al., 2015.). Since the information about the atmospheric water vapor is contained in the BT differences, for radiometers with large NEΔT (Noise Equivalent Temperature Difference) or large digitization noise, the difference itself may be very noisy. Smoothing over a cluster of pixels, such as the clear-sky pixels in a 5 × 5 pixel array, improves the accuracy of the SST retrievals even at full resolution, making use of the fact that atmospheric properties generally change over longer distances than those of the SST (Barton, 1989; Coll et al., 1993). Indeed, in conditions of a very dry atmosphere, such as in the Arctic, the brightness temperature difference may be dominated by noise, and a single channel correction may be more effective (Vincent et al., 2008b).

The statistical approach to atmospheric correction generally works well when the conditions for a particular retrieval are close to the mean of those that are used to derive the coefficient set, but in conditions that deviate from these, such as at high latitudes, errors tend to be larger (Szczodrak et al., 2014). An approach that makes specific use of the atmospheric conditions was pioneered by Merchant et al. (2008b) using an Optimal Estimation (OE) approach in which the prior information about the expected state of a system is represented by a state vector $\mathbf{x_a} = (SST_{skin}, TWV)$ where TWV is total atmospheric column water

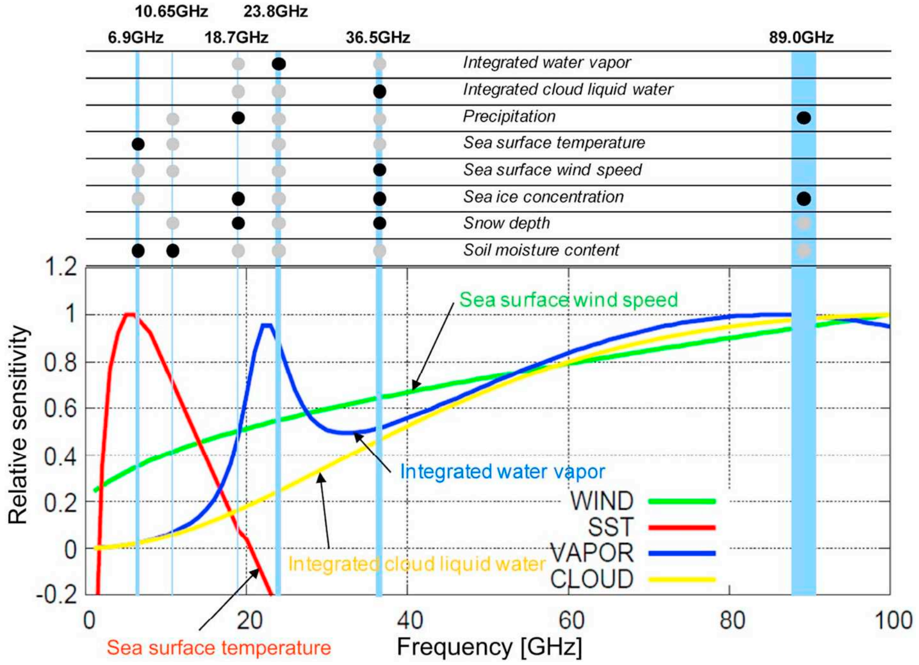

Fig. 6. Schematic of relative sensitivity in BT (normalized by the maximum value) for some geophysical parameters for measurements at an incidence angle of 55° as a function of frequency. Typical primary and secondary frequency bands for retrieving each geophysical parameter are shown by black and gray circles. Note that atmospheric contribution was neglected for ocean surface parameters, and oxygen absorption was not included for atmospheric parameters. From Imaoka et al. (2010), with permission.

vapor. The a priori values of SST_{skin} and TWV can be taken from a number of sources, including weather forecast models, or reanalysis fields such as from ECMWF. Vector $\mathbf{x_a}$ constitutes an input to a forward model F to simulate "prior observations" $\mathbf{y_a} = \mathrm{F}(\mathbf{x_a})$. The model F is generally a radiative transfer model and the prior observations are calculated radiances in the satellite radiometer channels. These simulated radiances are then adjusted to match the measured channel radiance within uncertainties determined by the radiometer characteristics, primarily the NEΔT and other residual instrumental artifacts if present. The adjustment is an inverse problem, as discussed by Rodgers (2000) and followed by Merchant et al. (2008b) and Merchant et al. (2009c):

$$\hat{\mathbf{z}} = \mathbf{z}(\mathbf{x_a}) + (\mathbf{K}^T\mathbf{S}_\varepsilon{}^{-1}\mathbf{K} + \mathbf{S_a}{}^{-1})^{-1}\,\mathbf{K}^T\mathbf{S}_\varepsilon{}^{-1}(\mathbf{y_o} - \mathbf{F}(\mathbf{x_a})) \tag{6}$$

where $\hat{\mathbf{z}}$ is a two-element vector containing the retrieved $\mathrm{SST_{skin}}$ and TWV. The matrix of partial derivatives (or the Jacobian), **K**, for the state vector is defined by:

$$\mathbf{K} = \left[\frac{\partial F(x_a)}{\partial z}\right] = \begin{bmatrix} \partial y_i/\partial x_1 & \partial y_i/\partial x_2 \\ \partial y_j/\partial x_1 & \partial y_j/\partial x_2 \end{bmatrix} \tag{7}$$

$\mathbf{S}_\varepsilon$ is the combined covariance matrix of the prior and satellite observations, and $\mathbf{S_a}$ is the covariance matrix of the two element prior reduced state vector. Merchant et al. (2008b) assumed the covariance matrices to be diagonal. Application of the OE atmospheric correction to MODIS data, using the Line-by-Line Radiative Transfer Model (LBLRTM) of Clough et al. (2005) and atmospheric state vectors derived from the ERA-Interim reanalysis fields of the ECMWF (Dee et al., 2011), resulted in SST retrieval accuracies that were better than those of the standard NLSST correction, but not for all retrievals that were not identified as highest quality, meaning confidently cloud-free, and for satellite zenith angles < 45° (Szczodrak, 2017; pers. com).

A further development of the physical retrieval method to correct for the effects of the intervening atmosphere has recently been developed by Koner et al. (2015). Called the Modified Total Least Squares (MTLS) method, it builds on earlier work to derive trace gas concentrations from satellite measurements (Koner and Drummond, 2008). The technique has been applied to SST retrievals from the GOES-13 imager (Section 5.4.3) (Koner et al., 2015) and to MODIS on Aqua (Koner and Harris, 2016), and produces satellite-derived SSTs that compare better with drifting buoy measurements than those derived using other approaches.

4.2. SST retrievals in the microwave

Planck's Function (Eq. (1)) gives the spectral distribution of radiance emitted by a blackbody at a given temperature; it is highly nonlinear in wavelength. But, at long wavelengths, where $hc \ll \lambda kT$, spectral radiance is a linear function of wavelength and using a Taylor expansion, Planck's Function reduces to the Rayleigh-Jean Law:

$$T = \lambda^4 B_\lambda(T)\,(2kc)^{-1} \tag{8}$$

As in the IR, the $B_\lambda(T)$ measured by passive microwave radiometers is related to the thermodynamic temperature (T) by the emissivity $\varepsilon(\lambda)$:

$$B_\lambda(T) = \varepsilon(\lambda)T \tag{9}$$

As the radiation passes through the atmosphere it is absorbed, scattered, and re-emitted, so the satellite measurement is:

$$\begin{aligned} &B_\lambda(T)\\ &\quad= \text{surface emission} + \text{atmospheric emission}\\ &\qquad+ \text{atmospheric emission reflected at the sea surface} + \text{emission from the surface,}\\ &\text{atmosphere and space scattered by the atmosphere} + \text{surface reflected space emission} \end{aligned}$$

A wind-speed dependent effective emissivity can also account for wave shadowing and surface emission being reflected from another facet of a roughened surface (Nalli et al., 2008a; Nalli et al., 2008b). The $B_\lambda(T)$ signal measured in the range of microwave frequencies used for earth observation depends on several varying parameters, including but not restricted to SST (Fig. 6).

Algorithms for deriving SST from passive microwave (PMW) measurements fall into two primary types, radiative transfer model (RTM) based algorithms and statistical algorithms. RTM simulations require instrument information (azimuth and earth incidence angles, frequency, polarization) and environmental data (SST, sea surface salinity, wind speed, wind direction, atmospheric profiles of temperature, pressure, water vapor density, and liquid cloud water density) to simulate the top of atmosphere (TOA) BTs.

Comparisons of the simulated and measured TOA BTs normally result in differences that can be attributed to errors in the RTM parameterizations or measurement errors (imperfect calibration, channel contamination, etc.), which require 'ad-hoc' corrections to the geophysical retrievals (Hilburn, 2009; Meissner and Wentz, 2012). The statistically based algorithms differ in that some of the calibration issues (up to ~1 K) or instrument issues may be accounted for by the nature of the statistical algorithm which is developed using satellite TOA BT measurements collocated with in situ and model observations (Shibata, 2006; Pearson et al., 2018; Nielsen-Englyst et al., 2018).

Both types of algorithms have their strengths and weaknesses. RTM-based algorithms clearly tie the physics of the observation to the geophysical retrieval allowing for identification of instrument calibration errors, and have a clear development path forward to improve future retrievals. Additionally, these algorithms can be used to develop realistic error models, but such error estimates depend on the accuracy of the model and the data used to derive it. Statistically based algorithms are simpler to implement and can be more accurate as the coefficient derivation process can account for errors in calibration or other offsets in channel temperatures.

Regardless of the algorithm type used to determine SST, removing erroneous data from the satellite retrievals ensures that the drived SSTs and the estimated errors are accurate. Cases where the satellite PMW SST retrievals are contaminated by radio-frequency interference (RFI) from ground-based sources, geostationary satellites, and communication satellites, need to be identified and flagged as being untrustworthy (Gentemann and Hilburn, 2015). Cases where the SST retrievals are affected by rain, strong winds, sea ice, sunglint, and being near land or sea ice as these retrievals have contributions from emission that enter through the antenna sidelobes, must also be identified and flagged. Precipitation, wind speed, and sea ice are geophysical variables derived from the same PMW measurements and these are used to flag erroneous SST values. The extent of sidelobe contamination is determined by calculating the distance to land or sea ice. Sunglint effects are present when the specular reflection angle is within 20–25° (depending on wind speed) of the solar angle at the surface. RFI can be difficult to identify, and the effects are usually identified using a mix of known ground-station locations and observation reflection vectors to known geostationary satellite emitters. Satellite to satellite RFI can be identified using a double difference method or estimated retrieval errors (Gentemann et al., 2010; Gentemann and Hilburn, 2015).

PMW SSTs have been retrieved from the Tropical Rainfall Measuring Mission (TRMM) Microwave Imager (TMI; Section 5.5.2) from December 1997 to 2015, but the low-inclination orbit limited retrievals to < 40° latitude. From June 2002–2011, Aqua's Advanced Microwave Scanning Radiometer - Earth Observing System (AMSR-E; Section 5.5.3) provided global PMW SST observations. From 2003, WindSat (Section 5.5.4) also measured PMW SST, and was joined by AMSR-2 (Section 5.5.7) in 2012, and Global Precipitation Mission (GPM) Microwave Imager (GMI; Section 5.5.8) in 2014. These last three radiometers are still in operation, but beyond their expected lifespan. The radiometers are described in more detail below.

4.3. SST sensitivity

The main focus of the development of SST retrieval algorithms has been to improve the absolute accuracy of the retrievals, but another important aspect is how well the derived SST fields represent local or larger scale spatial variability, or time series of retrieved SSTs represent time changes, such as diurnal warming and cooling. An ideal retrieval scheme would have zero sensitivity to water vapor variations, and a sensitivity to changes in the SST of unity. However, retrieval algorithms are imperfect and these targets are not achieved.

The sensitivities may be determined by radiative transfer modelling to simulate the satellite measurements through prescribed atmospheric conditions and surface temperatures, which can be adjusted in numerical experiments. As expected, the SST sensitivity to water vapor is dependent on the vapor distribution, being greater in the tropics and equatorial regions (Merchant et al., 2009b), and on the water vapor distribution in the vertical (Minnett, 1986). Using the AVHRR (Section 5.1.2) Pathfinder dataset (Kilpatrick et al., 2001), Merchant et al. (2009b) demonstrated that in nearly all cases the sensitivity of retrieved SST to actual SST variation is < 1.0, with the global average being 0.93. The minimum sensitivity was found to occur where atmospheric water vapor column content is high, specifically in the equatorial Atlantic and Pacific Oceans, especially the Tropical Warm Pool where the sensitivity may be < 0.5.

Similarly, estimates of the amplitude of diurnal heating deduced from satellite-derived SST may be smaller than the real amplitude if the temporal sensitivity of the satellite data is < 1.0 (Merchant et al., 2009b; Merchant et al., 2013). Zhang et al. (2018) compared diurnal heating signals in the Tropical Warm Pool region in geostationary satellite measurements from the Multifunctional Transport Satellite-1R (MTSAT-1R; Puschell et al., 2002) with in situ measurements from drifting buoys (Section 6) from the In situ SST Quality Monitor (iQuam) data set (Xu and Ignatov, 2014; https://www.star.nesdis.noaa.gov/sod/sst/iquam/), which, with measurements at a depth of ~20 cm, were taken to be a good representation of the real diurnal heating amplitude (Gentemann et al., 2009). The resulting estimate of the satellite-derived SST sensitivity was found to be 0.60 (± 0.05), meaning that remotely-sensed diurnal heating amplitudes in the Tropical Warm Pool are significantly underestimated.

5. History of instrument development

Throughout the history of science, major advances in knowledge and understanding of phenomena have followed new measurements, often taken using new or improved instruments. The development of satellite oceanography, including the derivation of SST fields from spacecraft is no exception.

There are several common characteristics of satellite scanning radiometers used to derive quantitative measurements of SST: a mechanism to generate imagery - a rotating plane mirror in the IR or a rotating offset-paraboloid reflector in microwave radiometers; effective detectors; and a process for real-time, in-flight calibration of the measurements. Both rotating mirrors and reflectors direct the IR or microwave radiation into the radiometers. Calibration is based on measurements of two targets at known temperatures, one of which is often cold space on the anti-solar side of the spacecraft. A two-point, on-orbit calibration accounts for the linear response of the detectors, and the smaller, nonlinear response of some IR detectors is based on pre-launch characterization (Minnett and Smith, 2014), or by periodic "warm-up - cool-down" on-orbit temperature cycling of the internal black-body (Xiong et al., 2012; Minnett and Smith, 2014).

Infrared detectors insert noise into their measurements, and the lower the temperature of the detector, the lower the noise level. Therefore, IR radiometers require cooled detectors, typically operating from 53 K (− 220 °C) to 183 K (− 90 °C) to reduce the NEΔT to < 0.1 K (Xiong et al., 2012; Minnett and Smith, 2014).

Here we provide an overview of satellite instruments that have brought us to our current capabilities to measure SST from space. The list cannot be exhaustive, but we include those sensors that have resulted in major advances, or have introduced significant technological developments to the field. Included are relevant dates and instrument characteristics, including surface spatial resolution. The references included for each sensor provide the interested reader with guidance to more detailed descriptions. For further details on past, current and planned satellites and instruments, the reader is referred to the World Meteorological Organization (WMO) Observing Systems Capability Analysis and Review (OSCAR) Tool (https://www.wmo-sat.info/oscar/).

Where possible, we include assessments of accuracy to illustrate improvements resulting from instrumental and algorithmic developments. These estimates are specific to the retrieval algorithms as well as to the instrument calibration and performance, and also to the methods used in the assessments, including environmental variability consequent on different spatial and temporal sampling of the satellite SST fields and the reference measurements.

5.1. Infrared instruments in low earth orbit

The initial motivation for flying earth-viewing IR imaging radiometers on satellites was to provide pictures of clouds to assist weather forecasters. During the sunlit part of each orbit, detectors in the visible part of the electromagnetic spectrum provided the required information, but at night IR radiometers were needed. Even though the sensitivities of the early IR detectors were poor compared to those in modern instruments, they were sufficient to reveal patterns in the cloud free parts of the images that were correctly interpreted as being indicative of spatial variability in the SST.

The spatial resolution at the sea surface of IR imaging radiometers is generally given at the subsatellite point, but because of beam spreading caused by longer path lengths the pixel size grows for measurements taken away from nadir and because of the curvature of the earth's surface the increase in size is not symmetric with growth in the across-track (scan) direction becoming greater than in the along-track direction (Fig. 7).

5.1.1. Early radiometers

Starting in 1964, only seven years after the launch of the first artificial satellite, Sputnik, NASA began to launch research and development satellites called Nimbus. The Nimbus satellites were sun-synchronous and stabilized so that instruments on board could be directed to the Earth throughout the orbits. The instruments were mostly prototypes, but once demonstrated to be successful successive versions were flown, often with incremental improvements.

Included in the instrument suite of Nimbus-1 was the High Resolution Infrared Radiometer (HRIR) which had a single IR channel, responsive to the 3.4–4.2 μm wavelength range, and having a spatial resolution of 8.6 km at the sub-satellite point with a swath extending from horizon to horizon. Because of solar contamination, these data were restricted to use only at night. The clear-sky parts of the images were used to describe variations in SST (Allison and Kennedy, 1967). The Nimbus-1 mission lasted only about one month, but Nimbus-2, launched in May 1966, functioned for about six months. The data were transmitted in analogue form and were generally displayed as photo-facsimiles in gray tones, or printed by a line-printer and contoured by hand. These were interpreted in terms of a relative SST, and sharp gradients were identified as boundaries between currents or delineating fronts and used to describe their responses to changes in atmospheric forcing, such as winds in the Arabian Sea (LaViolette and Chabot, 1968) and Persian Gulf (Szekielda et al., 1972), or boundary currents and coastal upwelling (Warnecke et al., 1971). A third HRIR, which included a visible channel, was on Nimbus-3 launched in 1969.

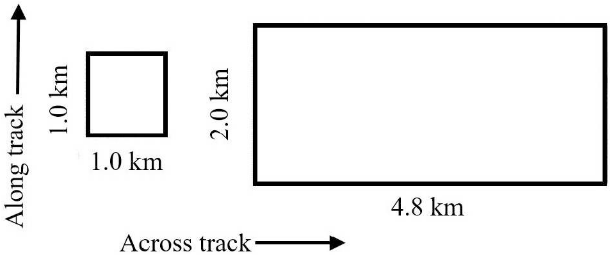

Fig. 7. A schematic of a MODIS 1 km pixel growth from nadir to the edge of swath. The total swath width is 2330 km and comprises 1354 pixels. At the swath edges, the satellite zenith angle is ~65°.

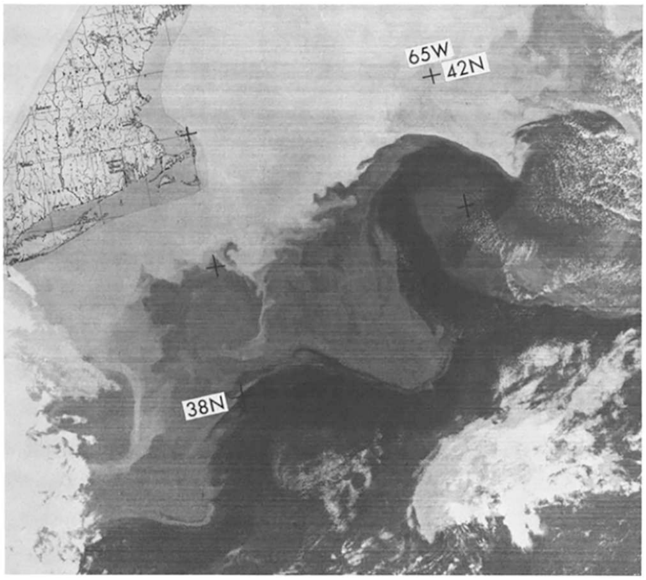

Fig. 8. VHRR IR image 4531 from NOAA 4 was obtained on November 12, 1975. The Gulf Stream north of Cape Hatteras and south of Cape Cod appears as the warmest (darkest) water. The large amplitude meanders as well as two warm core eddies are evident south of Cape Cod and Long Island (Legeckis, 1978).

A two channel radiometer, the Scanning Radiometer (SR) developed from the HRIR but with an IR channel in the 10.5–12.5 μm atmospheric window, first flew on the NOAA TIROS-M (Television Infrared Observation Satellite-M) launched in January 1970 into a sun-synchronous orbit at an altitude of 1470 km. The spatial resolution was 3.6 km at the subsatellite point. The longer IR wavelength is essentially unaffected by scattered and reflected solar radiation, so the SR IR channels were also used during the day. TIROS-M was followed by five operational satellites, NOAA-1 to -5 launched from December 1970 to July 1976, each carrying an SR.

A further development of the SR, the Very High Resolution Radiometer (VHRR) flew on NOAA-2, launched in October 1972, having channels very similar to the SR but with a spatial resolution at the subsatellite point of 0.9 km and a much reduced NEΔT of ~0.5 K the VHRR permitted greatly improved depiction of the SST in cloud-free areas. On-board data recording also allowed data to be retained out of sight of ground stations and then subsequently transmitted to a receiving station as they come into range. These technological improvements supported many investigations into ocean thermal fronts and associated features (Legeckis, 1978, and references therein).

Fig. 8 shows the thermal structure of the Gulf Stream off Cape Cod, USA, taken from the HRIR on NOAA-4 in November 1975 (Legeckis, 1978). The complexity of the fronts associated with the Gulf Stream is apparent, and explains the fact that ship-based surveys of the area defied simple interpretation (Fuglister, 1955), simply as a consequence of inadequate sampling of mesoscale current structure, and satellite imagery resolved which of multiple possible interpretations of ship-based measurements was correct.

5.1.2. The Advanced Very High Resolution Radiometer (AVHRR)

The satellite instrument that has contributed the longest to the study of SST is the AVHRR that first flew on TIROS-N launched in late 1978 (Cracknell, 1997). AVHRRs have flown on successive satellites from NOAA-6 to NOAA-19. AVHRRs are on satellites in near-polar, sun-synchronous orbits with an orbital period of about 100 min. There have been two NOAA AVHRRs operational at any given time, with at-launch local equator-crossing times of about 2.30 a.m. and p.m. and about

7.30 a.m. and p.m. The overpass times drift with the time on orbit (e.g. Fig. 1 of Bhatt et al., 2016). EUMETSAT, the European Organisation for the Exploitation of Meteorological Satellites, also flies AVHRRs on its three Metop satellites (Klaes et al., 2007) with a maintained descending equator crossing time at 9:30 a.m.

The AVHRRs on TIROS-N and NOAA-6 had only four channels and had limited capability for the derivation of SST because they lacked the "split-window" channels, numbered 4 and 5 (λ = 10.8 and 12.0 μm) which were on subsequent five-channel AVHRRs starting with NOAA-7, launched in June 1981. As with earlier IR imaging radiometers (Barton, 1985), SST retrieval from the AVHRRs without multiple IR bands was accomplished using a simple linear relationship to the measured BT, but the variability of the marine atmosphere introduced much scatter into this relationship. It was recognized early that a promising way forward was to make simultaneous measurements in two IR channels in which the atmospheric transmission was different (Anding and Kauth, 1970; McMillin, 1975; McMillin and Crosby, 1984; McMillin and Crosby, 1985; inter alia), leading to atmospheric correction algorithms given in Section 4.1.3. However, in very constrained conditions, a tailored single channel atmospheric correction may produce more accurate SST retrievals than a multichannel retrieval, an example being the very dry, cold Arctic atmosphere over the North Water Polynya (Vincent et al., 2008b; Vincent et al., 2008a).

The current version, AVHRR/3, has six channels: 1 and 2 at λ = ~0.65 and ~0.85 μm, measuring reflected sunlight are used to image clouds during the daytime part of each orbit. Channels 4 and 5, also on all AVHRRs, are in the atmospheric window close to the peak of the SST thermal emission and are used to derive SSTs. Channel 3 is in the mid-IR atmospheric window (λ = 3.7 μm), also measures surface emission, modified by its propagation through the atmosphere, and hence is used to derive SST, but at this wavelength there is a significant component of reflected and scattered sunlight rendering these measurements suitable for SST determination only at night. The λ = 3.7 μm channel data of the early AVHRRs had noise that introduced a "herringbone" effect in brightness temperature images at a level that made the quantitative use of the data very difficult (Dudhia, 1989; Warren, 1989), but research into reducing the excessive noise has shown success (Simpson and Yhann, 1994; Karlsson et al., 2017). The sixth channel of the AVHRR/3, first launched on NOAA-15 in May 1998, at $\lambda \sim$ 1.6 μm was designated 3a with the earlier λ = 3.7 μm channel being renamed 3b, provides superior discrimination of cloud over snow, ice and bright desert during the day. Given limited telemetry bandwidth, measurements from only one of these two channels are transmitted to ground, with 3a data being taken during the daytime part of the orbit, and 3b at night. Infrared channels of the AVHRRs are calibrated using measurements of an onboard blackbody plate, the temperature of which is monitored by five thermometers, and a measurement of space away from the sun providing a source of radiance very close to zero. The AVHRR/3s also incorporated several improvements, including better thermal stability of the blackbody used in the calibration of the IR channels (Trishchenko et al., 2002). The improved blackbody shielding reduced the temperature gradients that were found across the blackbody (Brown et al., 1985), which, since they exhibited orbital variations, were suggestive of stray light from the sun being incident on the blackbody. Although the AVHRR/3s on NOAA-15, -18 and -19 are still in operation, these satellites are not in maintained orbits so the equator crossing time drifts (see https://www.star.nesdis.noaa.gov/smcd/emb/vci/VH/vh_avhrr_ect.php) with the result that the on-board thermal environment may move out of that in which the sensors were designed to operate, with a consequent degradation in accuracy of their measurements (see https://www.star.nesdis.noaa.gov/sod/sst/3s/).

The images in each channel are constructed by scanning the AVHRR field of view across the Earth's surface by a rotating plane mirror with its surface inclined at 45° to its axis which lies in the direction of flight. The rate of rotation, 6 Hz, is such that successive scan lines are contiguous at the surface directly below the satellite. The width of the swath (~2700 km) results in overlap of the edges of successive orbits so the whole Earth is sampled without gaps each day. The spatial resolution at nadir is 1.1 km and 6.15 × 2.27 km^2 (across-track × along track) at the edge of swath.

An important and exhaustive reprocessing of the AVHRR SST data stream from the AVHRR on NOAA-7, in 1981, to the present including those on the Metop satellites, has been recently completed by Merchant et al. (2019). Their objective was to produce a consistent data set for the entire period that would be suitable for climate applications. For periods with overlap with the ATSR (Section 5.1.3) series of dual view radiometers, the infrared measurements from the most reliable channels of these were used as references to which the AVHRR data could be harmonized using radiative transfer modelling with atmospheric profiles given by the ERA-Interim data set (Dee et al., 2011). For AVHRR data prior to the first ATSR on ERS-1, in 1991, periods of overlap between successive AVHRRs on NOAA polar-orbiting satellites were used, but were thus far found insufficient to achieve adequate harmonization; additional reconciliation of the AVHRR SSTs to in situ sources was therefore applied prior to 1991. Thus, the resulting SST fields have a high degree of independence from in situ measurements, such as those from drifting buoys, from 1991 onwards. In addition to recalibrating the AVHRR data using improved understanding of the shortcomings of the AVHRR calibration procedures (Mittaz et al., 2019; Giering et al., 2019), the harmonization approach takes into account differences in the spectral response functions of each of the sensors, including those in the ATSR series, to produce empirical relationships to correct the residual errors in the individual AVHRR radiance measurements. A consistent Bayesian cloud screening algorithm has been applied to the data from all sensors (Bulgin et al., 2018). Apart from a few regions and periods, associated with episodes of sensor instability, stratospheric aerosols or desert dust, especially prior to ATSR data being available, the derived SSTs are accurate, having a median evaluated uncertainty of 0.18 K, at the pixel level. Long term stability, relative to drifting buoy measurements, is within 0.003 K yr^{-1} of zero, thus meeting the stability requirement of an SST CDR (Ohring et al., 2005).

5.1.3. The Along-Track Scanning Radiometer (ATSR) series

Instead of relying on the spectral dependence of atmospheric transmission to correct for the effects of the cloud- and aerosol-free atmosphere, measuring BTs at wavelengths in the atmospheric windows of the sea surface through two different atmospheric path lengths permits a direct measurement of the effect of the atmosphere on the top-of-atmosphere radiance. The pairs of such measurements must be made in quick succession, so that the SST and atmospheric conditions do not change in the time interval, and this is the basis of the Along-Track Scanning Radiometer (ATSR) series of IR radiometers. Following two ATSRs on ERS-1 and ERS-2, the Advanced ATSR (AATSR) was flown on Envisat (Louet and Bruzzi, 1999; Dubock et al., 2001), launched on 1 March 2002 for a decade-long mission. The AATSR had the same IR channels as the earlier ATSRs, but had additional channels in the visible part of the spectrum.

The ATSRs had IR channels in the atmospheric windows comparable to those of AVHRR. The axis of rotation of the scan mirror is inclined from the vertical by the half-angle of a cone, ~23.5°, so the swath passes through the subsatellite point sweeping out a curved path on the sea surface. Half a mirror revolution later, the field of view was about 900 km ahead of the sub-satellite track in the center of the 'forward view' (Prata et al., 1990). The field of view returns to the sub-satellite point, which has moved 1 km ahead of the starting point. Thus the pixels forming the successive swaths through the nadir point are contiguous. The nadir point overlays the center of the forward view after about 2 min. The scan geometry from the height of polar-orbiting satellites carrying the ATSRs, ~785 km, results in a swath width of ~500 km. The nadir measurement is through a single thickness of the atmosphere, and the slant path to the center of the forward view is almost double that, resulting in colder measured BTs for the same SST.

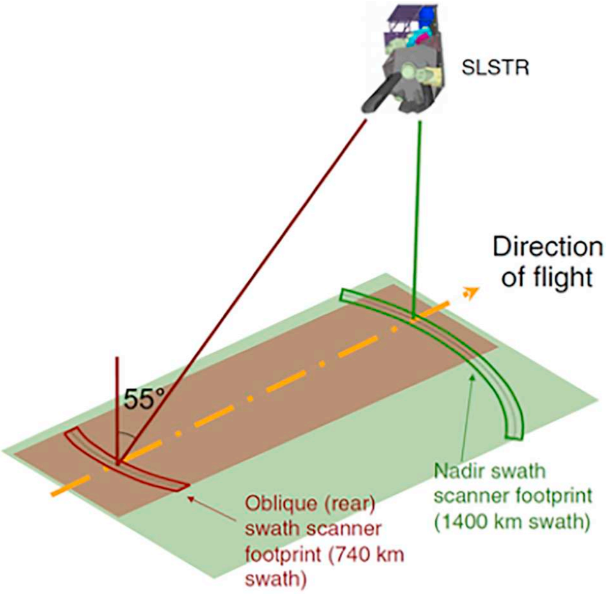

Fig. 9. Scan geometry of the SLSTR. The dual-view measurements are made by an inclined conical scan, which covers the same swath through two different atmospheric path lengths. The oblique swath is limited to 740 km by geometrical constraints. Interleaved between successive conical scans, a wider, single view swath is obtained. (Reprinted with permission from Donlon et al., 2012a).

The differences in the BTs between the forward and nadir swaths are direct measurements of the effect of the atmosphere. The atmospheric correction algorithm takes the form:

$$SST = c_o + \sum_i c_{n,i} T_{n,i} + \sum_i c_{f,i} T_{f,i} \tag{10}$$

where the subscripts n and f refer to measurements from the nadir and forward views, i indicates two or three atmospheric window channels and the set of c are coefficients (Závody et al., 1995). As with the atmospheric correction algorithm for other IR radiometers, an Optimal Estimation approach has been developed for the dual-view radiometers (Embury and Merchant, 2012; Embury et al., 2012) which has become the basis of a 20-yr time series intended to be of climate quality (Merchant et al., 2012; Berry et al., 2018).

The current generation of dual view radiometers, the Sea and Land Surface Temperature Radiometer (SLSTR; Donlon et al., 2012a; Smith et al., 2014) flying on Sentinel 3a launched on 16 February 2016 and Sentinel 3b launched on April 25, 2018, includes a quasi-linear scan through nadir to extend the spatial coverage (Fig. 9). In the extended scan, the atmospheric correction algorithm is based on a multi-channel formulation.

The coefficients of the atmospheric correction algorithms are derived by radiative transfer simulations, and have an explicit latitudinal dependence (Závody et al., 1995). Accurate calibration of the measured radiances is achieved using two onboard blackbody cavities, situated between the apertures for the nadir and oblique views being scanned during each rotation of the mirror (Prata et al., 1990). One blackbody is at the ambient temperature of the instrument, ~262.7 K, while the other is heated to ~301.6 K (Smith et al., 2012; Minnett and Smith, 2014) resulting in the measured brightness temperatures of the sea surface being straddled by the calibration temperatures.

5.1.4. *The Moderate Resolution Imaging Spectroradiometer (MODIS)*

The Moderate Resolution Imaging Spectroradiometer (MODIS) is a 36-band imaging radiometer on the NASA Earth Observing System (EOS) satellites Terra, launched in December 1999, and Aqua, launched in May 2002. Included in the innovations in the design of MODIS are (i) multiple detectors - ten - for each spectral band so that ten lines of pixels are measured simultaneously across the swath, (ii) a dual-sided scan mirror, and (iii) several advances to ensure the calibration, both radiometric and spectral, of the measurements. For calibration of the IR measurements, a grooved plate blackbody target with twelve embedded thermometers was developed, and the measurements of this along with those of cold space provided a two-point radiance calibration. The swath width of MODIS, at 2330 km, is narrower than that of AVHRR, with the result that a single day's coverage is not entire, but the gaps from one day are filled in on the next. The spatial resolution of the IR bands is 1 km at nadir. Further details of the ocean remote sensing of MODIS are given by Esaias et al. (1998). MODIS is much more complex than other radiometers used for deriving SST, but uses the same atmospheric transmission windows. The two bands in the 10–12 μm wavelength interval have bandwidths of ~0.5 μm, which are about half of those of the AVHRR and ATSR series. MODIS also has three narrow bands in the 3.7–4.1 μm window, which, although limited by solar effects during the day, produce more accurate retrievals of SST during the night. Several of the other MODIS bands contribute to improving the SSTs by better identification of residual cloud and aerosol contamination (Kilpatrick et al., 2015; Kilpatrick et al., 2019).

5.1.5. *Visible Infrared Imaging Radiometer Suite (VIIRS)*

The replacement of the AVHRRs on the NOAA polar-orbiting satellites is the Visible Infrared Imaging Radiometer Suite (VIIRS), which built on experience gained from MODIS, including sixteen detectors for each band and the grooved blackbody for calibration. The paddle-wheel scan mirror of MODIS was not used, but instead the rotating telescope fore-optics as on SeaWiFS (Sea-Viewing Wide Field-of-View Sensor) was adopted, with a "half-angle mirror" to prevent image rotation across the swath that would otherwise occur as a result of using multiple detectors. The first VIIRS was launched on the Suomi-National Polar-orbiting Partnership satellite (S-NPP) on October 28, 2011, and the second was launched on November 18, 2017, on NOAA-20. VIIRS has 22 channels in the visible and IR parts of the electromagnetic spectrum; the channels are a subset of those of MODIS. The spatial resolution at the sea-surface is 0.75 km at nadir, and VIIRS has an innovative approach of aggregating rectangular pixels, each having an aspect ratio of 3:1 in the along-track direction, to reduce the growth of pixel size across the swath away from nadir (Schueler et al., 2013; Gladkova et al., 2016). The IR bands used for SST measurements are the standard two in the λ = 10–12 μm interval, and two in the λ = 3.7–4.1 μm atmospheric transmission window for use at night. VIIRS has a higher resolution IR band, 375 m at nadir, that has a spectral response from λ = 10.6–12.4 μm, essential using the entire atmospheric transmission window. While the spectral width of this band and the absence of another high-resolution band in this window prevents the use of an atmospheric correction algorithm to produce SSTs at the high resolution, an approach has been developed applying the atmospheric correction derived using the 750 m bands. This approach permits the use of VIIRS SSTs to investigate submesoscale processes at the ocean surface (Cornillon et al., 2014). NOAA-20 is the first of four planned satellites each carrying a VIIRS, providing SSTs into the late 2030s.

5.1.6. *Second-generation Global Imager (SGLI)*

The Japanese Global Change Observation Mission (GCOM) currently comprises two satellites: GCOM-W (Water) launched in 2012 into the A-Train, a series of satellites carrying complementary instruments in the same orbit facilitating the analysis of measurements from diverse instruments (L'Ecuyer and Jiang, 2010), and GCOM-C (Climate) launched in December 2017. GCOM-C is in a sun-synchronous polar orbit with an ascending node time of 22:30. Both GCOM satellites have instruments with SST capability as GCOM-W carries the Advanced Microwave Scanning Radiometer-2 (AMSR2) described below (Section 5.5.7) and GCOM-C carries the Second-generation Global Imager (SGLI), which is an imaging radiometer in the visible and IR. SGLI comprises two sensors: the Visible and Near Infrared Radiometer (VNR)

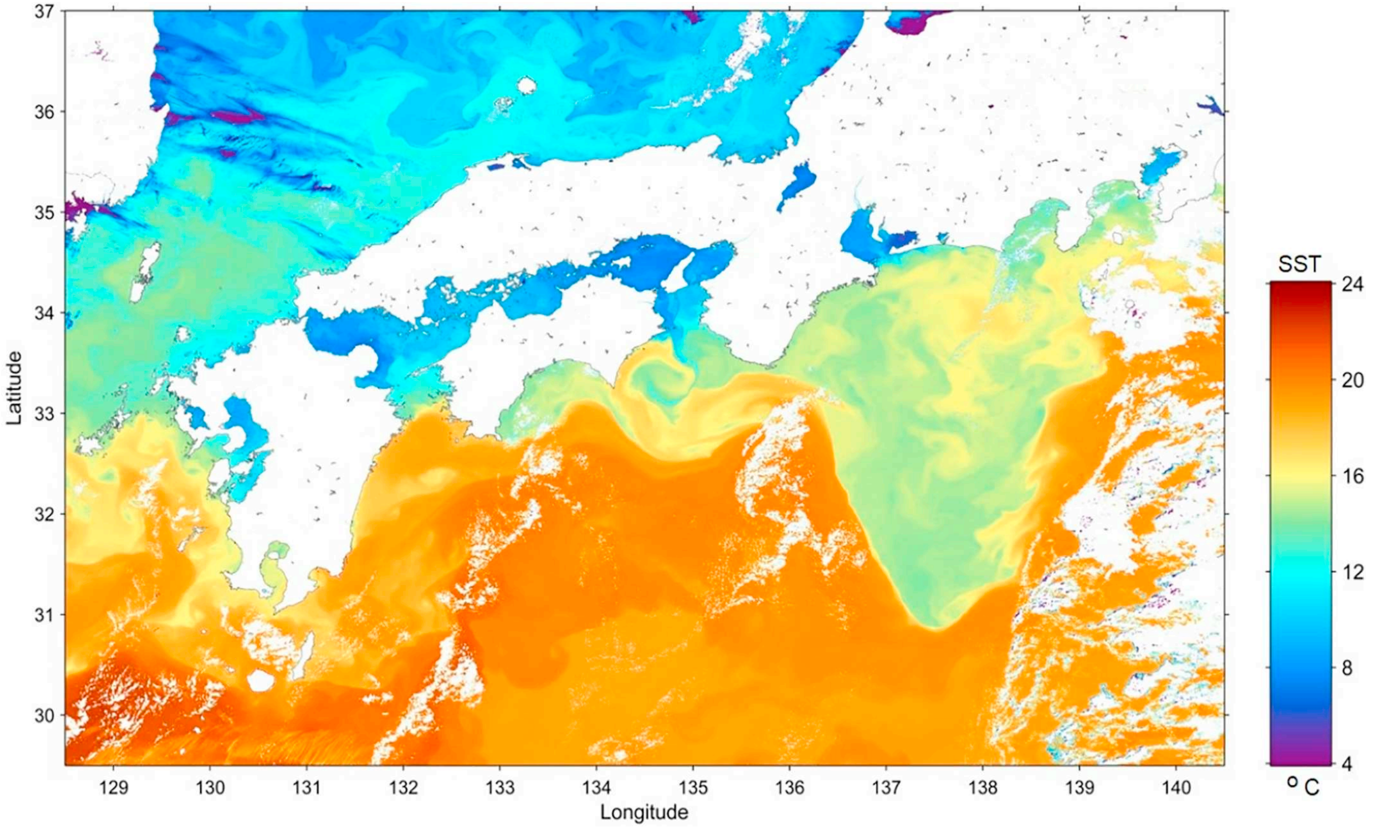

Fig. 10. SST in the vicinity of Japan derived from SGLI on 27 February 2018, showing complex structure both inshore and offshore, and the sharp temperature contrast with the waters of the Kuroshio to the south. From Tanaka et al., 2018, with permission.

and the Infrared Scanning Radiometer (IRS). The IRS includes two split-window channels at $\lambda = 10.78\,\mu m$ and $11.97\,\mu m$ with a resolution of 250 m at nadir and a swath width of 1400 km. The high resolution SSTs are expected to be of particular value in studying coastal processes. The SST fields derived from the split window bands are clean (Fig. 10) and initial comparisons with in situ temperatures from iQuam (Xu and Ignatov, 2014) during October 2018 indicate a mean difference for highest quality SGLI SSTs of −0.063 K during the day and −0.181 K during the night, with standard deviations of 0.333 K and 0.619 K and robust standard deviations of 0.284 K and 0.287 K. (Y. Kurihara, 2018, pers. comm.). The relatively high nighttime standard deviations are attributed to imperfections in the cloud screening algorithms (ibid.).

5.1.7. Multichannel Visible Infrared Scanning Radiometer (MVISR)

The Chinese Meteorological Administration (CMA) has developed a series of meteorological satellites called FengYun, meaning “wind and cloud” and commonly abbreviated to FY, that comprise both sun-synchronous polar-orbiters and geostationary satellites. FY1-A was launched in 1988 into polar orbit but was very short lived. FY-1B was launched in September 1990 and functioned for about one year, followed by FY1-C in 1999 which completed a five-year mission, with overlap with FY1-D, launched in 2002, that functioned for nearly a decade. The FY1-C and -D series carried the Multichannel Visible Infrared Scanning Radiometer (MVISR), which had 10 channels, most of which were in the visible and near-IR but included three in IR atmospheric windows: $\lambda = 3.75\,\mu m$, $10.8\,\mu m$ and $12.0\,\mu m$. These had the potential to be used in SST retrievals, but the relatively high NEΔTs (0.4 K at 300 K at $\lambda = 3.75\,\mu m$; 0.22 K at 300 K at $\lambda = 10.8$ and $12.0\,\mu m$), as well as the difficulty of accessing the data by non-Chinese researchers limited the MVISR applications. The spatial resolution was 1.1 km at the subsatellite point.

5.1.8. FY-3 Visible and Infra-Red Radiometer (VIRR)

The current series of FY polar-orbiters, FY-3, carry the Visible and Infra-Red Radiometer (VIRR) with IR bands similar to those of the MVISR. FY-3A was launched in 2008 and functioned until 2015; FY-3B, -3C and -3D are operating at the time of writing. Comparisons with the global iQuam buoy temperatures from May to July 2014, yielded mean differences of −0.26 K during the day and 0.06 K at night, with standard deviations of 0.54 K and 0.56 K (Wang et al., 2014). The VIRR was replaced on FY-3D by a much more capable instrument, the Medium Resolution Spectral Imager-2 (MERSI-2) with 25 channels, including one at $\lambda = 3.80\,\mu m$ with surface resolution of 1 km at nadir, and two at $\lambda = 10.8\,\mu m$ and $\lambda = 12.0\,\mu m$ with spatial resolution of 250 m at the subsatellite point. A further four FY-3 satellites are planned to extend the series beyond 2027.

5.1.9. HY-1 China Ocean Colour & Temperature Scanner (COCTS)

The Chinese State Ocean Administration has sponsored the development of the polar-orbiting ocean satellites called Hai Yang, meaning “Ocean” and referred to as the HY series. HY-1A and -1B were small satellites, launched in 2002 and 2007, and carried two imagers: the Coastal Zone Imager with four visible channels and the China Ocean Colour & Temperature Scanner (COCTS), a ten-channel imager with eight in the visible and near IR, and two in the thermal IR, $\lambda = 10.85\,\mu m$ and $11.95\,\mu m$, with a spatial resolution at nadir of 1.1 km. Comparisons with temperatures measured by buoys in the North-East Asian Regional Global Ocean Observing System revealed mean differences of 1.22 K and a standard deviation of 1.78 K with the HY-1B COCTS SST retrievals using a standard NLSST algorithm (Lei and Cong, 2013). When new coefficients for the NLSST were calculated using the matchups between COCTS BTs, and buoy data, the mean difference was removed and the standard deviation reduced to 1.35 K. The HY-1C was launched in September 2018, and a further three satellites are planned to provide data beyond 2029.

5.2. Hyperspectral IR imagers

For most of the period of satellite retrievals of SST, IR radiometers have provided measurements in discrete spectral bands defined by filters. For SST determination, the channels were selected in spectral intervals where the atmosphere is relatively transparent. But, hyperspectral IR radiometers that measure the full or significant parts of the spectrum of IR emission at orbital height have also been flown. In spectral regions where the atmospheric transmission is low, the measurements are primarily of atmospheric emission, and can be used to derive atmospheric soundings, cloud properties, and trace gas concentrations. In the high-transmission atmospheric window spectral regions, surface temperatures can be derived. There are two types of imaging hyperspectral IR radiometers: those using diffraction gratings, and those based on Fourier-Transform interferometry. Both split the incoming spectrum of IR radiation into numerous spectral intervals, each very much narrower than those derived by filters in more conventional multispectral radiometers, so to retain a usable signal-to-noise ratio the field-of-view of the radiometer is increased to typically ~12 km, with an increase in the signal integration time. The decrease in the spatial resolution is a hindrance to deriving accurate SSTs given the need to identify confidently clear sky pixels.

5.2.1. Atmospheric Infrared Sounder (AIRS)

The Atmospheric Infrared Sounder (AIRS; Aumann et al., 2003) on the NASA satellite Aqua, launched in May 2002, is a grating spectrometer that samples three intervals of the IR spectrum: $\lambda = 3.75$ to $4.59\,\mu m$, $\lambda = 6.20$ to $8.22\,\mu m$, and $\lambda = 8.80$ to $15.37\,\mu m$, with a total of 2378 channels. The width of the AIRS scan is 1650 km. In principle, the high spectral resolution of AIRS should make it a good sensor for SST_{skin} derivation as some of the spectral regions with the highest atmospheric transmission are included in the measurements, such as wavenumber $2616\,cm^{-1}$ ($\lambda = 3.823\,\mu m$), but this does not seem to have been exploited by the community. One reason might be the relatively poor spatial resolution ($13 \times 13\,km^2$ at nadir) which limits the opportunities to finding clear-sky pixels.

5.2.2. Infrared Atmospheric Sounding Interferometer (IASI)

An important instrument on the three Metop polar-orbiting satellites of EUMETSAT (Klaes and Holmlund, 2014) is the Infrared Atmospheric Sounding Interferometer (IASI). Metop-A was launched in 2006, -B in 2012 and -C in 2018. The IASI (Blumstein et al., 2004; Simeoni et al., 2004) is a Fourier-Transform IR Interferometer (Michelson and Morely, 1887; Griffiths and de Haseth, 1986) having a spectral range of $\lambda = 3.62$ to $15.5\,\mu m$ with 8461 spectral samples. The IASI calibration, which uses an internal blackbody target and a measurement of cold space, has been determined to be well-specified (Hewison and König, 2008) and stable (Aumann and Pagano, 2008), and consequently the IASIs have been selected as reference instruments by the Global Space-Based Inter-Calibration System (GSICS; Hewison et al., 2013). A comparison of best quality Metop-A IASI SST_{skin} retrievals with subsurface temperatures from drifting buoys resulted in a mean difference of $-0.16\,K$ with a standard deviation of 0.33 K (O'Carroll et al., 2012), and a three-way analysis of IASI and AVHRR (also on Metop-A) and drifters resulted in a standard deviation attributable to IASI of 0.28 K (ibid).

5.3. High resolution imagers

The majority of IR imaging radiometers on polar orbiting satellites have surface resolution of typically $1\,km^2$ and broad swaths that provide global, or near global, coverage in a day. For some purposes, usually associated with land surface applications, a much higher spatial resolution is required, and radiometers developed for these applications may also be used to derive SST provided there is a mechanism to correct for atmospheric effects and the IR measurements are well calibrated. To achieve high spatial resolution, coverage is sacrificed resulting in a much reduced swath width.

5.3.1. Landsat

The Landsat series of satellites have been in operation since 1972 carrying instruments designed to support monitoring and studying land surfaces. As such, these instruments have high spatial resolution. The imagers in the first satellites were limited to measurements in the visible, but with the Thematic Mapper (TM) on Landsat-4 and -5, launched in 1982 and 1984, a thermal IR channel ($\lambda = 10.4$–$12.5\,\mu m$) was added. Landsat-6 had a launch failure. This IR channel is also included in the Enhanced TM+ (ETM+) on Landsat-7, launched in 1999, with a surface resolution of 60 m at nadir in the IR and a swath 183 km wide. The ETM+ is still in operation. Landsat-8 (formerly called the Landsat Data Continuity Mission, LDCM), was launched on 11 February 2013, with two instruments: the Operational Land Imager (OLI) that operates in the visible through the short-wave IR; and the Thermal Infrared Sensor (TIRS), a two-channel radiometer ($\lambda = 10.3$–$11.3\,\mu m$ and $\lambda = 11.5$–$12.5\,\mu m$) with a spatial resolution of 100 m at nadir and an 185 km swath.

The TM and ETM+ IR measurements are calibrated on orbit by scanning a calibration wand in the field of view that serves as a warm blackbody at a controlled temperature and a cold shutter (Markham et al., 1997; Barsi et al., 2016). The TIRS on-orbit calibration uses measurements of cold space and of a blackbody at a known temperature with a correction for the non-linearity of the detector responses based on pre-launch calibration (Montanaro et al., 2014). However, evidence of stray light contamination was found that required a further correction (Wang et al., 2017). The large aperture of the TIRS renders accurate calibration very challenging, and it was recognized that comparisons with measurements of other spacecraft sensors, such as MODIS (Section 5.1.4) and GOES Imager (Section 5.4.3) would be a valuable approach (Wang et al., 2017; Wang and Ientilucci, 2018).

The high resolution of the TIRS measurements has been exploited in coastal waters, for example, to study inshore water quality (Trinh et al., 2017) and thermal discharge of cooling water from nuclear power stations (Wang et al., 2016).

5.3.2. ASTER

The Advanced Spaceborne Thermal Emission and Reflection Radiometer (ASTER) is a Japanese imaging radiometer on the Terra satellite. ASTER has 14 spectral channels spanning the visible to the thermal IR, including two split-window channels centered at $\lambda = 10.65$ and $11.30\,\mu m$ with bandwidths of 0.667 and $0.593\,\mu m$ (Yamaguchi et al., 1998). The ASTER optical system for the IR channels is a whisk broom scanner, with the visible and short-wave IR channels being push broom imagers. The IR channels have a spatial resolution of 90 m at nadir (Yamaguchi et al., 1999). ASTER does not operate continuously, but "scenes" are gathered with dimensions about $60 \times 60\,km^2$ according to a pre-programmed scheme; about 600 scenes can be gathered on one day (ibid). Unlike the IR measurements from most other imaging radiometers that are calibrated using two internal blackbody targets at different temperatures, or one blackbody target and a view of cold space (Minnett and Smith, 2014), the geometry of the ASTER optics prevents such an approach and instead the IR measurements are calibrated with a full-aperture blackbody that can be held at constant temperatures from 270 to 340 K. The blackbody is viewed before and after each scene (Tonooka et al., 2005; Hook et al., 2007). Although ASTER was designed for land surface and cloud measurements, its high spatial resolution and calibrated IR channels allows it to provide useful SST retrievals, especially in coastal areas (e.g. Matsuoka et al., 2011).

5.3.3. ECOSTRESS

Developed for land surface applications, the ECOsystem Spaceborne

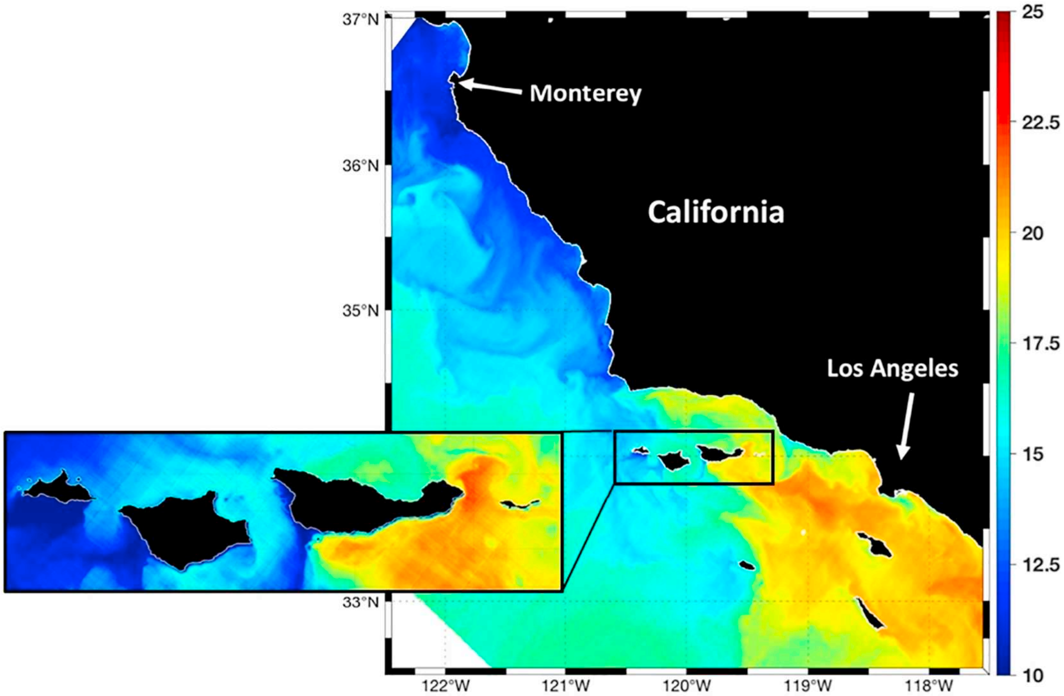

Fig. 11. ECOSTRESS composite of two Level-2 images of SST derived with the Land Surface Temperature (LST) retrieval algorithm, acquired on September 16, 2018 at 13:04 and 13:05 UTC. Colder SSTs are associated with upwelling north of Santa Barbara. The enlargement shows fine-scale SST gradients around the Channel Islands National Marine Sanctuary – note the color scale has been stretched to cover 14 °C to 22 °C to show the fine-scale detail. The western islands (San Miguel, Santa Rosa) experience much cooler ocean temperatures than the eastern islands due to differences in upwelling, winds and currents. Image credit: Daniel Otis, Institute for Marine Remote Sensing (IMaRS), College of Marine Science, University of South Florida. Reproduced from https://ecostress.jpl.nasa.gov/gallery/viewgalleryimage with permission. (For interpretation of the references to color in this figure legend, the reader is referred to the web version of this article.)

Thermal Radiometer Experiment on Space Station (ECOSTRESS) also has a capability to derive SSTs. ECOSTRESS was launched to the International Space Station (ISS) on 29 June 2018 and installed on there on July 2. Following the commissioning phase, ECOSTRESS became operational on August 20, 2018. The ISS orbit has an inclination of 51.64° and thus high latitudes are not accessible to ECOSTRESS. The orbit is not sun-synchronous and successive arcs of the orbit drift west (at the Equator) by about 22.9° of longitude, meaning that over about two months a full diurnal cycle is sampled. ECOSTRESS is an infrared imaging radiometer with five spectral bands in atmospheric transmission windows ($\lambda = 8.29, 8.78, 9.20, 10.49, 12.09\,\mu m$) each having a spatial resolution at nadir of $38\,m \times 68\,m$. From the altitude of ~400 km of the ISS the swath is 402 km wide (Hulley and Hook, 2018). Each infrared band has 256 detectors that sweep out lines of pixels in a whisk broom fashion, similar to MODIS (Section 5.1.4). Calibration is accomplished with two on-board blackbody targets at 300 K and 340 K that are scanned each mirror rotation (ibid).

Fig. 11 shows an example of coastal SST from ECOSTRESS derived using a land surface temperature retrieval algorithm, revealing high-resolution variability indicating the potential of ECOSTRESS to make contributions to coastal research.

As yet there has been no concerted effort to determine the accuracy of the ECOSTRESS SST_{skin} retrievals, but work is underway (Hulley et al., 2019), including using the facilities at Lake Tahoe and the Salton Sea as has been done for ASTER and MODIS (Hook et al., 2007; Tonooka et al., 2005). Preliminary analysis of four months of comparisons indicate that the RMSE is < 1 K (G. C. Hulley et al., 2019, pers. comm.).

5.4. Geostationary satellite instruments

The early geostationary earth observation satellites were "spin-stabilized" meaning they spin about an axis parallel to that of the rotation of the earth. Thus an image of the earth's disk, as visible from geostationary orbit, is built as the sensor scans the earth's disk longitudinally, with latitudinal sampling being achieved through a stepped motion of the sensor's scan mirror. There are several advantages to spin-stabilization, but a major disadvantage is the small part of each revolution when the earth is in view. Three-axis stabilized spacecraft, as used for GOES-8 in 1994 and subsequent satellites in the GOES series, rotates on its axis parallel to the earth's axis at the same rate as the earth. Thus, a single side of the satellite remains facing the earth, and instruments mounted on this face of the satellite view the earth all the time. The current Meteosat series, the European geostationary satellites, are spin-stabilized but the third generation will be 3-axis stabilized with the first planned for launch in 2021 and the series expected to reach into the late 2030s.

The potential contributions of imagery from geostationary orbit to improve weather nowcasting and forecasting were recognized early in the satellite era, and the first imagers on geostationary earth observation satellites were sensitive to radiation in the visible part of the spectrum. The first was the spin-scan cloud camera (SSCC) on the Applications Technology Satellite-l (ATS-l) launched in 1966 and which functioned for seven years. In 1974, the three-axis stabilized satellite ATS-6 was launched carrying the Geosynchronous Very High Resolution Radiometer (GVHRR) that included the first IR channel that permitted cloud imaging at night and estimation of cloud-top temperature, and thereby cloud-top height. The spectral width of the IR channel was 10.5–12.5 μm. The ATS-6 mission ended in 1979, ending the deployment of the last 3-axis stabilized geosynchronous satellites until 1994.

Some details of currently operational geostationary satellites are summarized in Table 1.

5.4.1. VISSR and VAS

In 1974, the first model of the Visible Infrared Spin-Scan

Table 1
Positions of geostationary satellites with an SST retrieval capability.

Name	Date launched	Longitude	Notes
GOES-16	19 November 2016	75.2°W	GOES-E. Operational on 18 December 2017.
GOES-17	1 March 2018	137.2°W	GOES-W. Operational on 12 February 2019.
Meteosat-8	28 August 2002	41.5°E	Moved on 4 July 2016 for Indian Ocean coverage.
Meteosat-9	21 December 2005	3.5°E	As backup for Meteosat-10 or Meteosat-11.
Meteosat-10	15 July 2012	9.5°E	Moved on 21 January 2013 for rapid scans over Europe.
Meteosat-11	15 July 2015	0°	Operational on 20 February 2018.
Himawari-8	7 October 2014	140.7°E	Operational on 7 July 2015.
Himawari-9	2 November 2016	140.7°E	On standby as operational replacement for Himawari-8.
FengYun-2E	23 December 2008	86.5°E	Operational on 1 July 2015
FengYun-2F	13 January 2012	112.0°E	On standby as operational replacement; used now for regional scanning
FengYun-2G	31 December 2014	99.5°E	Relocated from 105°E on 16 April 2018.
FengYun-2H	5 June 2018	79.0°E	Operational on 1 January 2019.
FengYun-4A	10 Dec 2016	105.0°E	Operational on 1 May 2018.
INSAT-3D	25 July 2013	82.0 E	Operational on 15 January 2014.
INSAT-3DR	8 September 2016	74.0 E	Operational on 11 October 2016.
GEO-KOMPSAT-1	27 June 2010	128.25°E	Also referred to as Cheollian-1 and COMS-1. Operational on April 1, 2011.
GEO-KOMPSAT-2A	4 December 2018	128.2°E	In commissioning. Expected to become operational in July 2019.

The longitude of each satellite may vary throughout its lifetime, being moved according to operational requirements. The information shown here is taken from the WMO OSCAR tool (https://www.wmo-sat.info/oscar/) or the web-pages of the satellite operators.
The satellites shown are those in operation at the time of writing. For past and planned satellites, please see the text.

Radiometer (VISSR) was launched on the spin-stabilized Synchronous Meteorological Satellite-1 (SMS-1; McClain, 1980). VISSR had one IR channel occupying the 10.5–12.6 μm wavelength interval and was the first to have on-board IR calibration (Hursen and Ross, 1996). The spatial resolution of the IR channel at the subsatellite point was 7 km and produced a full-disk image of the Earth each 30 min. Having just a single IR channel prevented a split-window type atmospheric correction algorithm to derive SST, but nevertheless, the VISSR brightness temperature images elucidated many upper ocean processes, including westward propagating tropical instability waves (Legeckis, 1977). The VISSR was the principal instrument on five US satellites: SMS-1 and -2, GOES-1, -2 and -3, four Japanese satellites: Himawari-1 to -4 (also known as Geostationary Meteorological Satellite, GMS-1 to -4).

An important development of the VISSR was the VISSR Atmospheric Sounder (VAS) that first flew on GOES-4, launched in 1980. VAS included a filter wheel in front of the detectors that resulted in there being 12 channels in the IR that were selected at wavelengths to permit sounding of the atmospheric temperature and humidity (Menzel et al., 1981). In addition to the 10.5–12.6 μm wavelength band inherited from VISSR, VAS had two additional channels, one in the 3.9 μm window and the other at 12.6 μm where the atmosphere is relatively transparent but has a marked sensitivity to water vapor variations (Section 4.1.1). Measurements in these three channels permitted a multi-channel atmospheric correction to estimate SST (Bates and Smith, 1985).

5.4.2. SEVIRI

The main payload of the current European Meteosats is the Spinning Enhanced Visible and Infrared Imager (SEVIRI), having 12 spectral channels of which 8 are in the IR having an instantaneous field of view (IFOV) of 4.8 km at the surface at nadir, over-sampled to give a pixel resolution of 3 km at the subsatellite point (European Space Agency, 1999; Aminou, 2002; Schmid, 2012). With a rotation rate of 100 rpm, the SEVIRI provides full disk images every 15 min. The primary location of Meteosat is at 0°E above the Equator, which is now occupied by Meteosat-11. Meteosat-10 is currently at 9.5°E producing rapid scans of a section of the earth's disk of limited latitudinal range primarily covering Europe every 5 min. Meteosat-9 is now at 3.5°E as a backup for −10 and −11, and Meteosat-8 is at 41.5°E to provide coverage over the Indian Ocean. Some of the IR channels of SEVIRI, those at $\lambda = 3.92$ μm, 10.8 μm and 12.0 μm, are suitable for accurate SST retrievals.

5.4.3. The GOES imager

The GOES Imager (Hursen and Ross, 1996) has flown on the GOES 8–15 satellites (Menzel and Purdom, 1994) from 1994 to the present; GOES-15 is still operating, but is scheduled to be decommissioned in July 2019. There are two GOES operational spacecraft - one at nominally 75°W, called GOES-East, and the other at 135°W, GOES-West. The image of the Earth's disk is constructed by scanning the field of view of the radiometer along horizontal lines by an oscillating mirror, with latitudinal increments of the scan line resulting from tilting the axis of the scan mirror between longitudinal scans. The spatial resolution of the IR channels is 4 km at the subsatellite point (Maturi et al., 2008). A full-disk image is produced every 30 min, and limited areas where rapidly evolving meteorological features are occurring, can be imaged in correspondingly shorter time intervals. The GOES Imager is a five-channel instrument, of which three on earlier satellites (GOES-8 to GOES-11) were suitable for SST retrieval: $\lambda = 3.9$ μm, 10.7 μm and 11.95 μm. On GOES-12, which became operational in 2003, and subsequent satellites, the channel at $\lambda = 11.95$ μm was moved to 13.35 μm, thereby compromising the feasibility of using split-window atmospheric corrections to derive SSTs, although an algorithm using the $\lambda = 3.9$ μm after a correction for solar contamination was developed (Merchant et al., 2009a).

5.4.4. Advanced Himawari Imager (AHI) and the Advanced Baseline Imager (ABI)

The first of a new generation of geostationary meteorology satellites of the JMA, Himawari-8 (Bessho et al., 2016), began operation on July 7th 2015; it is located at 140.7°E above the equator and replaced the earlier MTSAT-2 (also known as Himawari-7). MTSAT-2 carried a five-channel imager with IR channels for SST at $\lambda = 3.75$ μm, 10.8 μm and 12.0 μm, with a 4 km spatial resolution at nadir. Himawari-8 carries the first of a new type of visible and IR imager for geostationary satellites, the Advanced Himawari Imager (AHI). The AHI has 16 spectral channels of which five are in the IR and can be used for SST retrievals: $\lambda = 8.60$ μm, 10.45 μm, 11.20 μm, and 12.35 μm, with one at $\lambda = 3.85$ μm available for use at night. The IR bands have a spatial resolution of 2 km at nadir. The AHI provides full disk images of most of the Pacific Ocean and eastern Indian Ocean as rapidly as every 10 min, with smaller areas being sampled more frequently as required.

The first of a new series of NOAA geostationary satellites, called GOES-R while in development and renamed GOES-16 once declared operational on December 16th 2017, is located above 75.2°W. GOES-17, operational since February 12th 2019, is located above 137.2°W. This series of geostationary satellites, each with a planned lifetime of 10 years, is expected to operate into the mid-2030s, carries the

Advanced Baseline Imager (ABI), which has very similar capabilities to those of the AHI, including IR bands suitable for the derivation of SST, at $\lambda = 3.90\,\mu m$, 8.50 μm, 10.3 μm, 11.2 μm, ad 12.3 μm.

The AHI and ABI represent a significant development in the derivation of SST from geostationary orbit.

5.4.5. FengYun-2 Stretched Visible Infrared Spin Scan Radiometer

The Chinese, spin-stabilized geostationary satellites are the FengYun-2 (FY-2) series, with FY-2A having been launched in 1997 to a position above 105°E, where it operated for a little less than one year. It was succeeded by FY-2B in 2000 which functioned until 2004. These two satellites carried the S-VISSR (Stretched-VISSR) with a single IR channel at $\lambda = 10.5$–12.5 μm. The FY-2C, launched in 2004 to a position at 123°E, and subsequent satellites of this series carried an enhanced S-VISSR with a channel at $\lambda = 3.75\,\mu m$ and split-window channels at $\lambda = 10.8\,\mu m$ and 12.0 μm, permitting multi-channel atmospheric corrections to derive SST. The on-board calibration of the FY-2C S-VISSR IR bands was checked by comparing their BTs with those of MODIS on Terra and AIRS by Jiang et al. (2009) who reported that while the S-VISSR calibration was stable, there were significant temperature dependent offsets between the IR channels of the three instruments, which are largely consistent between S-VISSR and the two reference radiometers. Currently there are four FY-2s in operation: FY-2E at 86.5°E, FY-2F at 112°E, FY-2G at 105°E, and FY-2H launched in June 2018, at 79°E.

5.4.6. FengYun-4 Advanced Geostationary Radiation Imager

The first of the next-generation Chinese geostationary satellites, the FY-4 series (Yang et al., 2017) was launched in December 2017 into a position at 105°E. The FY-4s are three-axis stabilized satellites and one of the six instruments making up their payload is the Advanced Geostationary Radiation Imager (AGRI) with 14 channels, including two at $\lambda = 3.75\,\mu m$ – one with spatial resolution of 4 km and an NEΔT of 0.2 K at 300 K, and the other with a surface resolution of 2 km with an NEΔT of 0.7 K at 300 K – and two split window channels at $\lambda = 10.7\,\mu m$ and 12.0 μm with 4 km spatial resolution and NEΔTs of 0.2 K at 300 K. A full disk scan can be made by AGRI every 5 min. Seven FY-4 satellites are planned which will extend beyond 2040.

5.4.7. Communication Ocean Meteorological Satellite (COMS) meteorological imager

To provide ocean and meteorological measurements in the vicinity of the Korean Peninsula, a geostationary satellite was launched in June 2010 to 128.25°E. Called the Communication Ocean Meteorological Satellite (COMS), it has subsequently been renamed GEO-KOMPSAT 1 (Geostationary Korea Multi-Purpose Satellite) and is also referred to as Cheollian-1, it is three-axis stabilized and serves three objectives: monitoring ocean color, providing meteorological imagery, including IR bands that can be used for SST derivation, and for communications. The Meteorological Imager (MI) is a development of the imager flown on MTSAT-2 with five bands including at $\lambda = 3.75\,\mu m$, 10.8 μm and 12.0 μm (Cho and Youn, 2006). Following adjustment of the calibration of the MI IR channels after comparison with IASI measurements in the framework of the Global Space-based Inter-Calibration System (GSICS; Section 11), the SSTs derived using an NLSST atmospheric correction algorithm compared much better with in situ measurements from drifters in the western Pacific Ocean and eastern Indian Ocean with daytime differences of −0.062 K in the mean and root-mean-square error of 0.666 K, and night-time values of −0.020 K and 0.809 K (Park et al., 2015).

The next-generation satellites comprise of two satellites operating together; GEO-KOMPSAT-2A was launched on December 4th 2018, and -2B is scheduled for launch in October 2019. GEO-KOMPSAT-2A carries an Advanced Meteorological Imager (AMI), which is very similar to the AHI and ABI. GEO-KOMPSAT-2B will be for monitoring ocean color, atmospheric ozone and other trace gases.

5.4.8. INSAT-3 imager

The Indian Space Research Organisation (ISRO) has been launching satellites into geostationary orbit since 1982. These Indian National Satellites (INSATs) include telecommunication satellites as well as those for earth observation. The early series of satellites carried the Very High Resolution Radiometer (VHRR), with a single IR channel at $\lambda = 11.6\,\mu m$ thus not permitting correction for the atmosphere to derive SSTs. INSAT-3D, launched in 2013 above 82°E, included an Imager with IR channels at $\lambda = 3.82\,\mu m$, 10.8 μm, 12.0 μm, with a 4 km resolution at the subsatellite point. INSAT-3DR (Repeat) with the same payload was launched to 74°E in 2016, with INSAT-3DS (Second Repeat) scheduled for launch in 2022. Comparisons with the iQuam drifter data in the seas around India, revealed mean differences ranging from −0.16 K to −0.20 K, being worse in the Arabian Sea at −0.27 K with greater values during the monsoon season (Tyagi et al., 2018).

5.5. Microwave instruments

Imaging microwave radiometers are confined to satellites with orbital altitudes typical of those in polar orbits, or at lower altitudes, as the spatial resolution is limited by the size of an antenna that can be deployed on a spacecraft, typically 2 m or less in diameter. Since the sensitivity of the emitted radiation from the sea surface in microwave frequencies to SST variations is at 6 to 10 GHz, $\lambda = 5$ cm to 3 cm, (Fig. 6; Wilheit, 1979) and so the diffraction-limited surface resolution is tens of km ($35 \times 62\,km^2$ at 7 GHz for a 2 m diameter parabolic reflector at a height of 700 km, and $24 \times 42\,km^2$ at 10 GHz). Measurements are usually taken at both horizontal and vertical polarizations. A further consequence of the diffraction limitation of microwave measurements of SST is the presence of significant side-lobes (e.g. Kawanishi et al., 2003) which, in the vicinity of land, permits the leakage of terrestrial emission from a high emissivity source into the signal from the sea surface, with low emissivity, resulting in a degradation in the accuracy of the SST retrievals within ~100 km of coastlines. A further loss of SST retrievals is caused by the presence of heavy rain. Since the angular dependence of the apparent surface emissivity of sea water is large and dependent on the wind speed (Wilheit, 1979), there would be a strong variation in the BT signal across the swath of a linearly scanning microwave radiometer, so to avoid this complicating factor, satellite microwave radiometers use a conical scan with a constant angle of incidence of the field of view at the sea-surface, typically 50°–55°. As a consequence, the swath width of microwave radiometers with SST capabilities is typically < 1600 km from polar orbit, resulting in large gaps between successive orbits but these are generally filled in over two to three days.

5.5.1. Scanning Multichannel Microwave Radiometer (SMMR)

Two models of the SMMR (Gloersen and Barath, 1977) were flown, one on SeaSat in a drifting orbit from June to October 1978, and the other on Nimbus-7 in a sun-synchronous orbit from 1978 to 1994, with SMMR operations ending in 1988. Both had channels with SST sensitivity at 6.6 GHz and 10.7 GHz, but with a relatively small antenna at 60 cm diameter, the surface resolution was $95 \times 160\,km^2$ at 6.6 GHz and $60 \times 100\,km^2$ at 10.7 GHz. Prabhakara et al. (1983) attempted to assess the accuracy of the Nimbus-7 SMMR brightness temperatures at 6.6 GHz to represent the SST, as measured from ships, and confirmed the confusing influence of variations in wind speed and cloud liquid water. They derived empirical corrections which resulted in useful maps of SST being derived that indicated oceanographic patterns, such as the cool tongue of surface water in the equatorial eastern Pacific Ocean. A comparison with SMMR SSTs derived with corrections for water vapor, liquid water and wind speed through combinations of different channels and polarizations, and SSTs derived from drifting buoys deployed as part of the FGGE (First Global GARP Experiment, where GARP is the Global Atmospheric Research Program) during 1979 in the southern hemisphere revealed differences of ~0.6 K in the mean

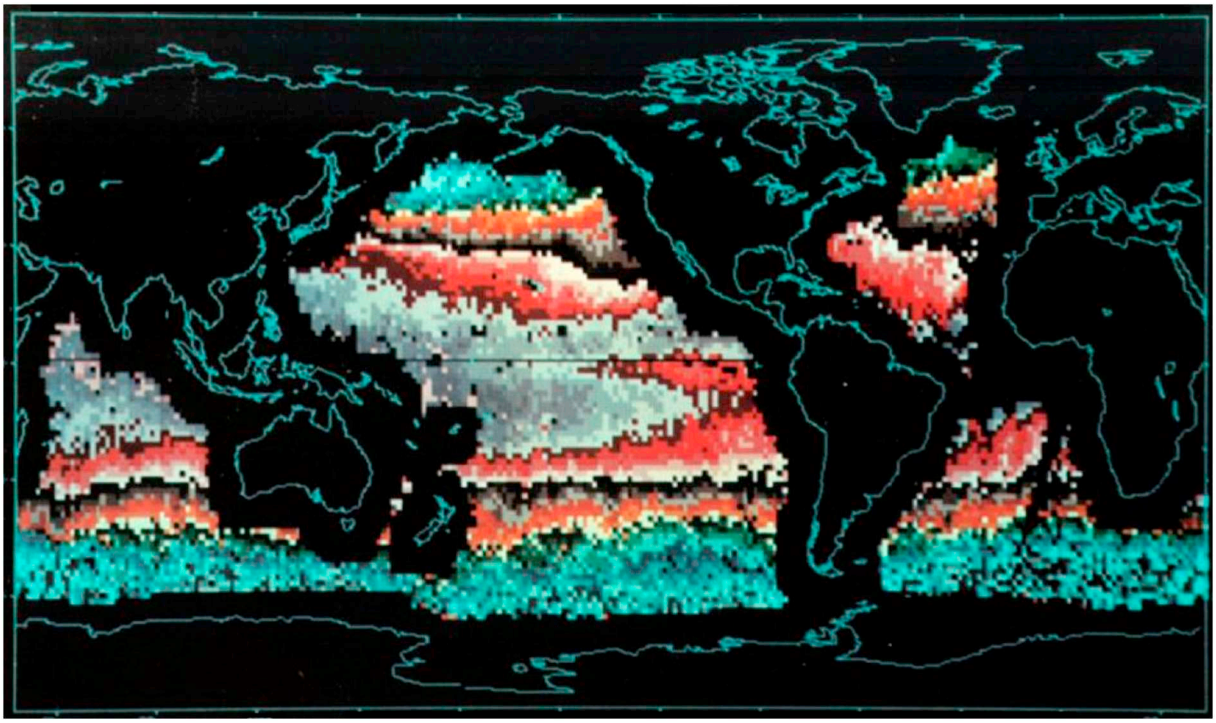

Fig. 12. Global SST's from SMMR, June 1979. Plate 1 of Gloersen et al., 1984.

and a standard deviation of ~1.76 K (Gloersen et al., 1984). Fig. 12 shows the global SST field derived from the SMMR on Nimbus-7 for June 1979.

5.5.2. TRMM Microwave Imager (TMI)

The Tropical Rainfall Measuring Mission (TRMM) satellite (Kummerow et al., 1998), a joint mission of NASA and the Japan Aerospace Exploration Agency (JAXA) launched in 1997, carried the TRMM Microwave Imager (TMI), which was a nine-channel microwave radiometer. The channels were centered at five frequencies: 10.65, 19.35, 21.3, 37.0, and 85.5 GHz, with four of them being measured in both horizontal and vertical polarizations. The 10.65 GHz channels confer a sensitivity to SST in the higher SST range found in the tropics, a capability that had been absent since the SMMR. The TMI complemented AVHRR IR SSTS by providing SSTs in the tropics where persistent clouds can be a problem for IR retrievals. The TMI swath width was only 759 km due to the low altitude of the orbit, and the low inclination of the TRMM orbit limited SST measurements to within 38.5° of the equator. The beam width of the 10.65 GHz channels produced an approximately elliptical footprint of 37 × 63 km^2, but the data were over-sampled to produce 104 pixels across the swath. Although originally planned for a three-year mission, TRMM ended in April 2015, after providing SSTs for 17 years.

5.5.3. Advanced Microwave Scanning Radiometer for EOS (AMSR-E)

The Japanese Advanced Microwave Scanning Radiometer for EOS (AMSR-E) was part of the payload of the NASA satellite Aqua. It was a twelve-channel, six-frequency, microwave radiometer that measured brightness temperatures at 6.925, 10.65, 18.7, 23.8, 36.5, and 89.0 GHz with vertical and horizontal polarization. AMSR-E had a parabolic reflector 1.6 m in diameter that rotated at 40 rpm to scan across the surface in a cone with an incidence angle of 55°, producing a swath width of 1445 km. As with other microwave radiometers, before and since, the calibration used the cosmic background radiation and an on-board warm target. The spatial resolution of the 6.9 GHz measurements was 74 km × 43 km but increased with increasing frequency, reaching 8.2 km × 14 km at 36.5 GHz (Kawanishi et al., 2003). The derivation of SST from microwave radiometer data requires the combination of measurements at different frequencies and therefore different footprint sizes (Gentemann et al., 2010) so the effective footprint size of the SST retrievals is not self-evident. A recent study (Boussidi et al., 2019) using SST_{skin} retrievals from MODIS on Aqua within the swath of AMSR-E has produced a reference footprint for the AMSR-E with 40 km × 60 km being the full-width defined as the point at which the magnitude has fallen to about e^{-1} of its central value (P. Cornillon (2019) pers. comm.). But many microwave-derived SST fields are produced at higher spatial resolution, indicating these fields are oversampled. The AMSR-E was decommissioned in October 2011 when the mechanism to rotate the antenna failed, after providing nearly a decade of valuable measurements.

In three-way comparisons with AMSR-E, AATSR and drifting buoys, O'Carroll et al. (2008) determined the AMSR-E SST observations have an uncertainty of ~0.42 K, comparable to the results of a subsequent analysis by Lean and Saunders (2013) who expressed their results as standard deviations for the years 2003 to 2009, ranging from 0.462 K to 0.500 K, with higher values in later years. In a three-way analysis including MODIS SSTs along with AMSR-E SSTs, Gentemann (2014) reported standard deviations of AMSR-E SSTs of 0.48 K. All of these three-way analyses were done using AMSR-E L2 (see Section 7 below) SST product distributed by Remote Sensing Systems (http://www.remss.com/missions/amsr/), with a 25 km retrieval grid. More recent versions were used in the later analyses. Comparable analyses using AMSR-E SSTs derived using different algorithms at different processing centers would not necessarily produce identical results.

5.5.4. WindSat

The US Navy launched a sun-synchronous polar-orbiting satellite called Coriolis in January 2003 into a terminator orbit, having equator crossing times of 6 a.m. and 6 p.m. Coriolis carries the WindSat microwave radiometer with bands at 6.8, 10.7, 18.7, 23.8, and 37.0 GHz. The 6.8 and 10.7 GHz channels are sensitive to SST. The conically-scanning 1.8 m reflector produces a swath of ~1000 km width with a native resolution of 39 × 71 km^2 of the low frequency channel (Gaiser et al., 2004). Meissner and Wentz (2007) assessed the accuracies of

WindSat SSTs by comparing global fields with those of AMSR-E and found a mean difference of −0.08 K with a standard deviation of 0.56 K, and in a smaller, regional comparison with M-AERI (Marine-Atmospheric Emitted Radiance Interferometer; Minnett et al. (2001)) SST_{skin} an RMS of 0.27 K. Comparisons between SSTs from WindSat and moored buoys in the Tropical Pacific Ocean resulted in an RMS difference of 0.36 K (L. Zhang et al., 2016).

5.5.5. OceanSat-1 Multi-frequency Scanning Microwave Radiometer (MSMR)

A series of sun-synchronous satellites for marine research was begun by the Indian Space Research Organisation (ISRO) in 1999 with the launch of OceanSat-1 with a Multi-frequency Scanning Microwave Radiometer (MSMR), which included channels at 6.6 GHz and 10.65 GHz, conferring an SST capability. The swath width was 1360 km. Comparisons with temperatures measured from five moored buoys in the Arabian Sea and the Bay of Bengal showed differences of −0.67 K with a standard deviation of 2.0 K; there were significant differences between day and night comparisons with the daytime values being better, and also with season as defined by the monsoon, with monsoonal values being better (Parekh et al., 2007). A more extensive comparison using drifting buoys in the Indian Ocean revealed a mean difference of −0.48 K with a standard deviation of 1.15 K (Muraleedharan et al., 2004). Although there were subsequent OceanSat missions, none included microwave radiometers.

5.5.6. HY-2 microwave radiometer (MWI)

A complementary series of satellites to the Chinese HY-1 polar orbiters, the HY-2 series, has microwave radars (altimeter and scatterometer) and a microwave radiometer (MWI). HY-2A was launched in 2011 and -2B in October 2018. The MWI has dual-polarized, low frequency channels at 6.6 GHz and 10.7 GHz thereby giving an SST capability. The surface resolution is 80 × 120 km^2 and 50 × 75 km^2, respectively. Comparisons with temperatures measured by drifting and moored buoys from NDBC (US National Data Buoy Center) gave a mean difference of −0.49 K with a standard deviation of 1.63 K, and with near-surface temperatures from Argo profilers (Roemmich et al., 2009) a mean difference of −0.28 K and 1.68 K (Zhao et al., 2014).

5.5.7. Advanced Microwave Scanning Radiometer 2

The second generation Advanced Microwave Scanning Radiometer (AMSR2) was launched on May 17, 2012, on the Japanese Global Change Observation Mission-Water “Shizuku” (GCOM-W1; Heygster et al., 2017; Kachi et al., 2017). GCOM-W1 is in the A-Train series of satellites with an ascending node at 13:30 (L'Ecuyer and Jiang, 2010). The diameter of the AMSR-2 reflector is 2.0 m, and, like AMSR-E, its rotation traces a conical scan with an angle of incidence of 55° at the surface. The channels of AMSR2 are the same as for AMSR-E with the addition of a 7.3 GHz channel to mitigate radiofrequency interference in the SST retrievals (Gentemann and Hilburn, 2015). An example of global SST derived from AMSR2 measurements is shown in Fig. 13.

Comparisons with in situ measurements of temperatures from drifting and moored buoys were found by Gentemann and Hilburn (2015) to give mean discrepancies of −0.04 K with a standard deviation of 0.55 K, with a small latitudinal dependence, and by Hihara et al. (2015) to be 0.21 K in the mean with an RMS of 0.49 K through comparisons with the TRITON moorings in the Western Tropical Pacific Ocean. Hihara et al. (2015) acknowledged the high mean difference could be a consequence of diurnal heating in the daytime comparisons whereas Gentemann and Hilburn (2015) removed daytime comparisons for wind speeds $< 6\,ms^{-1}$ to avoid the effects of diurnal heating.

5.5.8. The Global Precipitation Measurement Microwave Imager

Even before the end of the successful TRMM mission (Section 5.5.2), a follow-on satellite was being developed with a similar, but improved, suite of sensors. As with TRMM, the new satellite, the Global Precipitation Measurement (GPM; Smith et al., 2007) Core Observatory was planned to be in a drifting orbit so that over time diurnal variations would be sampled. The new satellite was launched on February 27th 2014, into an orbit with an altitude of 407 km and an inclination of 65°. The GPM Core Observatory carries a Microwave Imager (GMI; Draper et al., 2015), a conical-scanning radiometer covering a swath width of 550 miles (885 km) with thirteen channels from 10.65 GHz to 183.31 GHz. The 10.65 GHz channels, with horizontal and vertical polarization, have sensitivity to SST variations, but only for warm water, SST $> \sim 13\,°C$, as at colder temperatures the sensitivity decreases and the noise level increases (Gentemann et al., 2010).

6. Validation

As with all measurements, the success of the application of satellite-derived SSTs to research and to operational endeavors relies on an accurate and confident assessment of errors and uncertainties. As indicated in the previous section, such estimates of accuracy are generally derived by comparison with in situ measurements, and this requires the validating measurement to be of greater accuracy and lower uncertainty than the satellite data. The first satellite SST validation was reported by Allison and Kennedy (1967) from the Nimbus 1 High Resolution Infrared Radiometer (HRIR). But, it was not until the launch of the first AVHRR on TIROS-N that SST was routinely produced from space-based measurements. The initial validation of AVHRR SSTs, using the split-window MCSST atmospheric correction algorithm produced standard deviations of ~0.5 K at best (Strong and McClain, 1984), with mean differences of up to several tenths of a degree depending on the source of the validating data (McClain et al., 1985) and at these levels of accuracy, the contribution of the inaccuracy from the validating sensor and from the method of validation were not considered important, so the statistics of the comparisons were deemed to be an assessment of the accuracy of the satellite retrievals. As satellite sensors improved, along with the cloud screening and atmospheric correction algorithms, the differences between satellite-derived and in situ temperatures became much smaller, these other contributions could no longer be ignored. It was realized these contributions should be taken into account to determine a more meaningful estimate of the accuracy of the satellite retrievals of SST (see, for example, Corlett et al., 2014).

In situ measurements are available from many platforms (e.g. drifting buoys, moored buoys, ships, Argo floats). Each have different characteristics and also different performances, as presented by Castro et al. (2012) and Xu and Ignatov (2010) for drifting and moored buoys, and by Atkinson et al. (2014), for many other different types. Drifting buoys are the most commonly used type as they have several advantages: good geographical coverage, shallow measurement depth - typically 20 cm - and availability in near-real time through the GTS (Global Telecommunication Service). Argo floats, whose number has been increasing in recent years, have been recommended for climate studies; however, the uppermost measurement depth is about 5 m and relatively few are at the surface close to the time of overpass of a given satellite. The moorings of the Global Tropical Moored Buoy Array (GTMBA; McPhaden et al., 2010) provided long-term consistent measurements until the unfortunate degradation of the GTMBA in 2014 and are so far the best way to estimate the stability of satellite SST records (Merchant et al., 2012).

Given that the source of the IR radiation reaching the satellite is the skin of the ocean, the variable size of the thermal skin effect (Donlon et al., 2002; Minnett et al., 2011; Wong and Minnett, 2018) and variable diurnal heating decouple the SST_{skin} from the subsurface temperatures measured by in situ thermometers. Using well-calibrated IR radiometers on ships to measure the SST_{skin} provides validation measurements that avoid the contributions from variations in the temperature gradients across the thermal skin layer and possible diurnal heating.

Two types of shipboard radiometers that have been continuously

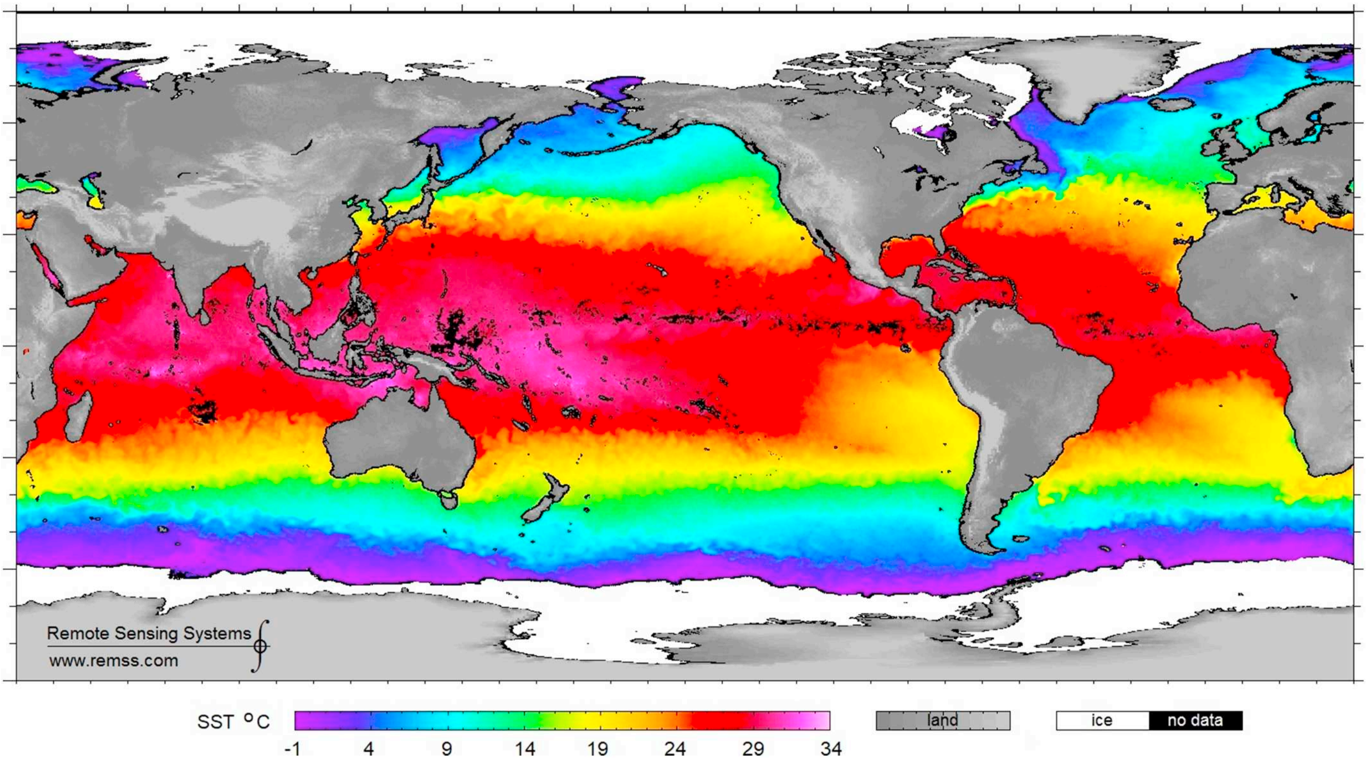

Fig. 13. Global SST distribution derived by compositing AMSR2 measurements over three days ending 21 November 2018. Credit: Wentz, F.J., T. Meissner, C. Gentemann, K.A. Hilburn, J. Scott, 2014: Remote Sensing Systems GCOM-W1 AMSR2 Environmental Suite on 0.25° grid, Version V.8. Remote Sensing Systems, Santa Rosa, CA. Available online at www.remss.com/missions/amsr. Accessed 24 November 2018.

deployed for many years for the validation of satellite derived SST_{skin} are the M-AERI (Minnett et al., 2001) and the Infrared SST Autonomous Radiometer (ISAR; Donlon et al., 2008). The M-AERI is a Fourier Transform Infrared Interferometer (Griffiths and de Haseth, 1986) that measures the spectra of IR emission from the ocean surface and the atmosphere from $\lambda = \sim 3\,\mu m$ to $\sim 18\,\mu m$ in ~2700 samples, with accurate internal calibration using two SI-traceable blackbody cavities, one of which is heated and the other is at ambient temperature. A gold-plated scan mirror directs the field of view of the interferometer to the ocean and the atmosphere (needed to correct the sky radiance reflected at the sea surface) and to the two blackbodies. A rain sensor is used to move the mirror to a "safe" position directed at one of the blackbodies when rain or sea spray is detected. SST_{skin} is derived from measurements around $\lambda = 7.7\,\mu m$ (Smith et al., 1996; Minnett et al., 2001) where the effects of cloud variability in the reflected sky radiance is much smaller than in the thermal IR atmospheric window at $\lambda = 10–12\,\mu m$, but where the emission depth at the ocean surface is very similar to those at wavelengths of the thermal window (Bertie and Lan, 1996). Running two M-AERIs side by side on a section from Hawaii to New Zealand produced SST_{skin} values from each instrument that were different by 0.005 K with a standard deviation of 0.077 K for 890 measurement pairs (Minnett et al., 2001). A recently revised error model of M-AERI SST_{skin} retrievals gives, for example, a median value for the total error of 0.041 K for 4600 retrievals during a recent research cruise in the Mediterranean Sea.

The ISAR operates on the same principle but uses a filter to define the wavelength passband of $\lambda = 9.6–11.5\,\mu m$. However, this choice of a wavelength interval where the atmosphere is very transparent in the IR increases the sensitivity of the SST_{skin} retrievals to errors introduced by cloud variability as, with all ship radiometers, the sky and sea view measurements are made sequentially. An analysis of at-sea measurements from the Scanning Infrared Sea Surface Temperature Radiometer (SISTeR; described by Donlon et al. (2014)), which has very similar measurement and operating principles to the ISAR, Donlon and Nightingale (2000) found cases where variable cloud fields could lead to errors in the SST_{skin} of ± 0.25 K and greater were possible. Nevertheless, an analysis of 12 years of SST_{skin} retrievals from ISAR from ships crossing the Bay of Biscay shows that 77.6% of the data are accurate within 0.1 K (Wimmer and Robinson, 2016). Donlon et al. (2014) give a more complete review of shipboard IR radiometry for satellite-derived SST validation.

Various approaches are used to control the quality of in situ data. Gross error checks, e.g. a 5 K cut-off relative to climatology, are commonly applied. The so-called blacklist approach is an automatic scheme that detects the platforms having anomalous statistics and blacklists them: UKMO makes a monthly blacklist by comparing drifting buoy SSTs and ship SSTs to those of OSTIA (Operational Sea Surface Temperature and Sea Ice Analysis; Donlon et al., 2012b), OSI SAF (Ocean and Sea Ice Satellite Application Facility of EUMETSAT) updates its blacklist every 10 days, using night-time SST differences between satellites and buoys, considering two satellites for a given buoy, when available (Marsouin et al., 2015). The in situ SST Quality Monitor (iQuam) developed at NOAA (Xu and Ignatov, 2014) is an elaborate scheme that routinely processes the in situ data (drifters, ships, tropical and coastal moorings) available on the GTS. Quality flags are assigned to each measurement through multiple tests, Bayesian and basic (e.g. track check, SST spike check). Files with quality controlled SSTs are available online (https://www.star.nesdis.noaa.gov/sod/sst/iquam2/).

Satellite-derived SST retrievals have been validated using several approaches: satellite-derived SST compared with in situ SST considered as a reference (Walton et al., 1998; Kilpatrick et al., 2001; Le Borgne et al., 2012a; Høyer et al., 2012; Marsouin et al., 2015; Kilpatrick et al., 2015), three-way analyses using two satellite-derived SSTs and one in situ SST (O'Carroll et al., 2008; O'Carroll et al., 2012; Gentemann, 2014) and a satellite-derived SST field compared to another satellite-derived SST field or an SST analysis (Dash et al., 2012; Le Borgne et al., 2012b). The first two approaches, based on collocated, coincident satellite and in situ data (matchups), aim to assess the SST accuracy,

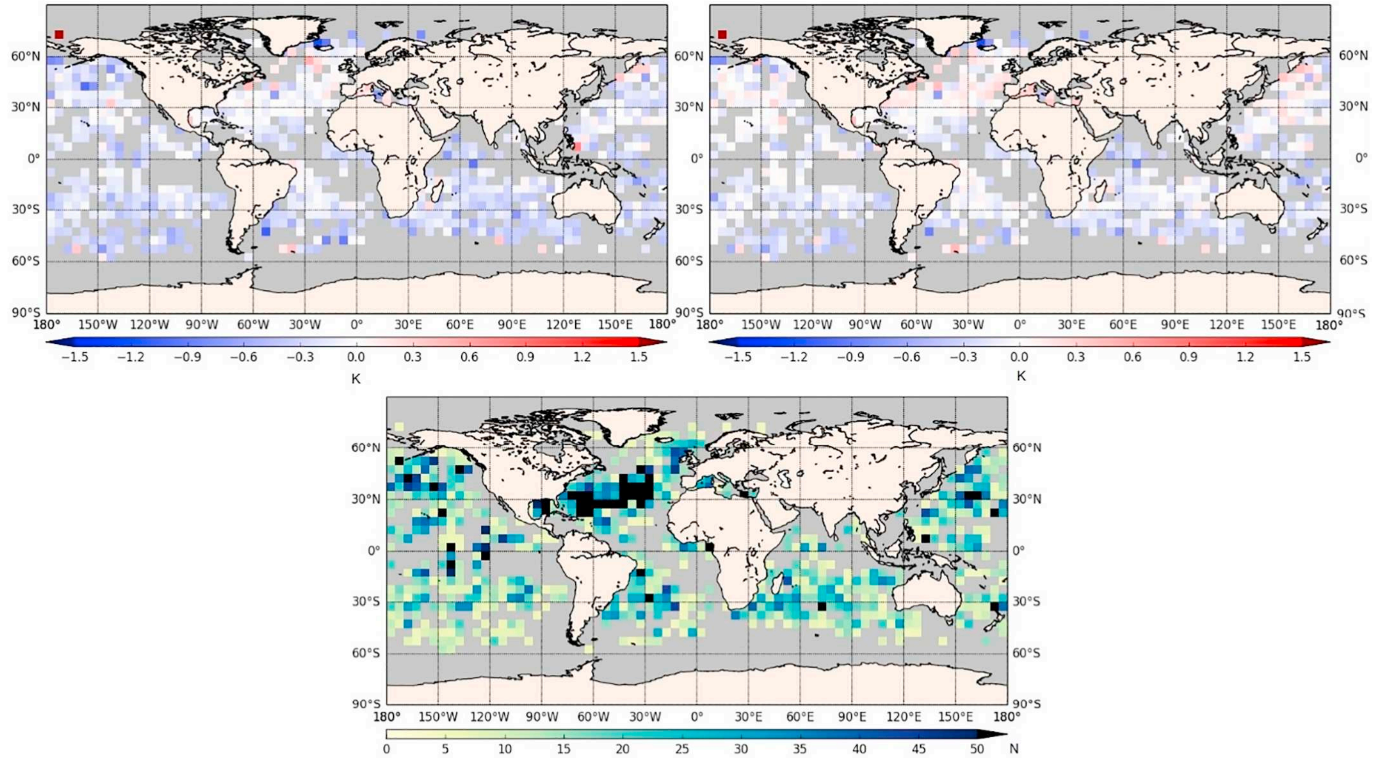

Fig. 14. Maps of the differences between Metop-B AVHRR and drifting buoys temperatures at night for October 2018. Top left: Mean differences (mean = −0.16 K, standard deviation = 0.53 K); top right: Median differences (median = −0.05 K, robust standard deviation = 0.39 K); bottom: number of matchups in 5° latitude × longitude bins – bins with < 5 matchups are excluded from the analysis. There are 14,560 cases. (Data produced by the OSI SAF; quality index data from 3 to 5 have been used.)

while the third approach may reveal defects or artifacts, undetected or hardly detected with matchups.

The assessment of satellite-derived SST accuracy is usually performed through the analysis of statistics computed on a set of collocated matchups between satellite-derived retrievals and in situ measurements. Statistics are computed globally or regionally and on time intervals ranging from daily to multi-annual depending on the data availability and the goal pursued (e.g. Marsouin et al., 2015). Mean and standard deviation are broadly used. In more recent years, robust statistics (Merchant and Harris, 1999) have been implemented more systematically because they provide an estimate of the accuracy that is less sensitive to outliers (cloud contamination or erroneous in situ value, for instance) and is therefore more representative of the accuracy of the retrieval algorithm (Fig. 14).

Statistics are often computed using daytime and night-time data separately because the cloud-screening and atmospheric correction algorithms usually differ and also because daytime comparisons to in situ measurements may be complicated by potential diurnal warming of the surface of the ocean (Section 3.2), of which the geographical extent and depth are very difficult to predict accurately. Also, the spatial resolution of the satellite-derived SST (pixel size) and the depth of the in situ measurement may significantly impact the accuracy assessment. This is particularly true in the presence of horizontal thermal fronts and other regions of high spatial variability, such as close to the coast or in the vicinity of sea ice.

The constraining time and space intervals applied to matchups should be as small as possible. These intervals are determined by the geographical zone, the coverage by in situ data, satellite SST temporal and spatial resolution and the need to obtain enough matchups. The time interval is mostly 2 or 3 h, with values varying from 30 min in AVHRR Pathfinder, MODIS and VIIRs matchups (Kilpatrick et al., 2001; Kilpatrick et al., 2015) based on ship measurements of temperature variability (Minnett, 1991), to 4 h (Walton et al., 1998). The spatial intervals vary from the satellite radiometer resolution (typically 1 km at subsatellite, to 2 × 5 km^2 at the swath edges) to 25 km (Walton et al., 1998). Research is continuing to define an optimal set of space and time intervals. Sub-pixel variability within 1-km MODIS SSTs was estimated to have a mean value of order 0.1 K by Castro et al. (2017). The spatial variability within a satellite SST pixel was further examined by Castro et al. (2018).

While it is convenient to state the accuracy of SSTs derived from a particular satellite radiometer and associated algorithms in terms of a mean error, often referred to as a bias, or a median error and a standard deviation (or robust standard deviation), there are multiple factors that contribute to inaccuracies in the satellite-derived SSTs. Some are reasonably well defined, such as the atmospheric path length that increases in a simple fashion across the swath leading to less accurate retrievals as the satellite zenith angle increases (Kilpatrick et al., 2015), while others less so, such as anomalous atmospheres (Minnett, 1986; Szczodrak et al., 2014). Thus, the error for the retrieval for each pixel should be constructed on a statistical expectation based on the conditions at the time of the satellite measurements. This is formulated in the GHRSST Sensor Specific Error Statistics (SSESs; Donlon et al., 2007).

Recently a new type of validation specifically aimed at assessing Climate Data Records has emerged, where both the SST and its uncertainty are validated (Fig. 15). For this the uncertainty in the SST is not estimated from the comparison to the in situ data but is instead estimated from a theoretical basis through an uncertainty model (e.g., Bulgin et al., 2016). Using the approach defined in Corlett et al. (2014), the distribution of satellite-in situ SST differences offers a way to assess the magnitude of the uncertainty derived from the theoretical model (Lean and Saunders, 2013; Bulgin et al., 2016; Nielsen-Englyst et al., 2018).

This new approach to SST retrieval uncertainty estimation and validation is resilient to the significant variations in both type and coverage of in situ SST across the years. It also offers a way to check the

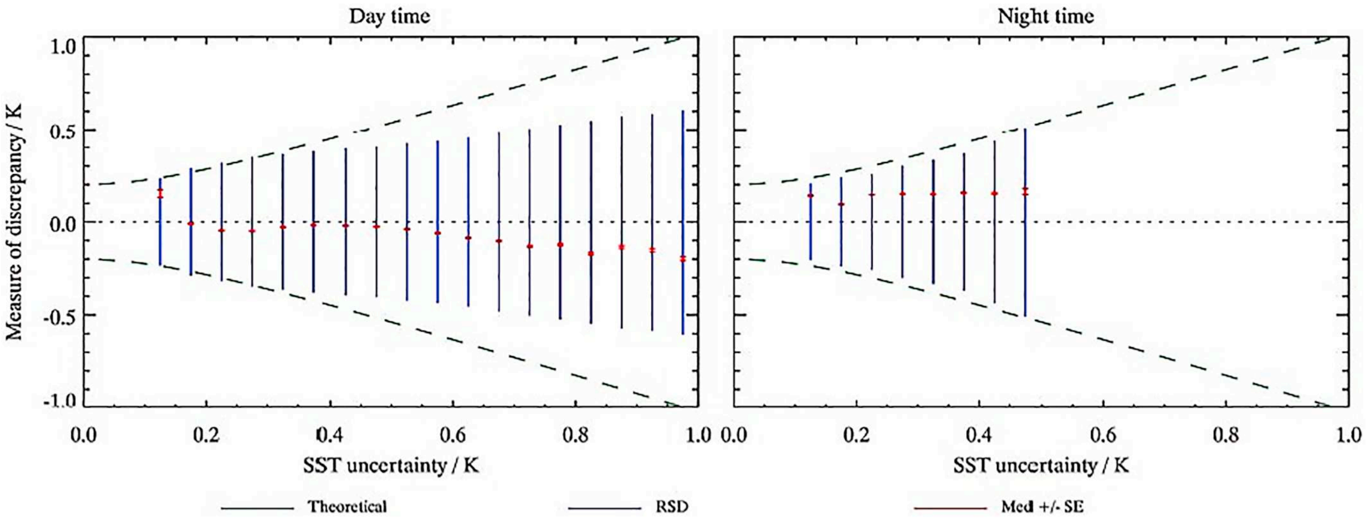

Fig. 15. Example of validation of an uncertainty model for ESA SST_CCI V1.1 NOAA-18 AVHRR SST products for (left) day time and (right) nighttime. Match-ups to drifting buoys are binned in terms of the product uncertainty; vertical blue lines indicate the measured dispersion for each uncertainty level and red dots indicate the standard error for each uncertainty level and also provide an indication of the number of match-ups. The dashed green lines indicated the theoretical dispersion of uncertainties (assuming an average drifting buoy measurement uncertainty of 0.2 K) if the product uncertainty estimates (and uncertainty models) are accurate. The agreement at night time is very good but the day time results show the product uncertainties were overestimated. (Corlett, G., 2018. Uncertainty_validation_example.jpg. doi:https://doi.org/10.6084/m9.figshare.7286168.v2.) (For interpretation of the references to color in this figure legend, the reader is referred to the web version of this article.)

stability in time of the uncertainty of the retrieved SST, which is of prime importance for climate studies. The GHRSST Climate Data Assessment Framework (CDAF; Merchant et al., 2014) gives guidelines on how to assess the stability and also on the criteria of selection of in situ data. The CDAF was developed from the methods given in Merchant et al. (2012) using the GTMBA; the method has recently been applied to drifter and Argo match-ups in addition to the GTMBA (Berry et al., 2018).

SST data producers usually assess their products in near real time or in a slightly delayed mode and often share results of their assessment with users through websites. More comprehensive online tools, such as the Summary Quality Monitor (SQUAM; Dash et al., 2010; https://www.star.nesdis.noaa.gov/sod/sst/squam/) and the Monitoring & Evaluation of Thematic Information from Space (METIS; http://metis.eumetsat.int/) enable interactive comparisons between various SST products (in situ, satellite and analysis). New open source software developments such as Felyx (Taberner et al., 2013) offer community tools for diagnostics and match-up generation.

7. Data processing progression: L2–L3–L4

After the SST values are retrieved from the satellite measurements, they are usually presented in three different data levels, called Level 2 (L2), Level 3 (L3), and Level 4 (L4) analyses (Parkinson et al., 2006). These levels are the most common forms in which the satellite-based SST data are archived and delivered to their “consumers”, from fishermen needing the most recent SST imagery to scientists studying long-term temperature trends as well as to the computers downloading the daily inputs for weather forecasting models. The three analysis formats differ in the way that the SST samples are averaged, interpolated, and combined with other SST data. The NASA definitions of the different data levels are summarized in Table 2, although others exist varying in details and often refined for the characteristics of particular sensors. The extent of averaging, interpolation, and combination increases from L2 to L3 to L4. The L3 and L4 data sets are “gridded”, meaning that the SST values are presented on a grid of prescribed geolocations (latitude and longitude coordinates, usually at a regular interval) to facilitate data use (such as visual displays). On the other hand, in general, the L2 data sets are not gridded, maintaining the original geolocation of each SST retrieval. An exception is the re-gridding of SST pixels derived from instruments on several geostationary satellites, for example the ABI fixed-grid SST fields (Harris Corporation, 2018). L2 fields are the most authentic representation of the satellite SST retrievals. Among the ocean surface parameters monitored from satellites, SST is unique in the large number of concurrent observations (both in spatial coverage and number of sensors and platforms), and the L3 and L4 analyses of SST are the device with which these heterogeneous data are coalesced. The higher-level analyses, in particular, could attempt to achieve more complete spatial coverage through multi-modality (IR, microwave, in situ) and higher accuracy through averaging of multiple coincident samples. Different versions of Level 3 fields are given in Table 3. The typical L3 and L4 data sets are also significantly more compact than their L2 counterparts in terms of data volume (i.e., total file size).

The L2 form is the standard format for the individual sensor data set, comprising the retrieved SST value, geolocation, and sample time for each SST retrieval. Most L2P data sets contain a wealth of additional information for each sample, including an estimate for uncertainty in the retrieval (typically, a standard deviation), and an array of quality flags that, for example, reflect the atmospheric conditions such as cloud cover affecting the retrieval procedure, and the atmospheric parameter values used in the retrieval and quality control procedures. An estimate of the difference between the derived SST and the foundation temperature is also typically given with every sample to facilitate oceanographic application of SST. Unlike most in situ SST data, the satellite retrieval should not be considered to be a point measurement of ocean surface temperature. The satellite measurement is already an average over the sensor “footprint” which is a surface area several km^2 in the IR and many hundred km^2 in the microwave. The geocenter reported in an L2 data set is hence an estimate of the center of the footprint. Moreover, sensor-level averaging is also applied mostly for reduction of instrumental noise. For example, the data from AVHRR, with a native spatial resolution of ~1 km^2, are acquired in three formats: High Resolution Picture Transmission (HRPT), Local Area Coverage (LAC), and Global Area Coverage (GAC). The HRPT data are full-resolution data transmitted to a ground station as they are collected. The LAC data are also full-resolution data, but the acquisition is recorded by an on-board tape recorder for subsequent transmission during a ground station overpass. The GAC data are derived from an on-board sample averaging, where

Table 2
NASA definitions of data levels.

Level 0	Reconstructed, unprocessed instrument/payload data at full resolution; any and all communications artifacts, e.g., synchronization frames, communications headers, duplicate data removed.
Level 1A	Reconstructed, unprocessed instrument data at full resolution, time-referenced, and annotated with ancillary information, including radiometric and geometric calibration coefficients and georeferencing parameters, e.g., satellite ephemeris, computed and appended but not applied to the Level 0 data.
Level 1B	Level 1A data that have been processed to sensor units (not all instruments have Level 1B data products).
Level 2	Derived geophysical variables at the same resolution and location as the Level 1 source data.
Level 3	Variables mapped on uniform space-time grids, usually with some completeness and consistency.
Level 4	Model output or results from analyses of lower level data, e.g., variables derived from multiple measurements.

After Parkinson et al., 2006.
See also https://science.nasa.gov/earth-science/earth-science-data/data-processing-levels-for-eosdis-data-products.

four out of every five samples along the scan line are used to compute an average value, and the data from only every third scan line are processed, yielding an approximate 4 km resolution at nadir. Further binning and averaging of these pixels by some agencies (e.g. the US Naval Oceanographic Office) result in the final GAC data resolution of these products of approximately 9 km.

Unlike the general L2 form, both the L3 and L4 analyses are gridded and are so designed to provide measurement-based SST values at a regular interval in space and time. Many L3 and L4 data sets today are given at a daily frequency, typically at noon UTC. A popular spatial interval is 1/4° in latitude and longitude, although finer grid spacings are also in use today while coarser grids can be found in long-term data sets that extend coverage back into the pre-satellite era. Typical contents of L3 and L4 data sets include the latitude and longitude coordinates of the grid, interpolated SST values over the grid-points, and an accompanying estimate of uncertainty for the SST values. Almost all of the L3 and most L4 SST analyses are derived from L2 data sets, with some L4 analyses ingesting L3 data as their inputs. The L2 samples are heavily quality controlled using the accompanying quality flags and other auxiliary data with typically much less than half of the available samples being selected. The traditional method for gridding is to sort the selected L2 samples based on their geolocation and time into space-time bins defined by the given spatial grid and time interval. The SST value of a bin is then computed as a weighted average of the values of all samples in the bin (with the weights typically defined by the inverse of the uncertainty variances). Gridding methods more sophisticated than this "bin-average" method are also in use today, as described below.

The main difference between the L3 and L4 forms is the data void: some L3 grid locations can be absent of data (marked as voids), while all L4 grid locations are filled with data. The data void in L3 data sets is typically inherited from the input L2 data. The grid bins without L2 samples simply become a void in L3. In satellite-based SST, the most significant data void in terms of the area affected is the cloud masking of IR SSTs. An L3 analysis can be derived from a single L2 data set or a combination of several data sets (Table 3). An example of the latter is the AVHRR Pathfinder SST data set which combines the AVHRR GAC data from NOAA-7, 9, 11, 14, 16, 17, and 18 satellites in order to produce a long-term data set with cross-satellite consistency (Kilpatrick et al., 2001; Casey et al., 2010).

Most of the L4 SST analyses are a combination of multiple lower level SST data sets, which are often used in a complementary manner. In particular, large and persistent IR data voids can be filled with data from microwave sensors which are less prone to cloud and water vapor contamination than IR sensors which nevertheless tend to provide higher horizontal resolutions. Data voids typically remain after binning of the combined data sets. There are two common ways to fill such voids: spatial interpolation and temporal extension. In the latter, the temporal extent of each bin is increased to more than a day (for a daily analysis), resulting in temporally overlapping bins that could collect from more samples to fill the bin. The assumption behind this technique is that the SST does not vary much during the binning duration, and for a 1/4-degree grid such an assumption is practically acceptable for a temporal bin length of a week or so (Reynolds and Smith, 1994). A common method for spatial interpolation, on the other hand, is the Bayesian statistical estimation based on a given prior distribution for the global SST field derived from some climatological mean field and/or empirical correlations over the ocean surface (Reynolds and Smith, 1994; Thiébaux et al., 2003; Donlon et al., 2012b). Bin-averaging mentioned previously is performed as part of this spatial interpolation procedure. Approaches based on principal component analysis or empirical orthogonal functions (Fig. 16) can be also used to obtain a spatio-temporal interpolation of the data (e.g. Kaplan et al., 1997; Alvera-Azcárate et al., 2005; Alvera-Azcárate et al., 2009). In order to combine SST retrievals and measurements from multiple types of sensors (IR, microwave, in situ) in a coherent fashion, inter-sensor bias fields are often computed empirically in advance to reduce the persistent discrepancy among certain data sets (Donlon et al., 2012b).

Currently, at least ten near real-time L4 analysis data sets of the daily global SST are in existence (Dash et al., 2010) reflecting their demand in operations such as weather forecasting. The ensemble variance in the analyzed SST values among the existing L4 data sets has turned out to be a better predictor for the difference between the in-situ SST observations and analyzed SST represented by the ensemble median value (Martin et al., 2012) than the formal uncertainty estimated for many of the individual analyses. The ensemble median itself has also shown consistently to be one of the most accurate SST analyses (at 1/4-degree resolution) in terms of comparison to the in situ observations (Dash et al., 2012; Fiedler et al., 2019), and comparisons of individual L4 fields with the median to which they contribute reveal the spatial and temporal characteristics of the deviations from the median (ibid). These results indicate great practical potential for L4 ensemble statistics, and that scientific investigations into their accuracy and mechanism behind it are appropriate. At present, satellite remotely

Table 3
GHRSST refinement of definitions of data levels.

Level 2P (L2P)	As L2 with uncertainty information as Sensor Specific Error Statistics derived from coincident satellite and reference measurements taken at the surface. Includes auxiliary fields for each pixel to help interpreting the SST data – sometimes referred to as Dynamic Flags.
Level-3 uncollated (L3U)	L2 data granules remapped to a space grid without combining any observations from overlapping orbits.
Level-3 collated (L3C)	SST measurements combined from a single instrument into a space-time grid. Multiple passes/scenes of data can be combined. Adjustments may be made to input SST data.
Level-3 super-collated (L3S)	SST measurements combined from multiple instruments into a space-time grid. Multiple passes/scenes of data are combined. Adjustments may be made to input SST data.

After https://www.ghrsst.org/ghrsst-data-services/products/.

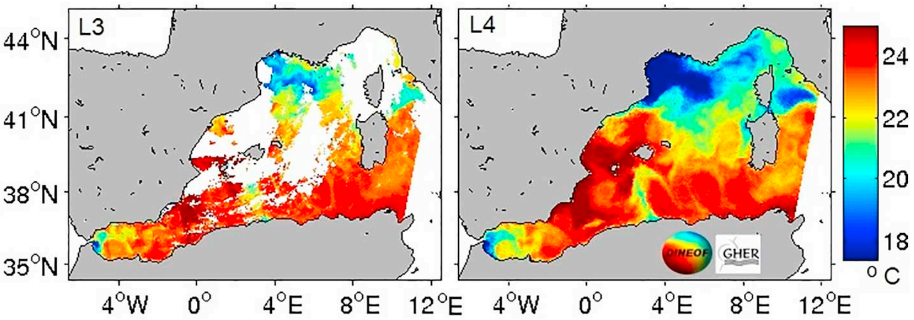

Fig. 16. An example of L3 to L4 SST interpolation using DINEOF (Data Interpolating Empirical Orthogonal Functions); (left): original VIIRS SST_{skin} data on 8 October 2018 and (right): DINEOF L4 SST_{skin} reconstruction.

sensed SST data sets are uniquely positioned to allow such statistical study due to the existence of multiple independent analyses.

There are other topics of investigation to improve SST analyses. One is the common practice of ignoring the correlations among the L2 samples during interpolation, a practice which tends to yield inadequate estimation of analysis uncertainty that reflects mostly the area density of the samples (Kaplan et al., 2003). Treating neighboring L2 samples as independent observations during Bayesian interpolation can also lead to numerical conditioning issues (due to discrepancy in bin weights between densely observed areas of the ocean surface and those without data) leading to visible artifacts in the analyzed SST fields, which turn out to be preventable simply by using a constant positive correlation value among all samples in every bin (Chin et al., 2014). This implies potential for improvements in the Bayesian interpolation procedure used for L4 (and L3) analyses. In particular, the prior distribution may need to be adaptable to the density of the L2 samples to be ingested. Another common practice to be improved may be the bin-average method itself. In standard bin-averaging, every L2 sample in a bin assumes the geolocation of the bin, effectively being “moved” to the center of the bin and truncating the geolocation values associated with the L2 sample. Truncation of sub-grid geolocation can smear ocean features such as SST fronts in an L4 analysis (Fig. 17), but smearing can be mitigated significantly by the use of non-constant (e.g., cubic) polynomials as the kernel function for interpolation (Chin et al., 2014). The bin-averaging procedure is equivalent to using a piecewise constant function as the kernel, which is the only “polynomial” that cannot encode sub-grid geolocation information. Finally, the daily frequency commonly used is likely not frequent enough to capture the sub-10 km scale SST features observable in the 1-km resolution L2 data sets. A sub-daily time window is found more appropriate to form an analysis at such a high horizontal resolution (Chin et al., 2017). A sub-daily analysis would be affected more directly by the diurnal SST variability than the current daily analyses, which tend to simply avoid the samples from areas of strong daytime warming (Donlon et al., 2012b; Chin et al., 2017). In summary, the technical issues noted here are especially relevant to analysis of high-resolution SST data and represent future topics of SST analysis: lopsided data density, fast-evolving sub-grid features, and diurnal variability. Handling of inter-sensor biases and inter-sample correlations, which have already been addressed as mentioned above, can also be considered as among the open issues in general SST analyses.

Finally, advances in computer power have ushered in a new approach to analysis of SST data, namely *data assimilation*. As noted above, the majority of the L4 SST data products available today are daily analyses reporting T_{fnd} (Fig. 2). Applications in weather forecasting require instead SST_{skin} at the interface of ocean and atmosphere sampled multiple times a day (e.g., every 3 or 6 h). Current operational practices often involve separate procedures interpolating the existing daily L4 SST data in time and estimating the skin temperature from the foundation temperature based on models of diurnal solar heating of ocean surface and associated measurements of insolation parameters and ocean surface winds. Recent increases in computational speed and storage, however, have enabled integration of these procedures into the forecast model itself, allowing direct assimilation of the L2 SST samples instead of their analyzed versions. An SST analysis would also be made a by-product of such a data-assimilative integrated forecast system, and such L4 analyses are packaged as emerging SST data products (e.g. Miyazawa et al., 2017; Li et al., 2019). Some of these systems have also integrated the traditional SST retrieval procedures (e.g., in a Radiative Transfer Model), so that the brightness temperature measurements from satellite sensors instead of the L2 retrievals could directly be ingested into a model of ocean surface to provide a L4 SST analysis (Li et al., 2019). An advantage of using ocean circulation dynamics to interpolate L2 data into L4 analyses via data assimilation is its potential to estimate the finer scale structures in a dynamically consistent way. In contrast, traditional interpolation schemes, such as Bayesian optimal interpolation, tend to smooth out the finer scale features. An integrated dynamical model, however, must also manage the variety of types and scales of data they ingest in order to balance the consistency and representativeness of their dynamical parameters. For example, while ocean circulation models are still refining their dynamics to resolve the location where the Gulf Stream separates from the American coastline into the North Atlantic Ocean (Ezer, 2016; Chassignet and Xu, 2017), the existing traditional SST analyses can usually pinpoint the separation

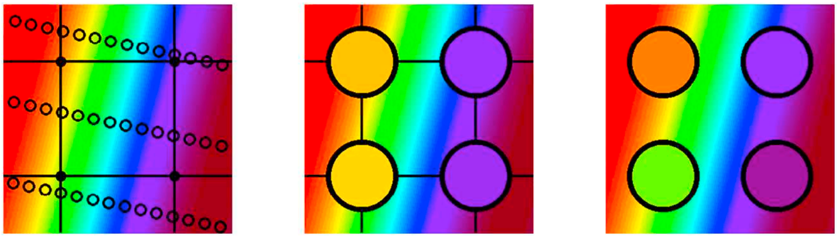

Fig. 17. Demonstration of a “gridless” interpolation and importance of avoiding truncation of geolocation data. Left: observations (open circles) are typically averaged at a nearest grid-point (closed circles) effectively truncating the subgrid portion of the location parameters. Center: such bin-averaging (colors inside big circles) can distort spatial information like the orientation of the front (background), due to the nearest-neighbor approximation of geolocation data. Right: a gridless interpolation method tends to ingest the observations at their original locations, reducing the distortion in front orientation, even at a low resolution shown. (For interpretation of the references to color in this figure legend, the reader is referred to the web version of this article.)

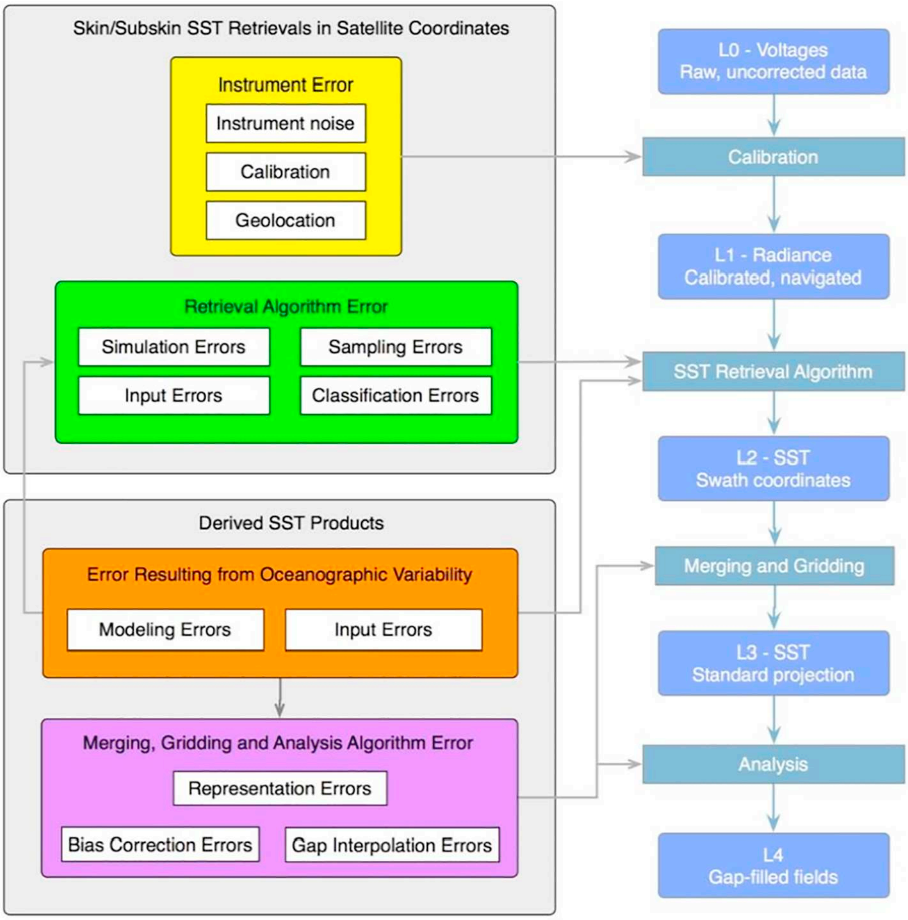

Fig. 18. Error budget framework with sources of errors and uncertainties (left column) and how they accumulate in the progression to L4 gap-filled SST fields (right column). From Wu et al. (2017), reproduced through CC BY 4.0.

point in general, and it remains to be seen if assimilation of SST (or associated brightness temperature) data would have enough numerical and dynamical influence to sufficiently correct the modeled three-dimensional circulation pattern, i.e., the course of the modeled Gulf Stream. As such issues are resolved, we should see more and more components of traditional SST analysis as well as retrieval procedures incorporated into dynamical forecast/nowcast systems, which could in turn become important sources of SST analysis data products.

The progression of satellite data through the processing levels makes the SST fields more accessible for many users but comes at a cost as each step leads to the accumulation of errors and uncertainties from many sources, as illustrated in Fig. 18 (Wu et al., 2017). L2 is where uncertainties in SST retrievals are derived by comparison with independent measurements in cloud-free conditions, but L4 fields are used to initialize climate models and in other climate studies. The accuracy assessed for SST fields from the same satellite radiometer, but at different Levels, is likely to be different; the uncertainties may be reduced at higher Levels by averaging multiple measurements in a grid cell, but may be increased due to additional processing steps and assumptions, and where L2 data are missing. Thus, the L2 SSESs may not be appropriate for L4 fields (Liu and Minnett, 2016; Liu et al., 2017).

8. Examples of regional studies

Clearly a great strength of satellite remote sensing of SST is the global sampling at high temporal and spatial resolution and thus the contributions of satellite-derived SSTs to studies of processes and particular regions have been very significant. Here we focus on two regions each presenting particular challenges but clearly benefiting from satellite data: the Mediterranean Sea and the Arctic Ocean. The Mediterranean Sea is a nearly landlocked sea with the atmosphere above it frequently influenced by continental air masses, including very dry, aerosol laden air from north Africa, which pose particular challenges to the derivation of SST in the IR. Nevertheless, the Mediterranean Sea is an important component of the global thermohaline circulation and given that it is less cloudy than many other regions, it continues to be a focus of research that incorporates analysis of satellite-derived SSTs. The Arctic Ocean, on the other hand, is a cloudy region which thus presents problems for the accurate retrievals of IR SSTs, as does the fact that the Arctic is an extreme case in the distributions of global atmospheric properties. Furthermore, because of difficulties in access and the harshness of the conditions for both researchers and instruments, the area is poorly sampled by in situ sensors placing a greater reliance on satellite remote sensing. The key role of the Arctic in the climate system also warrants a significant research effort.

8.1. *Mediterranean Sea*

The Mediterranean Sea is the most famous among the "Mediterranean seas". It is a mid-latitude semi-enclosed marginal sea that exchanges water and heat with the Atlantic Ocean through the shallow Strait of Gibraltar. The Mediterranean Sea is a concentration basin with an inflow of fresher (S ~36.2) and warmer (T ~15.0 °C) Atlantic water in the upper layer and outflow of saltier (S ~38.4) and colder (T ~13.5 °C) Mediterranean water in the lower layer through the Strait of Gibraltar. On an annual mean basis, the Mediterranean Sea loses buoyancy to the atmosphere through both an excess of

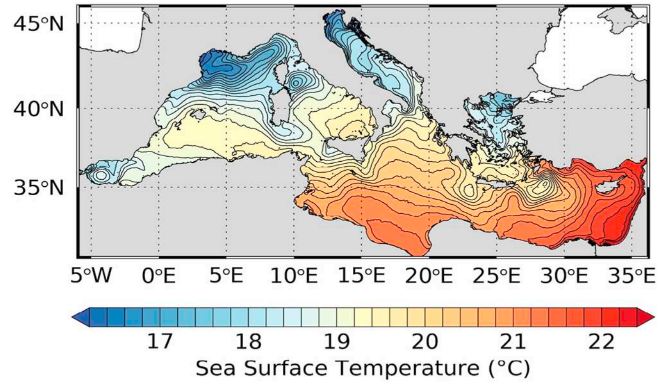

Fig. 19. Mean Sea Surface Temperature field in the Mediterranean Sea from 1982 to 2017 derived from CMEMS reprocessing.

evaporation over precipitation and a negative heat budget (Lacombe et al., 1981). The combination of all these air-sea exchanges as well as deep and intermediate water formation contributes to sustaining a basin-wide thermohaline circulation cell that can be viewed as a reduced version of the large-scale oceanic conveyor (Broecker, 1991). In this sense, as suggested by Robinson and Golnaraghi (1993), the Mediterranean Sea can be considered as a "small-scale ocean" where "many processes which are fundamental to the general circulation of the world ocean also occur within the Mediterranean, either identically or analogously". The direct consequence is that the Mediterranean Sea can be considered as a natural laboratory where field and numerical experiments can be conducted in more favorable dimensional and environmental conditions than for the global ocean. Satellite oceanography researchers also benefited from these favorable conditions; in particular sea surface temperature remote sensing has produced the longest record of valuable scientific results and practical applications.

The first satellite Mediterranean Sea application, recoverable from the web, was published in *Oceanologica Acta* in 1979 (Albuisson et al., 1979) and reported a first comparison between NOAA-4 VHRR and Aries airborne radiometer in the Gulf of Lions on August 3 and 6, 1976. They concluded that thermographic maps derived from VHRR data could enable users to determine the relative SST and study horizontal thermal gradients and their spatial distribution. Determining spatial thermal gradients and then detecting thermal fronts was the first most important result of the IR satellite remote sensing of the Mediterranean Sea during the 1980s, when a whole generation of Mediterranean oceanographers was fascinated by the possibility to observe, week after week, the evolution of the Mediterranean thermal fronts in the SATMER bulletin (SATMER, Bulletin Mensuel de Renseignements Oceanographiques Obtenus a Partir de Mesures Satellitaires Metéorologiques sur la Mediterrannée et l'Atlantique Nord-Est, Direction de la Metéorologie Nationale, Paris, France, 1984–1987).

Mollo-Christensen et al. (1981) reported one of the first applications of IR imagery of fronts, in their case off Cape Hatteras, to infer upper ocean dynamics. In the following year Crépon et al. (1982) demonstrated that a time series of thermal IR images obtained by the VHRR on NOAA-5 to detect thermal fronts in the Ligurian Sea can be used to determine the mean wavelength and phase velocity of the low-frequency waves associated with the evolution of the fronts. These waves were interpreted as large-amplitude baroclinic waves, finding a fairly good agreement with simulations using a two-layer ocean model. Additional studies of the Ligurian Sea based on IR images from the VHRR on NOAA-5 were reported by Millot and Wald (1980) and Wald and Nihous (1980).

A few years later, TIROS-N AVHRR thermal images from November 1979, were used to detect thermal fronts and measure wavelengths of the meanders of the Ligurian Current, relating them to the occurrence of baroclinic instabilities and small scale eddies detected during a field experiment (see Fig. 6 of Marullo et al. (1985)).

One of the first attempts to derive absolute values of SST from AVHRR data, considering the particular environmental conditions of the Mediterranean Sea, was proposed by Dalu et al. (1985). Their algorithm was based on radiative transfer model simulations and considered the specific Mediterranean conditions for water vapor absorption in the thermal IR. Validation was performed for a limited number of samples acquired in a field campaign in the Adriatic Sea. Since that time things have improved, moving from the laborious and expensive analysis of a relatively small set of images ingested from magnetic tapes to the time series analysis of years of daily or even hourly acquisitions downloaded from web-based servers. This was possible thanks to the initiatives of national and international institutions and agencies that undertook to archive, preserve and freely distribute petabytes of high level processed SST maps worldwide (Section 14). In the specific case of the Mediterranean Sea a crucial role has been played by European operational oceanography efforts which, in the 1990s, selected the Mediterranean Sea to develop a first prototype of observation and forecasting system. In this framework, MFSPP (Mediterranean Forecasting System Pilot Project) the MFSTEP (Mediterranean Forecasting System Towards Environmental Predictions) project and the first SST L4 operational products specific to the Mediterranean Sea were developed (Buongiorno Nardelli et al., 2003) and assimilated in near-real time in the Mediterranean Forecasting System (Pinardi et al., 2003). Of course, the Mediterranean Sea had been included in global L4 analyses since the 1990s (Reynolds and Marsico, 1993; Reynolds and Smith, 1994). The outcome of the European effort is now the CMEMS (Copernicus Marine Environment Monitoring Service) which has made the last 36 years of SST L4 data available to a wider community of scientific users. Fig. 19 shows the mean Mediterranean SST field derived from the average of all the CMEMS reprocessed daily SSTs maps from 1982 to 2017.

Before that time several attempts had been made that used a relatively long series of acquisitions to increase the knowledge of the description and the understanding of the Mediterranean circulation following the thermal signatures of eddies and currents. Today, such things can appear trivial but then, for the first time, baroclinic instabilities evolving along the Algerian Current in small-scale eddies traveling northward to meet the Balearic Front, it became apparent that a new era for the exploration of the sea had started.

This kind of approach, either based on time series of several full resolution AVHRR images or on the NASA PO.DAAC (Section 14.1) AVHRR Pathfinder SST Archive (18 km resolution at that time), produced interesting results and new understanding of the Mediterranean circulation as a result of combining previous information based on in situ observations and satellite thermal IR images (e.g. Marullo et al., 1999a; Marullo et al., 1999b; Hamad et al., 2005; Millot and Taupier-Letage, 2005). Such research has definitively proved that the key element that made possible the great progress in the knowledge and understanding of the Mediterranean Sea dynamics was the jump from the use of a few thermal images, produced by individual researchers, like the "icing on the cake" of analyses based on other data or models, to the analysis of long time series of maps, centrally and uniformly produced in dedicated facilities.

This pioneering work has opened the way to the more recent studies that made use of space-based IR remote sensing observations for advanced Mediterranean Sea investigations. In fact, starting from the beginning of this millennium, a consistent number of publications appeared dealing with basin-scale investigations and focusing on time scales ranging from hourly to interannual. A first re-analysis of the AVHRR SST maps of the Mediterranean Sea, starting from 1985, was published in 2007 (Marullo et al., 2007). This analysis also presented a validation of the product including the optimal interpolation scheme applied to produce the series of L4 SSTs and the evaluation of the stability of biases with respect to in situ data. With the lengthening of the series, remote sensing scientists began to glimpse the possibility of addressing the field of climatology. Since SST forms the longest, quality controlled and continuous series of satellite-derived ocean data, the possibility to estimate linear (at least) trends over large areas of the basin was considered a golden opportunity to promote, with modest effort, satellite oceanography (Nykjaer, 2009; Shaltout and Omstedt, 2014; Pastor et al., 2018). At the time of writing, one more year of L4 Mediterranean SST maps is about to be released by CMEMS (Section 14.3), extending the time series started in 1982 to the end of 2018: 37 years of quality controlled consistent SST data. This implies that not only significant linear and nonlinear trends (covering the positive phase of Atlantic Multidecadal Oscillation, AMO) can be evaluated but also that interesting oscillatory modes in the range of periods from quasi-biennial to ENSO can and have been detected (Skliris et al., 2012).

On shorter time scales, investigations to study the SST diurnal cycle have also benefited from satellite-derived SSTs. This has been feasible also thanks to the contribution of geostationary satellites making it possible to observe the Mediterranean Sea surface with frequencies compatible with the resolution of the diurnal cycle ($>$ 4 times per day as suggested by Sykes et al. (2011)). Particular attention has been paid to the Mediterranean Sea, as it is one of the world ocean regions where extreme diurnal warming events are more frequent (Fig. 3; Gentemann et al., 2008; Karagali and Høyer, 2014). This particular interest produced a series of publications that highlighted the contribution of high frequency satellite observation to reconstruct the variability of the diurnal SST cycle in the Mediterranean Sea to understand the physical mechanisms that modulate the intensity of diurnal warming events (among several: Merchant et al., 2008a; Le Borgne et al., 2012a: Marullo et al., 2014b; Marullo et al., 2016).

8.2. The Arctic Ocean

A defining feature of the Arctic Seas is the seasonal or perennial presence of a floating sea ice pack, formed locally during winter or advected by winds or currents. Where sea ice exists, the underlying ocean mixed layer is generally at or very close to the freezing point, except in leads and polynyas on calm, sunny days when the ocean may become warm within a surface melt layer (Richter-Menge et al., 2001; Vincent et al., 2008b). The lateral extent of Arctic sea ice has always been greater in winter than in summer, but in the past few decades dramatic summer melt-back (e.g., Cavalieri and Parkinson, 2012) has led to a large increase in the area of seasonally ice-free Arctic waters (Steele and Ermold, 2015; Haine and Martin, 2017). Thus, until recently, the topic of SST in much of the Arctic Seas was relatively uninteresting: the ocean remained at or near the freezing point all year round. This is not the case now, as ocean surface warming has become evident in many areas of the Arctic (Steele et al., 2008; Eastwood et al., 2011).

When the ice retreats, what exactly causes the ocean to warm? In the western Arctic Ocean, Steele et al. (2010) analyzed model output to determine that the largest forcing by far was net surface heating, largely from solar radiation; areas within ~100 km of Alaska were also influenced by lateral heat flux convergence, i.e. warm currents moving northward from the North Pacific Ocean via Bering Strait. Heat flux from below the mixed layer in summer is essentially nil, owing to strong stratification in the estuarine-like Arctic Ocean. The partition is likely different in the highly advective eastern Arctic Ocean near the Atlantic Water inflow, which is where the bulk of the Arctic Ocean's subsurface heat content enters (e.g., Smedsrud et al., 2013). In the Northeast Water Polynya in western Fram Strait, Minnett (1995) found the summertime surface heat budget of the open water to be dominated by the radiative terms, as was also the case in the North Water Polynya (Hanafin and Minnett, 2001). Given that clouds modulate the incoming solar radiation and the net IR flux at the ocean surface, Arctic clouds play a crucial role in determining the evolution of the SST (Minnett, 1999; Hanafin and Minnett, 2001).

Warming in the Arctic Seasonal Ice Zone (SIZ) has some unique properties. The western Arctic is very strongly stratified by freshwater inputs from rivers, net precipitation less evaporation, relatively fresh inflows from the North Pacific Ocean via the Bering Strait, and (seasonally) from sea ice melt (Aagaard and Carmack, 1989). The result is mixed layers in the summer SIZ that are 20 m thick or shallower (Peralta-Ferriz and Woodgate, 2015). In fact, winds in early-mid-summer are generally quite weak, so that stratification can extend right to the surface (Randelhoff et al., 2017). These conditions lead also to diurnal warming in summer even at high latitudes (Eastwood et al., 2011). Later in the summer, surface winds accelerate and mix warm SSTs downward, even while the net air-sea heat flux is still weakly downward (Steele and Dickinson, 2016).

Warming of seasonally ice-free Arctic waters has a number of impacts, e.g., on the marine ecosystem (e.g., Feng et al., 2018), on coastal terrestrial ecosystems (Uma et al., 2017), and on the atmospheric boundary layer (especially in fall when this heat is fluxed upward; Screen et al., 2013). This seasonal ocean surface warming in turn affects both the details of ice retreat (Steele and Ermold, 2015) and ice advance (Stroeve et al., 2016; Smith et al., 2018).

In situ measurement of SST and upper ocean conditions in the Seasonal Ice Zone (SIZ) is not easy, given the short period in which field work is generally possible (i.e., late summer open water for ship-based work, and late winter pre-melt ice cover for aircraft-based work). Traditional Arctic autonomous drifting buoys have been deployed on thick ice floes to maximize survival, which explicitly avoids the SIZ. A unique program focused on the SIZ is the University of Washington's UpTempO (Upper Temperature of the polar Oceans) buoy program, which deploys surface drifters with a thermistor string in the SIZ (http://psc.apl.washington.edu/UpTempO/). These buoys have been successful in measuring the vertical extent of seasonal warming, the presence of diurnal warming, and the process of fall cooling that sometimes allows a portion of summer heat to survive through winter under the mixed layer. Buoy data from two years in the Beaufort Sea have also been used to evaluate the performance of a large suite of global gridded SST products (Fig. 20; Castro et al., 2016). More work is needed on this subject, i.e. in different areas and different seasons. Other autonomous SST-measuring platforms are also being used in the SIZ, such as wave- and sea-gliders, saildrones, and even profiling floats.

Remote sensing of SST in the Arctic Seas is challenging, owing to the frequent and extensive summer cloud cover which hides the surface from IR satellite sensors. A further problem in the IR is the varying length of the sunlit part of the day round the year. In sunlit conditions, measurements in the mid-infrared window cannot be used because of scattering and reflection of sunlight, with the consequence that in summer, there is a limited opportunity for matchups with in situ data from the drifting buoys at high latitudes at night to generate coefficients for the atmospheric correction algorithms, and for assessing the accuracy of the derived SSTs. These issues in the IR enhance the role that microwave SST products should play in this region, although their lower resolution is limiting, especially early in the ice retreat season when open water areas are small. A positive note is that polar-orbiting satellites take many images per day at high Arctic latitudes, a capability that could allow for more detailed examination of diurnal warming and other processes, but one that has not been fully exploited to date.

What should global, gridded SST products provide in ice-covered waters? One option is to provide a foundation or mixed layer temperature, which (since it is in contact with ice) will be the freezing point of seawater. This is the traditional approach, where most products assume a value of $-1.8\,^{\circ}\mathrm{C}$, appropriate for salinities of ~34. That is, a satellite sea ice extent mask is used to determine where to create “synthetic observations” of SST at this value, which are then blended in various ways with the true observed values in the open water to the south. A few products recognize the estuarine nature of the Arctic Seas, which results in large spatial variability of sea surface salinity. This means that the freezing point varies by up to perhaps 0.5 K over the region. There is also temporal variability, owing to recent Arctic Ocean

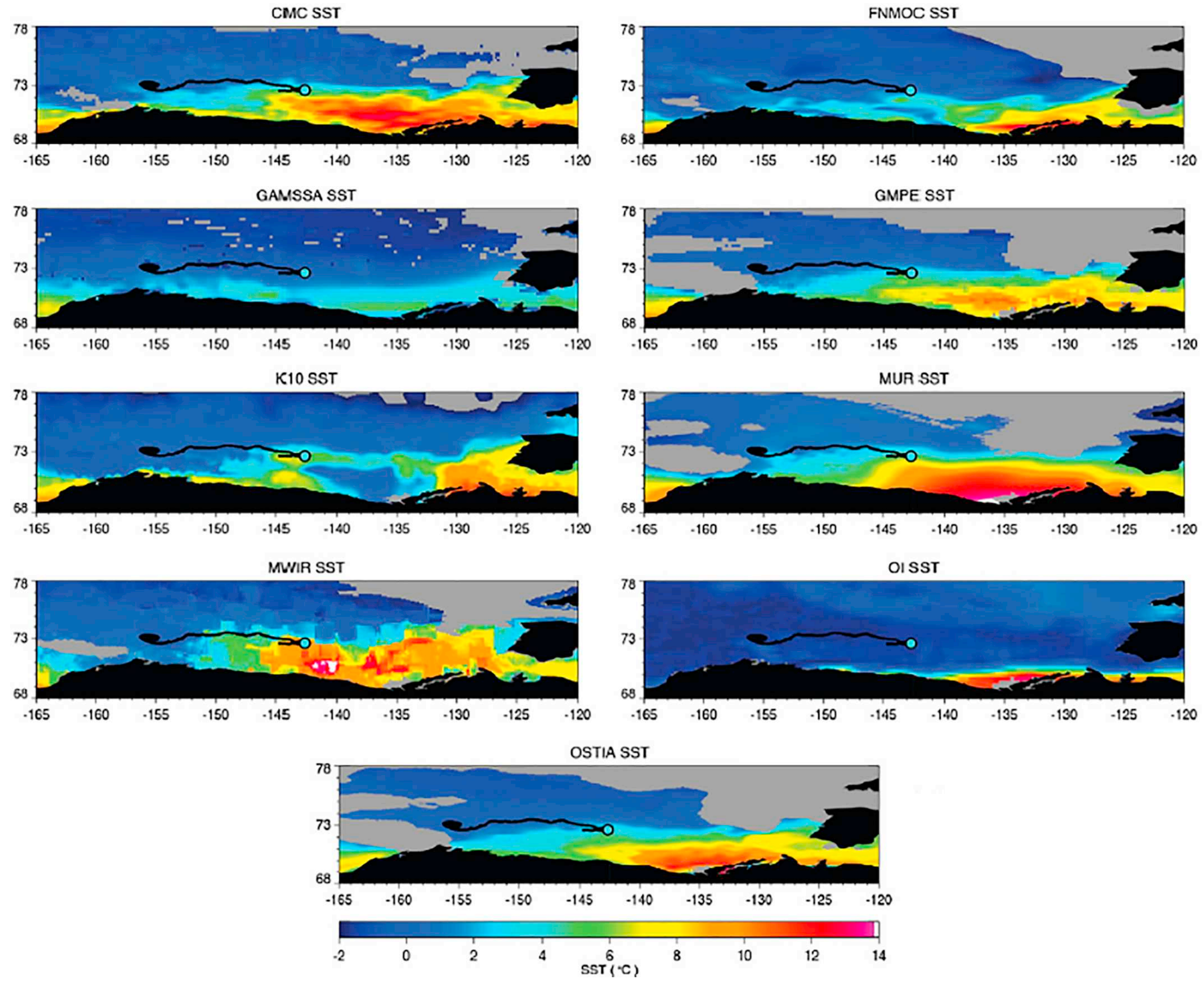
CMC SST

FNMOC SST

GAMSSA SST

GMPE SST

K10 SST

MUR SST

MWIR SST

OI SST

OSTIA SST

Fig. 20. Comparison of selected L4 SST analyses in the Beaufort Sea on 13 August 2012 (DOY 226). The color scale has been fixed to facilitate comparisons between products, and the trajectory of one of the drifting buoys (Louis 2012-03) has been plotted over the images with the circle showing the position of the buoy for that particular day and the color indicating the corresponding buoy temperature. The gray areas indicate that the respective ice mask has been applied, if available. Note that no ice mask is shown in the OISST since the ice and water masks were mistakenly inverted during this period and the buoy location was inaccurately flagged as ice covered. The anomalously low OISST temperature at the buoy location is a result of the improper masking. From Castro et al. (2016), with permission. (For interpretation of the references to color in this figure legend, the reader is referred to the web version of this article.)

freshening and large changes in salinity (Rabe et al., 2011). Furthermore, the algorithms for blending of synthetic freezing SSTs and open water observed values across the Marginal Ice Zone (MIZ) likely requires some updating in most products, as the MIZ has changed dramatically in recent years (Strong and Rigor, 2013).

Another option for a global gridded product might be to produce a blend of open water SST and ice/snow surface temperature in icy conditions. Some products are in fact available that provide this blend, which is most appropriate for, e.g., providing a lower boundary condition for atmospheric models. This can be difficult, however, in areas with mixed ice and open water. Further, ice/snow surface temperature is much more highly variable (spatially and temporally) relative to SST, owing to their lower thermal inertia.

In summary, deriving SST in seasonally ice-free Arctic waters is a new, relevant and exciting field, one that will only grow as the ice cover continues to shrink. These waters still suffer from a severe lack of in situ data for satellite validation, although new observational strategies are on the horizon. Ocean surface warming in the Arctic Seas is both a response to, and an active participant in, the large changes in sea ice cover we have seen and will likely continue to see in coming years.

9. Examples of applications

There are many global and regional applications of satellite-derived SSTs, such as forecasting and monitoring El-Niño-Southern Oscillation events (McPhaden, 2012), better understanding of atmospheric boundary layer response to SST variability (Perlin et al., 2014), assisting with efficient fisheries and monitoring ecosystem changes (Stuart et al., 2011), monitoring thermal stress threats to coral reefs (Mumby et al., 2004; Hedley et al., 2016), seeking signals that indicate changes in large-scale ocean phenomena (Liu and Minnett, 2015) and a warming climate (Casey and Cornillon, 2001; Good et al., 2007), better understanding air-sea fluxes of heat and moisture (Bentamy et al., 2011) and of CO_2 (Olsen et al., 2004; Wickramaratna et al., 2008; Wanninkhof et al., 2013), but here we focus on three applications that have very specific societal benefits: weather forecasting, development of severe storms, and sea level rise.

9.1. Numerical weather prediction

Accurate sea surface temperature data is vital for Numerical Weather Prediction (NWP) from a few days, to seasonal forecasts covering several weeks, to longer term climate variability. Most NWP systems use single (daily) spatially complete L4 SST analysis fields (e.g. OSTIA, Donlon et al., 2012b) as a boundary condition for constraining the atmospheric model (Thiébaux et al., 2003). Here we begin the discussion of contributions of SST fields to NWP with a focus on the use of daily fields, and then present results of the recent development at the US National Centers for Environmental Prediction (NCEP) to generate and use global SST fields at 6-hourly intervals.

9.1.1. Daily SST fields

Most L4 SST analyses used for NWP applications are smoothed to avoid shocks in the NWP model. Invariably L4 SST fields are of a temperature at an unknown depth – many aim to be a foundation temperature – and so near surface temperature gradients not considered in the forecast result in larger errors. Consequently, the error characteristics of L4 SST analyses are often not well understood and are not represented in subsequent applications. A more detailed review of the use of SST analyses in operational systems is given in Beggs (2010). SST patterns are dynamic and strong gradients in SST can impact the evolution of many atmospheric phenomena through its influence on surface winds (Song et al., 2006; Small et al., 2008; Perlin et al., 2014). For example, the benefits of OSTIA were shown in Donlon et al. (2012b), where the higher resolution of OSTIA reduced NWP forecast errors compared to a legacy SST product, by resolving, for example, small scale changes in the Arctic SSTs due to above average sea-ice loss in the summer of 2007 (Fig. 21). Seasonal patterns of SST change more slowly but strong signals associated with the El Niño, for example, can impact global weather patterns. Here, SST anomalies – the difference from a climatological mean – in the Niño 3.4 region are more useful in predicting changes (see, for example, Arribas et al., 2011).

A key requirement for NWP application is timeliness. For example, an SST analysis may be up to 48 h old when used in an NWP system at 00z if the timeliness of the SST analysis is not optimized for the NWP production time. Further, for reanalysis applications the recent satellite based SST analyses need to be aligned with the historical SST record from in situ measurements. Also, NWP requires global SST data to be stable over time and robust to changes in the satellite constellation.

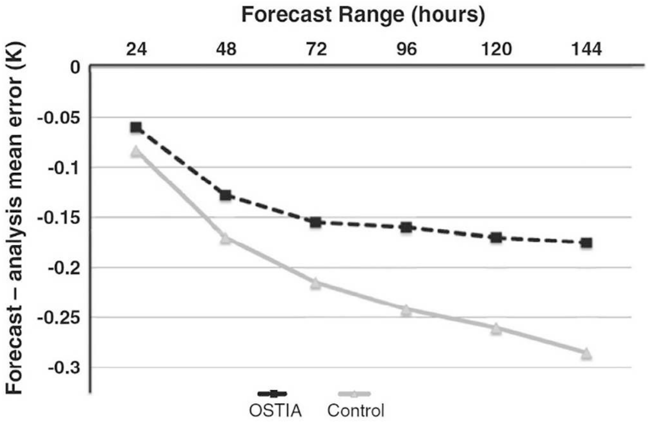

Fig. 21. An example of the improvement in the NWP forecasting skill when a more realistic SST field is used as the bottom marine boundary. The mean error in temperature at 850 hPa in the Northern Hemisphere when using old AVHRR and in situ low resolution SST data as a bottom boundary condition (gray line) and high resolution SST data from the OSTIA system (black line). The trial period was from 1st August 2007 until 31st August 2007. (From Donlon et al. (2012b), with permission).

9.1.2. Six-hourly SST fields

One SST analysis, referred to as the NSST (Near-Surface Sea Temperature) analysis, has been developed within the NCEP Global Forecast System (GFS), an integrated operational NWP system, to improve the resolution of diurnal heating and cooling by producing 6-hourly fields. In the history of the NCEP GFS since 1980, the thermal lower boundary condition has been provided by weekly OI SST (Reynolds, 1988; Reynolds and Marsico, 1993; Reynolds and Smith, 1994) initially, then daily RTG SST (Thiébaux et al., 2003) since 2015, and then 6-hourly NSST since 2017 (Li et al., 2019). Increasing the temporal resolution to capture diurnal variability in the SST is intended to improve the satellite radiance measurement assimilation over water surfaces.

One of the fundamental issues in SST analysis is the definition of the analysis variable. The foundation temperature, SST$_{fnd}$ (Fig. 2), is widely used in analyses such as OSTIA (Donlon et al., 2012b), the Canadian Meteorological Centre (CMC) analysis (Brasnett, 1997; Brasnett, 2008) and the Multi-Scale Ultra-High Resolution (MUR) fields (Chin et al., 2017). In the NCEP NSST, the analysis variable, T_f, is defined as the sea temperature at the base ($z = z_w$) of the diurnal warming layer. Thus, T_f is slightly different from SST$_{fnd}$ and evolves with time. The NSST profile, $T(z)$, incorporating diurnal warming and skin-layer cooling physics is simulated or parameterized in the atmospheric model to provide a prognostic lower thermal boundary condition for both atmospheric and radiative transfer models. Therefore, at a specific time, $T(z) = T_f(z_w) + T_w'(z) - T_c'(z)$, where, $T_w'(z)$ and $T_c'(z)$ are the simulated diurnal warming profile and skin-layer cooling profile respectively (Li et al., 2019).

The SST for air-sea fluxes calculation and skin-depth (or wavelength) dependent thermal lower boundary condition for the Community Radiative Transfer Model (CRTM; Han et al., 2006; Zou et al., 2016) over water surface can be provided when the NSST profile is available. For example, $SST = T(0) = T_f(z_w) + T_w'(0) - T_c'(0)$.

The T_f, an oceanic variable, as one of the analysis variables is incorporated into the atmospheric data assimilation system of GFS. All observations, including satellite radiances and in situ sea water temperature, are assimilated directly (without retrieval for satellite observations) with observation operators and their Jacobians provided by a Radiative Transfer Model and NSST model.

The major difference between NSST and the other SST analyses is in the way of handling the challenge that all the observations are indirect. In NSST, all observations are assimilated directly, including satellite radiances and in situ sea temperatures. In the other SST analyses, the radiances are converted to sea water temperature retrieval first, and the observations with diurnal warming signals are discarded according to some criterion. Additionally, NSST is able to take advantage of the well-established quality control and bias correction of the satellite radiances in the frequently-updated atmospheric data assimilation system. It is also a step towards the future coupled data assimilation.

The validation of NSST can be roughly divided into two stages: the first is to compare to RTG SST fields, the previous one used in operational GFS; and the second to compare to other SST analyses with the major goal being to understand the causes of differences and then find possible ways to improve the analysis. The Analysis (A) and Background (B) are the T_f analysis or background plus the diurnal warming amount at the observed depth. The observed depth, z_{ob}, is assumed to be 20 cm for drifting buoys, $T_w'^{bg}(zob)$, in NSST and used in the validation here. The Observation – Background (O – B) statistics for both in situ and satellite data have indicated improvement, with positive impacts on weather prediction being seen especially in the tropics. Here, verification against drifting buoy observations is reported. The statistics are calculated using 6-hour samples for a 10-day period. NSST is analyzed 6-hourly and the other three, OSTIA, CMC and MUR fields, are analyzed daily. The horizontal resolution of the NSST product is

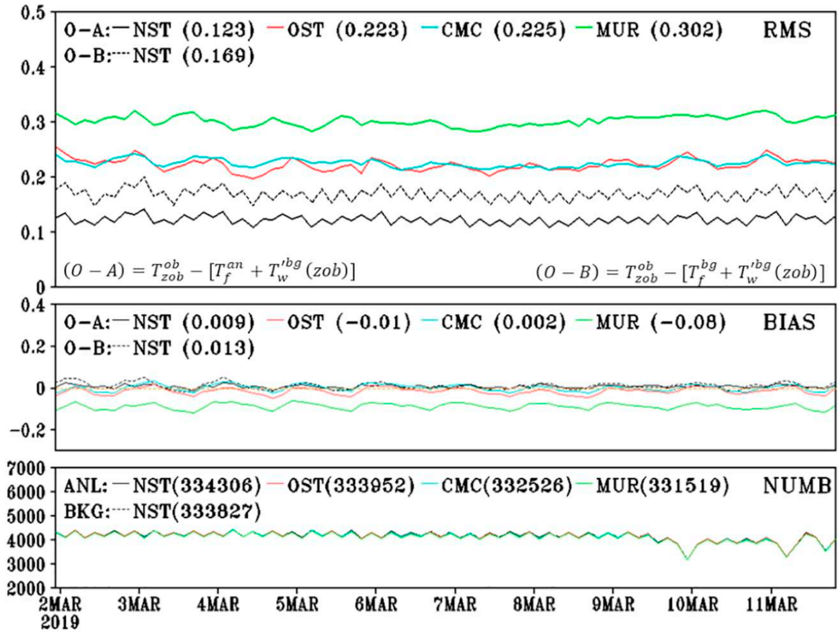

Fig. 22. 3-hourly verification against drifting buoys of four SST analyses. Global data for March 2, 2019 to March 11, 2019. The solid curves are for O − A = $T_{zob}{}^{ob} - [T_f^{an} + T_w{}^{\prime bg}(zob)]$, black: NCEP NSST (NST); red: OSTIA (OST); blue: CMC; green: MUR. The upper, middle and lower panel is for bias, root mean square and used counts respectively. The black dashed curve is $(O - B) = T_{zob}{}^{ob} - [T_f^{bg} + T_w{}^{\prime bg}(zob)]$ for NSST. (For interpretation of the references to color in this figure legend, the reader is referred to the web version of this article.)

about 25 km, but the analysis increment is generated at about 50 km grid spacing. For the comparison, the other three products are interpolated to NSST resolution with identical 4 consecutive 6-hourly analyses. For every 6-hour interval, the analyses at the NSST resolution are interpolated to the observed location to generate the O – A fields; O – B is available for NSST only. The drifting buoy observations are from the diagnostic files of the NCEP NSST analysis, the same quality control as NSST is applied to the other three analyses.

It is illustrative to see how well the OSTIA, CMC and MUR $\mathrm{SST_{fnd}}$ analyses compare to the drifting buoy observations which of course include diurnal warming and cooling signals. Fig. 22 shows the verification of four SST analyses, NSST, OSTIA, CMC and MUR, against global drifting buoy measurements. The (O – A) RMS difference is 0.123 K, 0.223 K, 0.225 K and 0.302 K for this 10-day period. The bias is nearly zero for NSST, OSTIA and CMC; MUR is slightly too warm. There is no significant difference in the observation counts. As expected, the NSST (O – B) is generally worse than (O – A). The basic features are stable with time, based on comparisons over much longer periods (not shown; Li et al., 2019).

In Fig. 23 the calculated diurnal warming at the observation depth, $T_w{}^{\prime bg}(zob)$, is not applied to the analysis or background. As is reasonable, this leads to larger RMS differences and smaller numbers of data counts. The bias increases from nearly zero to 0.070 K, 0.046 K and 0.061 K for NSST, OSTIA and CMC respectively. However, for MUR the negative bias is reduced from −0.08 K to −0.02 K. For small areas (not shown), the conclusions are basically the same, and the difference due the inclusion of $T_w{}^{\prime bg}(zob)$ is larger over more active diurnal warming area, such as tropics.

The validation has been repeated using other in situ observation platforms, including fixed buoys and ships. In comparison to temperatures measured from ships, NSST is significantly worse than OSTIA and CMC, and this is due to too large an observation error attributed to ship data. A smaller ship observation error will be used in the NSST in the future. From the inter-comparison with the other SST analyses, it has been found the NSST has issues in certain circumstances, particularly where observation coverage is poor. Improvements to the NSST production are underway, including the use of more observations especially microwave satellite radiances, using a more advanced background error correlation length and the better use of the SST climatology.

It should be pointed out, drifting buoy temperature measurements are ingested in all four analyses discussed here, and the fitness of the analyses to this observation depends on the weights given to these and to the background temperatures. Therefore, the (O – A) statistics are not the only metrics of the quality evaluation, and (O – B) is a better metric. A metric to evaluate the fit to satellite observations needs to be established even though it is acknowledged that it is not likely to be straightforward.

As NWP systems become more complex and move towards coupled ocean-atmosphere models (Miller et al., 2017) then the requirements for SST products increase. In a coupled system the SST is first assimilated into an ocean model, which then exchanges fluxes with the atmospheric model. Also, diurnally varying SST analysis systems are being developed (While et al., 2017) to reduce errors due to timeliness and for validation of coupled models. In the future, operational forecast centers will move to direct radiance assimilation to allow a more consistent atmospheric and oceanic processing across all sky conditions (Geer et al., 2018). However, SST will remain an essential diagnostic as it can be independently validated (see Section 6).

9.2. *Ocean heat content and severe storms*

The connection between high SST and Atlantic hurricanes has been long recognized as the ocean was seen as a source of heat to sustain a hurricane (Malkus and Riehl, 1960). In 1948, Palmen, used arguments based on atmospheric stability to conclude that SSTs > 27–28 °C are needed for hurricane formation, and Miller (1958) found a relationship between SST and storm intensity, also noting that hurricanes in the Atlantic Ocean were unlikely to form over SSTs below 26–27 °C. Merrill (1988) reported that SST > 30 °C were needed for the development of a severe hurricane. Before quantitative retrievals of SST from satellites, a climatological SST field or sparse data from ship-based meteorological reports had to be used. Making use of cloud images from early meteorological satellites, Ramage (1974) described the life-cycles of three typhoons in the South China Sea in 1970, and although he noted that SST > 30 °C was found in the area, the resolution and sampling of the SSTs caused him to conclude the SST “bore no apparent direct relationship to the typhoon intensity changes” but he did note that the SST was cooler after the passage of a storm.

Of course, it is not just the SST itself that is critical to the development of severe storms, but the ocean heat content (OHC) that is available to the storms though air-sea exchanges at the surface.

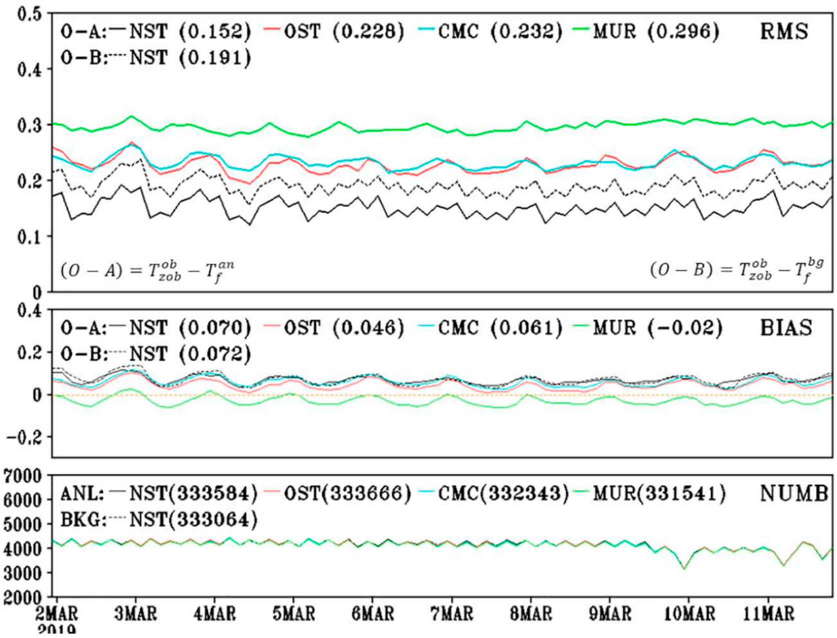

Fig. 23. As Fig. 22 but excluding the diurnal warming at the observed depth in the analysis and background fields.

Variations in the upper ocean heat content, derived by integrating the vertical temperature profile from the surface to some depth, usually taken to be the depth of the 26 °C isotherm, was shown by Shay et al. (2000) to be critical in understanding the development of Hurricane Opal in the Gulf of Mexico in 1995, highlighting the influence of the Loop Current and warm core eddies (Hong et al., 2000). The OHC can be estimated using SSH fields and sea-surface height anomalies (SSHA) derived from satellite altimetry (Shay et al., 2000).

Fig. 24 shows OHC in the Intra-American Seas (IAS), with high OHC in the Loop Current and the warm anticyclonic eddy field having provided additional thermal energy to major hurricanes over the past decade such as Hurricane Katrina in 2005, Hurricane Harvey in 2017, and Hurricane Michael in 2018. Some of the strongest North Atlantic Ocean basin hurricanes have occurred over the warm pool regime in the IAS (Fig. 25). This variability points to the importance of the OHC on hurricane intensity in the IAS. Examination of these hurricanes relative to OHC (Meyers et al., 2014) shows that they often reach maximum intensity over the high-OHC Subtropical Water of the Caribbean Sea, Florida Current, Gulf of Mexico Loop Current, or Gulf Stream, often weakening just before landfall (Rappaport et al., 2010). Approximately 70% of hurricanes with maximum winds > 120 knots (62 ms^{-1}) experience eyewall replacement cycles (ERCs) after reaching maximum intensity levels. Hurricanes subsequently weaken due to the combination of ERCs increasing shear, and movement over lower-OHC water. Hurricanes striking the US Atlantic Eastern Seaboard encounter similar oceanic environments passing over the Gulf Stream and then cooler shelf waters. Such behavior in hurricanes has become much clearer now that there is an evaluated OHC product available for forecasting.

A novel application of OHC maps and their daily progression is in predicting the behavior and migration of large predatory fish. While it has been understood for many years that ocean thermal fronts are a preferred environment for large marine predators, using tagged tunas

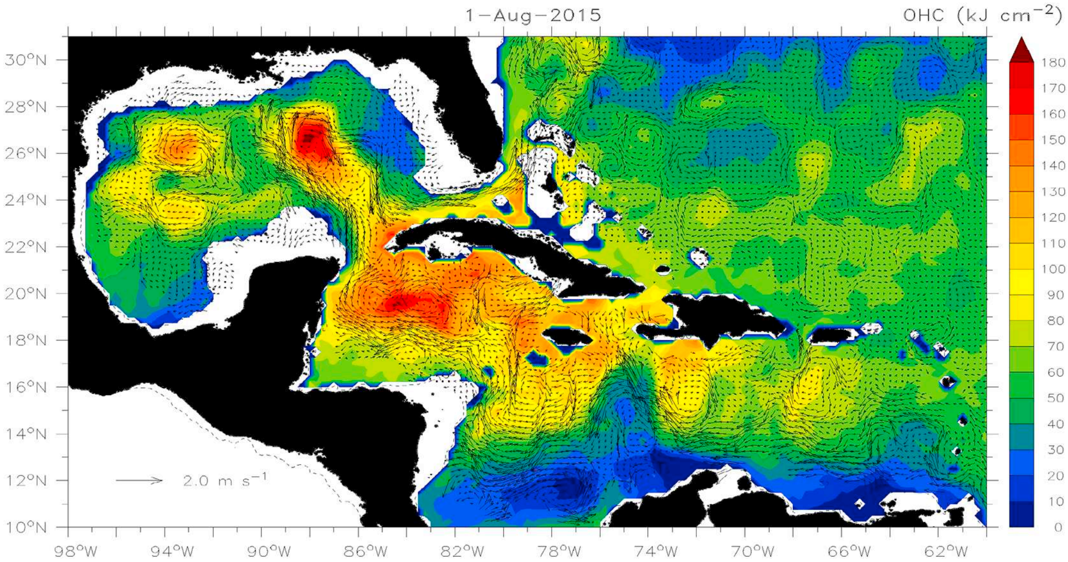

Fig. 24. OHC estimate (relative to 26 °C: color bar) and geostrophic velocity vectors from space-based measurements of satellite altimetry and SST on 1 August 2015 in the Intra-American Seas. (For interpretation of the references to color in this figure legend, the reader is referred to the web version of this article.)

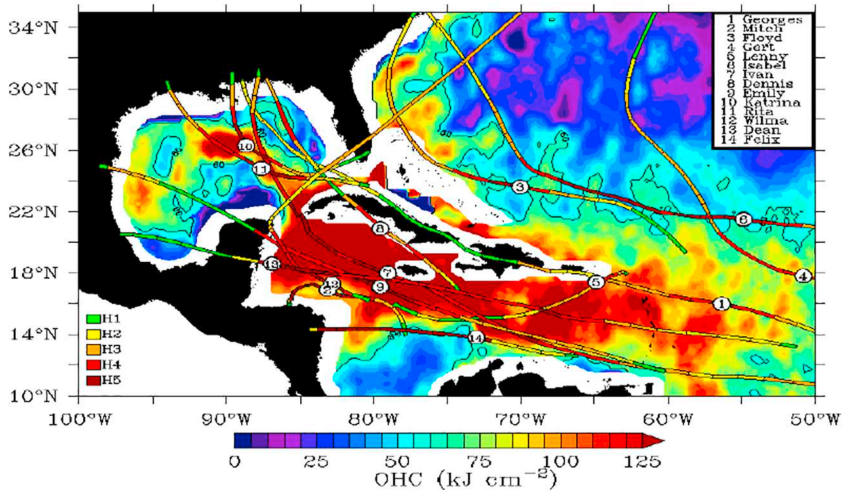

Fig. 25. Tracks and positions of maximum intensity for fourteen of the strongest hurricanes 1998–2011, plotted over OHC relative to the 26 °C isotherm for September 2005.

Luo et al. (2015) were able to demonstrate that the large horizontal variations in OHC are a potent predictor of fish behavior, even when the surface manifestation of fronts is weak.

9.3. Sea level

As the global population continues to grow, the largest rate of growth is found in coastal areas where there is an influx of people from the hinterland as well as continuing urbanization, which are expected to continue (Neumann et al., 2015). Many of the world's largest cities are in the coastal areas, often located in large deltas with low-lying surroundings, with ~10% of the global population living on land within 10 m of sea level (McGranahan et al., 2007). The greatest increase in coastal populations is in Asia, especially southeast Asia (Neumann et al., 2015). In addition to the loss of habitat by permanent submergence of low-lying coastal areas by the inexorably rising sea, coastal populations are vulnerable to other events exacerbated by rising sea-levels, including storm surges, tidal flooding, more persistent river flooding following extreme rain events, and flooding by tsunamis. Some events may be rare, but when they occur they can be devastating to both human populations and ecosystems (see the references in Neumann et al., 2015).

Measurements from tide gauges and satellite altimeters leave no doubt that sea-levels are rising, and that this increase in sea level is expected to accelerate (Nerem et al., 2018). There are two contributing factors to sea-level rise: increases in mass resulting from run-off from melting land ice, especially from Greenland and Antarctica (Rignot et al., 2011), and increases in volume as the ocean temperature increases and expands (Nicholls and Cazenave, 2010). Although there are significant regional variations in the rate of sea-level rise (Cazenave and Nerem, 2004) and some are caused by large scale phenomena such as ENSO (Cheng et al., 2008), the thermosteric expansion can be monitored using global satellite-derived SST fields with ocean and climate models (e.g. Han et al., 2010).

10. Operational oceanography

The high variability of ocean properties and the need for the assessment of the state of the marine environment require a continuous monitoring of the ocean environment at unprecedented resolution and quality. To respond to these requirements, Operational Oceanography (OO) became a branch of ocean science that routinely makes available high quality observational and model data for both fundamental studies and practical applications. Operational oceanography depends critically on the near real time availability of high quality satellite and in-situ data with a sufficiently dense space and time sampling. Observations are required to constrain ocean models through data assimilation and also to validate them. As a consequence, the evolution of OO that occurred in the last two decades strongly intersected with the evolution of the satellite observing systems, computer technology and improvement of models. Satellite retrievals of SST were the first high space and time resolution data available in real time. SST data were used to constrain ocean models through data assimilation and/or to serve downstream applications (Le Traon et al., 2015). The first prototype of the OO system was developed in Europe, in the late 90s when the implementation of operational oceanography in the world ocean was still at its infancy (Pinardi and Woods, 2002; Pinardi et al., 2003). The prototype was the Mediterranean observing and modelling system for operational oceanography developed by Mediterranean Forecasting System Pilot Project (MFSPP) that, starting from October 1998, was able to provide Near Real Time (NRT) observational data and 5-day forecasts of currents for the entire Mediterranean basin. During the MFSPP, a system for the acquisition and processing in NRT of satellite data (AVHRR at that time) was developed and became operational, providing NRT data and products to users (Buongiorno Nardelli et al., 2003). The SST processing system at that time included all the steps required to transform AVHRR L0 data into L4 SST analyses: the reception of the L0 raw telemetry AVHRR data stream via HRPT stations, L2 SST retrieval from IR measurements, automatic cloud screening, data quality control, L3 merging data of SSTs (5 to 6 satellite passes were available over the areas of interest) to produce daily L3 SSTs, a production of the daily-weekly L4 analysis using optimal interpolation techniques (Santoleri et al., 1991; Marullo et al., 1999a; Marullo et al., 1999b; Buongiorno Nardelli et al., 2003). During the MFSPP for the first time NRT SST were assimilated in MFS general circulation modelling every week and used to correct the atmospheric forcing to improve ocean forecasts. This prototype observing and modelling system was operational from October 1998 to the end of 2001, demonstrating the importance of an OO system at basin scale. Successive upgrades of the various components of the oceanographic system, including an SST component, were developed in the following years (Pinardi et al., 2003; Pinardi and Coppini, 2010).

At the same time, the Global Ocean Data Assimilation Experiment (GODAE) concept was developed with the aim to conduct a 10-year international demonstration of the feasibility and utility of real-time, global ocean forecasting (Bell et al., 2009). Thanks to the MSF success and GODAE effort, other OO projects started in Europe and worldwide. To respond to operational SST requirements of the modelling community, several international projects were launched: such as Medspiration by ESA, OSI SAF by EUMETSAT and the international GODAE High Resolution Sea Surface Temperature Pilot Project was established (GHRSST-PP, subsequently renamed the Group for High Resolution Sea Surface Temperature (GHRSST) (Section 13)) in 2001 (Donlon et al., 2009). The GODAE OceanView (GOV) has maintained strong links with satellite oceanography communities and major progress has been made over the past 10 years to develop and optimize the use of satellite observations for operational oceanography. The GHRSST partners offered, and continue to offer, a suite of tailored global high-resolution SST products, in near-real-time, on a daily basis, to support operational forecast systems and the broader scientific community.

The establishment of a political framework for the Global Earth Observation System of Systems (GEOSS; Lautenbacher, 2006) and the accompanying Earth Observation Summits have been the backdrop to the formation of a significant European contribution to GEOSS. The Global Monitoring for Environment and Security (GMES) initiative, subsequently renamed the Copernicus program, has been established in the course of the last decade to fulfill the growing need expressed by European policy-makers to access accurate and timely information to better manage the environment, understand and mitigate the effects of climate change and ensure civil security. MyOcean Projects implemented the European GMES Marine Core Service for the 2009–2015 period, and developed and tested in pre-operational mode the first concerted and integrated pan-European capacity for ocean monitoring and forecasting. The main results and recommendations of the GHRSST have been reflected in the design of the MyOcean sub-systems devoted to the development and production of satellite SST data (SST-TAC, Thematic Assembly Centre). The SST-TAC was developed, implemented and is now part of CMEMS. The SST-TAC is maintaining the operational chains for the production, validation and dissemination of the multi-sensor SST Level 3 data (more precisely L3S data) and L4 products for a total of 18 products covering the global ocean and the European Seas (North Atlantic, Baltic, Arctic, Mediterranean and Black Sea). Currently, the L3S and L4 data are built from all available GHRSST L2P IR measurements, and correspond to daily (night-time) gridded super-collated (multi-sensor) and optimally interpolated satellite SST estimates at High spatial Resolution (10 to 5 km) and Ultra-High spatial Resolution (1 km, as in the Mediterranean Sea, Buongiorno Nardelli et al., 2015) and hourly L4 SST products.

The other important impact of OO has been its role in defining the requirements for the space component. In fact, climate, science and OO applications share the same backbone system. Operational oceanography has, however, specific requirements for near real time and for spatial resolution. Operational oceanography requirements have been detailed in several papers and used by space agencies to define space segment and the characteristics of the latency and accuracy of operational data. For example, the needs of an ocean observing system was used to define the Sentinel-3 mission, dedicated to global ocean observations (Drinkwater et al., 2005; Donlon et al., 2012a). This role is still crucial and recently CMEMS has revised the space component requirements to take into account the evolving user requests. In particular, continuity of the present capability of the Copernicus Sentinel missions (Desnos et al., 2014) should be ensured and the request of a European passive microwave mission for high spatial resolution ocean surface temperature should be considered (CMEMS, 2017; Le Traon et al., 2019).

11. Climate data record

The concept of a Climate Data Record (CDR) was formally introduced in a National Academy of Sciences report (NRC, 2000) as being "*a data set designed to enable study and assessment of long-term climate change, with 'long-term' meaning year-to-year and decade-to-decade change. Climate research often involves the detection of small changes against a background of intense, short-term variations… The production of CDRs requires repeated analysis and refinement of long-term data sets, usually from multiple data sources.*" The report emphasized the need for "Data Stability," reasoning that "*because natural signals are often small, it is difficult to ascribe particular events or processes to climate change…* [so that] *long-term, high-quality measurements are needed to discern subtle shifts in Earth's climate. Such measurements require an observing strategy emphasizing a strong commitment to maintaining data quality and minimizing gaps in coverage.*" The Report states that "*long-term studies such as those needed for documenting and understanding global climate change require not only that a remote sensing instrument be accurately characterized and calibrated but also that its characteristics and calibration be stable over the life of the mission*". Data Continuity "*includes the continuous and accurate characterization of the properties that affect the construction of the time series. The most useful data for climate research purposes are time series that are continuous and for which the characterization of error, in terms of precision and bias, is known. Such errors should be minimized as much as possible in order to detect the often small, climate-related signal.*"

The Committee on Earth Observation Satellites (CEOS) has declared SST to be an Essential Climate Variable (ECVs; Bojinski et al., 2014) that has a high impact on the requirements of the UNFCCC (United Nation Framework Convention on Climate Change) and the IPCC (Intergovernmental Panel on Climate Change). SST derived from satellite measurements offers the best source of global, repeated fields, along with accompanying uncertainty characteristics. Compared to some other ECVs, satellite-derived SST can more readily produce a CDR as temperature is a base variable of the SI system (International System of Units; Taylor and Thompson, 2008) and as such, traceability to SI temperature standards is much more straightforward to achieve than other CDRs. An unbroken chain of calibration to an SI temperature reference for each source of satellite-derived SSTs is an important factor in generating SST CDRs with data from multiple satellite missions (Minnett and Corlett, 2012). The required accuracy for satellite remote sensing of SST for climate research and applications is very stringent, but it is a good target as in striving to achieve it we will generate data sets that can contribute to many research activities. The target accuracy, ± 0.1 K with a decadal stability of 0.04 K (Ohring et al., 2005), is very challenging not only to achieve but also to demonstrate convincingly whether these targets have been attained. Determining the accuracies of satellite-derived SST_{skin} by comparing them with independent measurements from using ship-board radiometers (Donlon et al., 2014), by being a comparison of "like-with-like," removes much of the error and uncertainty attendant when using subsurface temperature measurements taken from drifting or moored buoys (Minnett, 2003; Minnett and Smith, 2014). However, the number of ship-board radiometers is small, whereas the number of drifting and moored buoys is large, so that an optimal way forward to assess the accuracies of satellite-derived SSTs is to use both (Minnett and Corlett, 2012).

In recognition of the need to improve the consistency and the calibration of different satellite instruments providing measurements used to derive climate-relevant variables, including SST, the Global Space-based Inter-Calibration System (GSICS) was set up in 2005 by the WMO and the Coordination Group for Meteorological Satellites (CGMS) with membership of a number of national space agencies and meteorological agencies (https://gsics.wmo.int/en). The objectives of GSICS include ensuring the satellite radiometers are tested and calibrated pre-launch to SI-standards, the radiometers be intercalibrated on orbit with specific radiometers that have been identified to be stable and well calibrated, and that archives of satellite data can be reprocessed to produce stable and improved long-term data sets (Goldberg et al., 2011). Currently, the on-orbit reference radiometers are the IASIs (Section 5.2.2) on the Metop polar-orbiters (Hewison et al., 2013). A further aspect of GSICS is the monitoring of the satellite radiance measurements using NWP fields (Saunders et al., 2013).

The assessment of accuracies of satellite-derived SSTs using ship-board radiometers also contributes to establishing an unbroken chain of calibration to SI Standards (Minnett and Corlett, 2012). The internal

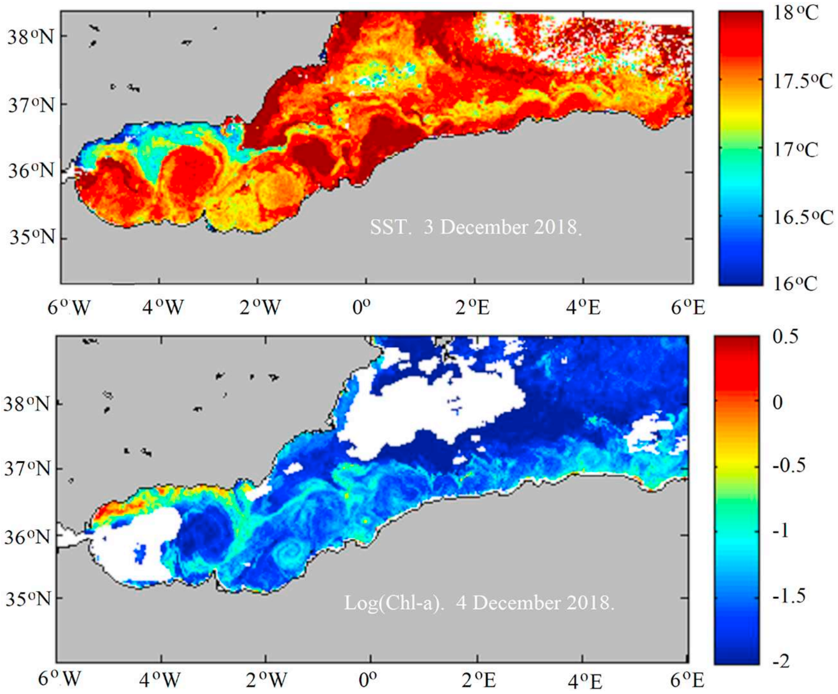

Fig. 26. SST on 3 December 2018 (top) and Chlorophyll-a concentration (units log(mg m^{-3})) on 4 December 2018 (bottom), western Mediterranean Sea, derived from measurements of MODIS on Aqua.

calibration accuracies of the ship radiometers have been checked periodically through a series of international workshops involving reference instruments provided by national metrology laboratories, the National Institute of Standards and Technology (NIST) in the USA, and the National Physical Laboratory (NPL) in the UK. The format of the workshops comprises assessment of calibrations of ship-board radiometers using metrology standard blackbody calibration targets, and an assessment of the accuracies of blackbody calibration facilities used by individual researchers in their laboratories through measurements of national standard radiometers. (Kannenberg and Palluconi, 1998; Rice et al., 2004; Barton et al., 2004; Theocharous et al., 2019).

12. Synergy with other remotely-sensed variables

The relation between SST and other oceanic variables has long been exploited to obtain a better understanding of the processes controlling the ocean, to assess the spatial and temporal scales of variability of these processes, and to study the ocean dynamics at these scales. Physical and biogeochemical processes are closely coupled in the ocean, with SST being a key variable that allows a link to be made between these different disciplines. Fig. 26 shows SST and chlorophyll-a concentration in the western Mediterranean Sea on 3 and 4 December 2018 respectively. The fields of eddies and fronts are clearly visible in the images, showing the link between ocean dynamics, SST and primary production. Multivariate studies of the state of the ocean have been performed ever since such satellite-based retrievals have been available, often in combination with in situ data in order to understand the vertical expression of the processes observed at the surface. Santoleri et al. (2002), for example, studied the circulation patterns in the Mediterranean Sea using a combination of altimeter, SST and chlorophyll-a data. The results were compared with in situ data in the Algerian basin and Adriatic Sea, and contributed to explaining mesoscale dynamics in these basins. Smyth et al. (2001) linked SST and chlorophyll-a imagery with Lagrangian measurements to study the biological response to upwelling at wind-induced offshore filaments. Access to real-time satellite imagery allowed the optimization of field sampling stations.

It is well known that upwelling-favorable winds bring deep, cold, nutrient-laden waters to the surface, which favor the development of phytoplankton blooms visible from space through their chlorophyll-a content. The joint study of SST and chlorophyll-a using satellite data supported, for example, the study of the evolution of biological patterns in time and their link to SST structures during an El Niño event in 1997 off the Chile coast (Thomas et al., 2001). Using satellite winds in addition to SST and chlorophyll-a, Murtugudde et al. (2004) also showed the influence of atmospheric patterns on ecosystem response for the El Niño event of 1997. As the satellite time series becomes longer, studies showing interannual variability in the relation between SST and chlorophyll-a concentration in the Pacific Ocean, related to changes in El Niño events, have become feasible (e.g. Thomas et al., 2012). On a smaller scale, Mauri and Poulain (2001) used SST and chlorophyll-a satellite data to study circulation patterns in the northern Adriatic Sea, identifying a link between river plume dynamics and wind events. More recently, Brando et al. (2015) used satellite-derived turbidity and SST data to track river plume water in the northern Adriatic after a major flood event. The use of multiple satellite variables might also lead to improved SST analyses, as the correlation between variables can be used to infer missing information about, for example, length scales of variability. Alvera-Azcárate et al. (2007) performed a multivariate analysis using SST, chlorophyll-a and winds to study an upwelling/downwelling event in the West Florida Shelf, and demonstrated that using jointly these three variables led to improved SST analyses. Li and He (2014) performed a similar analysis to study the multi-year relationship between chlorophyll-a and SST and the dynamics at the Gulf of Maine.

Ocean dynamics, expressed at the surface in the form of currents, fronts and eddies, have also very often a clear SST signature. The relation between sea surface height and SST can be therefore also used in studies aimed at describing the ocean circulation. Earlier studies (e.g. Carnes et al., 1994; Knudsen et al., 1996; Vazquez-Cuervo et al., 1996; Santoleri et al., 2002) had already pointed out the potential of exploiting the synergy between these variables. The joint use of SST and sea surface height, used to derive OHC (Section 9.2), can also help in deriving information about the ocean dynamics, such as improved representations of ocean currents (González-Haro and Isern-Fontanet, 2014; Rio et al., 2016). Recently, Rio and Santoleri (2018) demonstrated that the use of the information contained in high resolution SST maps leads to improved determination of surface velocities at spatial scales not resolved by the altimeter systems (i.e., below 150 km) but also at larger scales, where the geostrophic equilibrium might not be the unique or dominant process of the ocean circulation.

The data of SMOS (Soil Moisture Ocean Salinity; Drinkwater et al., 2009), Aquarius (Lagerloef et al., 2008) and SMAP (Soil Moisture Active Passive; Entekhabi et al., 2010; Piepmeier et al., 2017) have recently produced global measurements of sea-surface salinity (SSS). The relation between SST and SSS provides information about water mass formation and circulation patterns (e.g. Reul et al., 2014; Buongiorno Nardelli et al., 2016). The close relationship between SSS and SST is also used to improve the spatial resolution and to reduce noise in the satellite-derived SSS fields (Olmedo et al., 2018).

The evolution of satellite sensors, with more accurate data and higher spatial resolutions being resolved over the last decade, have led to works linking the meso- and submesoscale variability in different ocean variables. For example, Cotroneo et al. (2016) studied the evolution of a mesoscale eddy detaching from the Algerian current (Mediterranean Sea) using a combination of satellite SST and chlorophyll-a data with in situ high-resolution glider data, allowing them to study the dynamics of this structure and its impact on biochemistry. Pascual et al. (2017) performed a multiplatform experiment in the western Mediterranean Sea using satellite and in situ data to study meso- and submesoscale processes at an intense front. Satellite SST data were used to determine the strategy to sample an eddy at the Alboran Sea, and also to describe the physical and biogeochemical variability of this region, in combination with in situ data from gliders, drifters and Argo profilers.

13. The Group for High-Resolution Sea-Surface Temperature (GHRSST)

Since 2002, research into many aspects of SST, primarily satellite remote sensing of SST, and the transition of research results into operations has benefited from the actions of the GHRSST which plays a key role in coordinating international SST-related activities. The GHRSST is made up of scientists and operational practitioners from universities, research institutes, space agencies and operational forecast centers from many countries. GHRSST works closely with the Committee on Earth Observation (CEOS) SST Virtual Constellation (SST-VC). The group started out as the Global Ocean Data Assimilation Experiment (GODAE; Bell et al., 2009) High Resolution SST Pilot Project (GHRSST-PP; Donlon et al., 2007) and transitioned to GHRSST following the completion of GODAE. GODAE had set the GHRSST-PP the challenge of providing global near-real time (within 6 h) $<$ 10 km and 6–12 h resolution products with an accuracy better than 0.4 K (Smith and Koblinsky, 2001). In response, GHRSST established several practical steps to meet the GODAE requirements.

To provide data with sufficient sampling, a merging of all available data sources (satellite and in situ) was required. For this, GHRSST established a series of three key standards: first, GHRSST recognized the need to standardize the definition of SST itself, as data labelled "SST" would be coming from measurements made at different depths and times (Section 3) using different measuring techniques; second, to ease comparison, joint analysis, and merging SST data from different sources, a common data format (the GHRSST Data Specification, or GDS; https://www.ghrsst.org/governance-documents/ghrsst-data-processing-specification-2-0-revision-5/) was required; and third, an international framework (the Regional/Global Task Sharing, or RGT/S) was needed to coordinate SST data production from diverse sources and distribution to users. These standards have allowed GHRSST to ensure that data products meeting the requirements of GODAE are now available from its contributing entities.

As well as providing uniformity of file structure, the GDS also identified the process of transforming data across different levels (Section 7). In addition, it also specifies both a quality level and an uncertainty (in the form of Single Sensor Error Statistics, SSES), information that is now becoming more common across all Earth observation domains through initiatives such as the Quality Assurance Framework for Earth Observation (QA4EO; Fox, 2010). Indeed, this information is vital for producing higher level products as it offers a way to quantitatively merge data from multiple sources.

As SST datasets become more diverse and satellite data volumes grow (with the new generation of geostationary satellites for example), the role of GHRSST is arguably more important now than when the group was initiated. To address these new challenges, the Group is currently evolving the RGT/S framework to ensure seamless data provision to users well into the future.

Information on the GHRSST project may be accessed through the main home page at http://www.ghrsst.org.

14. Data handling, data sources and archives

In the half century of satellite remote sensing of SST, the methods available to distribute data to operational centers and researchers has undergone a revolution. Initially, data were mailed from receiving stations to researchers on computer-readable 9-track magnetic tapes and the processing of the data was a challenge, not least how to display imagery in a cost-effective but scientifically useful fashion, often as photographic prints. The growth in data volume that began with the ERS series in the early 1990s and more so with the NASA Earth Observing System in the early 2000s led to the formation of large data processing and archive centers, which coincided with the development of the Internet and the ability to deliver large datasets on a computer-to-computer basis using unified protocols. Currently, data access and remote processing and analysis of satellite-derived SSTs is no longer the daunting challenge it used to be, and many tools are available to researchers that facilitate the exploitation of large data sets in a wide range of applications.

Considerable progress has been made in providing users with a single point of entry for all SST data sets. The GHRSST page: https://www.ghrsst.org/ghrsst-data-services/services/ provides an overview of how to access the near real time (PO.DAAC; http://podaac.jpl.nasa.gov) and the historical L2 to L4 data (NODC; https://data.nodc. noaa.gov/ghrsst/ or ftp://ftp.nodc.noaa.gov/pub/data.nodc/ghrsst/). Yet, the numerous GHRSST data sets, while providing users with many sources, also creates the need to integrate information and tools that allow users to make informed decisions about which data set to use. This will be a major challenge for the future.

14.1. *Physical Oceanography Distributed Active Archive Center (PO.DAAC)*

The Physical Oceanography Distributed Active Archive Center (PO.DAAC) located at the Jet Propulsion Laboratory/California Institute of Technology, and NOAA's National Centers for Environmental Information (NCEI, and its forerunners) have been the lead centers for the distribution and management of SST products. The original NOAA/NASA Pathfinder AVHRR data set (Kilpatrick et al., 2001) was archived and distributed through the PO.DAAC. Processing of the data set was done at the University of Miami with the PO.DAAC undertaking post-processing from L2 to L3 for distribution and archiving. This was a major breakthrough in setting a standard for data providers and data managers working together to provide efficient distribution and tools and services for data extraction.

The AVHRR Pathfinder project led to a breakthrough in how to distribute high volume data. At a 4 km global spatial resolution, it required the implementation of new technologies for subsetting and extracting data on regional scales. The 4 km spatial global resolution made it prohibitive for users to download and easily work with the global data. This led to a breakthrough in implementing data format standards which included all the data processed and formatted in the Hierarchical Data Format (HDF). The PO.DAAC developed an interface and distribution tool known as PO.DAAC OceanESIP Tool (POET). This tool facilitated the subsetting of the Pathfinder data set. Additionally, it gave the user the flexibility to choose several output formats, including ASCII and ArcGIS (a tradename of a Geographical Information System). The POET tool was a major step forward in data distribution in several ways: 1) allowing data subsetting; 2) implementing data interoperability standards through a common format (HDF); 3) flexibility in allowing users different output formats for implementation in their own tools and software programs. The model used for the NOAA/NASA Pathfinder project was instrumental in moving forward with the GHRSST (Section 13).

Following on the success of the NOAA/NASA Pathfinder project the GHRSST project was one of the first to implement the common data format Network Common Data Form (NetCDF). The goal of satellite-derived SST data sets to be implemented in a common data format with compliant standards allowed for interoperability among all the satellite-derived SST data sets. This also allowed for a unique cooperation between NASA and NOAA to allow users access to both near real time and historical data. The GHRSST Data Specification Document (GDS) provided the framework for all data providers to process data into common formats, including specifications for data levels (Table 3). Implementation of tools such as the Thematic Real-Time Environmental Distributed Data Services (THREDDS), OPeNDAP, and the Live Access Server (LAS) allowed users to easily extract and subset data in both space and time. All the tools allow for subsetting of data and use the OPeNDAP protocol. Additionally, LAS allows the user to visualize the data, along with the extraction of time series at particular locations, as well as generate Hovmöller diagrams for both longitude and latitude. Other functionality with LAS, allows the user to save the data in netCDF, CSV, ASCII, or ArcGrid. The THREDDS server allows the user to aggregate the extracted data into one file. This is very useful when a user is extracting several years of data that consist of daily files. Issues with extracting large amounts of data were not due to the tool, but primarily the data format. These issues included tools timing out and/or having to submit multiple jobs to access the desired data over a certain period of time. A major breakthrough that occurred was the transition from NetCDF version 3 to NetCDF version 4, which allowed for internal compression, thus eliminating the need to decompress data before reading. Users could then extract and access larger amounts of data. Both LAS and THREDDS would have timeout issues with data sets such as the MUR SST data set, which is formed of files of daily, global gridded data at 1 km resolution. Conversion to NetCDF4 allowed users to easily access the entire time series of these data sets. This was critical for MUR, with data available since 2002, and the AVHRR_OI, with data availability since 1981. Overall, each tool provides advantages, depending on the user need, with OPeNDAP being a primary protocol used in both THREDDS and LAS. The THREDDS server primarily uses the NetCDF JAVA libraries, thus the conversion to NetCDF4 improved accessibility of the GHRSST data.

Effective June 3, 2019, NASA has retired their standard FTP protocol for data and information access. For more information on using the replacement service, PO.DAAC Drive, to access data please see: https://podaac.jpl.nasa.gov/announcements/2019-02-13_REMINDER_PO.DAAC_FTP_RETIREMENT.

As the GHRSST data sets span increasingly longer time periods and with the availability of high resolution (< 10 km) SSTs, challenges remain in distribution. These include implementing new methodologies for allowing users to extract large amounts of data in their particular areas of interest. Some examples of the challenges include extracting the NOAA/NCEI AVHRR_OI SST fields dating back to 1981 (Banzon et al., 2014). Another example is the daily MUR SST (Chin et al., 2017). Data from the Visible Infrared Imaging Radiometer Suite (VIIRS; Section 5.1.5) has sub-kilometer resolution. As these data sets are applied to coastal regions, for example, allowing users flexibility in applying quality flags and filtering is critical, interfaces that give users flexibility in filtering and gridding data will be a major challenge for the future.

Future directions for the GHRSST project and data management include a restructuring of the GHRSST Regional/Global Task Sharing Network (R/GTS) to a more federated approach. Data will be accessible through a centralized catalog. Data providers will have primary responsibility for maintaining data distribution and access. This would include implementation of THREDDS and OPeNDAP servers. Even with restructuring, many challenges remain. Many of these have to do with the access of higher resolution and longer time periods of data. A major challenge will not only be managing data, but also of information. The management of information needs to include documentation of error sources and uncertainties. This will be critical as an increasing number of satellite-derived SST products become available to the user community.

Part of the challenges will be in transitioning to cloud based technology that would allow for accessing and manipulating large amounts of data. This will be critical as high resolution data sets such as VIIRS become available over longer periods of time. Cloud-based technologies will allow for users to implement their own algorithms for gridding and optimal interpolation. A major hurdle to the user community will be implementing software on the cloud that allows for functionality beyond the traditional downloading of data and processing on a laptop. Cloud based solutions are currently being developed by both NOAA and NASA to prepare for these future challenges.

Additional challenges include the visualization of multiple data sets and accessing such data sets in near real time. The example in Fig. 27 shows an image of the SST anomaly derived from the MUR SST data set (Chin et al., 2017). The image was generated using NASA's State of the Ocean Tool (SOTO) (http://podaac.jpl.nasa.gov/soto). The SST anomaly is overlaid on a true color image from MODIS on Aqua. Blue colors indicate the surface cooling from the passage of Hurricane Michael which made landfall on October 10th 2018. Adding functionality to future tools that allow for not only data extraction, but also data manipulation and derivation of statistics will be a large focus of future development. This work will build on the groundbreaking web interfaces of the SST Quality Monitor (SQUAM; Dash et al., 2010) and the in-Situ Quality Monitor (iQuam; Xu and Ignatov, 2014).

14.2. Ocean and Sea Ice Satellite Application Facility (OSI SAF)

The Ocean and Sea Ice Satellite Application Facility (OSI SAF) is part of the EUMETSAT ground segment. Its primary aim is to provide users with sea surface parameters in near real time derived mostly from European meteorological satellites, and among these parameters is SST computed from IR radiometers on board polar orbiting and geostationary satellites.

Currently OSI SAF is distributing hourly L3C SST products derived from three geostationary satellites: Meteosat-8 above the Indian Ocean (41.5°E), Meteosat-11 in the 0°E position and GOES-16 (75.2°W); and L2P and L3C from instruments on two polar orbiting satellites: AVHRR on Metop-B (global and regional) and VIIRS on S-NPP (North Atlantic region). All products are delivered in NetCDF-4 format compliant with the GHRSST GDS v2. Near real-time and historical OSI SAF data can be accessed by several means including EUMETCast or FTP servers. Some products are also archived and available at the EUMETSAT Data Center (EDC) and at the PO.DAAC. Details on how to access OSI SAF products can be found on the “Access to data” page at https://www.osi-saf.org.

OSI SAF is also performing reprocessing activities. For instance, it has recently released an MSG SST data record (2004–2012) which was created using state-of-the-art methodologies.

Future OSI SAF activities are strongly tied to the future EUMETSAT meteorological satellite programs and as such will aim at providing the best possible SST products for the new generation sensors expected in

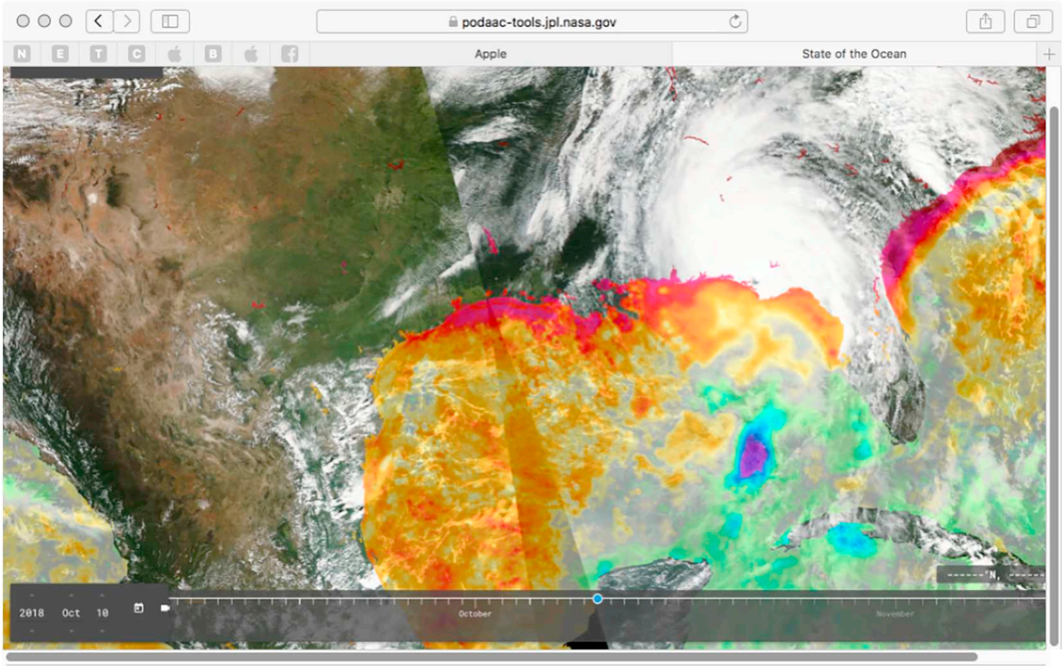

Fig. 27. The SST anomaly derived from the Multi-Scale Ultra-High Resolution (MUR) SST overlaid on a true color image from MODIS on Aqua. Clearly visible (blue colors) is the cooling of the Gulf of Mexico as Hurricane Michael made landfall on October 10th 2018. Image provided by JPL/Caltech/PO.DAAC. (For interpretation of the references to color in this figure legend, the reader is referred to the web version of this article.)

the next few years: Metop-Second Generation and Meteosat Third Generation.

14.3. Copernicus Marine Environment Monitoring Service (CMEMS)

The Copernicus Marine Environment Monitoring Service (CMEMS) is one of the six pillar services of the EU Copernicus program. CMEMS provides regular and systematic reference information on the ocean and sea ice state for the global ocean and the European regional seas (www.cmems.org). CMEMS today provides about 160 different products derived from observations and models which include 18 different SST products (see CMEMS catalog at www.marine.copernicus.eu) and serves a wide range of users and applications with > 15,000 users now registered for the service. SST observations are a fundamental pillar of the CMEMS added value chain that goes from observation to information and users (Le Traon et al., 2019). SST is the most downloaded observational product of CMEMS. Users require both global and regional products designed for specific European regions. These data are produced by CMEMS-SST-TAC (Thematic Assembling Centre) both for dissemination to external users and for use internally within CMEMS. CMEMS SST products are available in near real time and operationally assimilated by CMEMS global and regional modelling forecasting systems to produce ocean reanalysis and forecasts (Bell et al., 2000; Lellouche et al., 2018; Oddo et al., 2009). The CMEMS SST products are global and regional L3 multi-sensor SST and L4 analysis products, and are produced ingesting all L2 data provided by Space Agencies, using an ad hoc processing chain developed by the CMEMS SST-TAC. The processing chain includes additional quality checks of upstream data, bias adjustment among sensors, and interpolation techniques (e.g. Donlon et al., 2012b; Buongiorno Nardelli et al., 2013). SST L4 products at regional scales are characterized by improved spatial resolution with respect to global products reaching 1 km resolution, as for L4 Mediterranean SST (Buongiorno Nardelli et al., 2015). Multi-year reprocessed Products (MYP) are also produced and distributed by CMEMS, which are consistent time series covering the period 1982 to the present (Pisano et al., 2016). MYP SSTs are required to provide consistent descriptions of the ocean state over the past decades and are used by CMEMS to produce ocean monitoring indicators available on the web and to contribute to the Ocean State Report published every year (von Schuckmann et al., 2018). MYP SSTs are also assimilated by global and regional CMEMS MFCs (Monitoring and Forecasting Centers) to produce ocean reanalysis of the two decades. The SST TAC is responsible for ensuring the quality of their products by planning and implementing validation of their products, instigating quality control checks of incoming data streams and then monitoring the quality of the data produced. The SST TAC makes a continuous effort to include any new sources of data that are proven to improve the quality of the CMEMS output products, such as newly available satellite sensors. These new data sets, for example the SLSTR data from both Sentinel 3A and Sentinel 3B missions, are included in all regional and global products. Interaction with users is another important component of the CMEMS, for example via provision of quality information documents and user manuals and by responding to queries received through the CMEMS service desk.

15. Outlook

The outlook for the next decade and longer is very good, with continuation of current SST-capable satellite missions and the first launches of new radiometers. Data processing and distribution capabilities will no doubt continue to expand and provide increasingly effective support for research and operations, and the combination of improved sensors and algorithms will result in more accurate SST fields. A detailed discussion of requirements and recommendations to ensure continuing our SST capability through the next decade is given by O'Carroll et al. (2019).

15.1. Satellite instruments

We can confidently expect the continuation of VIIRS on the NOAA polar orbiters, SLSTR on Sentinel 3 series and several other IR radiometers described in Section 5 through the next decade and beyond. Similarly, the new generation of instruments on the current GOES and Himawari and on the new GEO-KOMPSAT-2 geostationary satellites will continue to provide valuable data.

In addition, new satellite series carrying radiometers with SST capabilities are planned to be launched in the next decade into both sun-synchronous polar and geostationary orbits. The first of the EUMETSAT Polar System - Second Generation (EPS-SG) polar-orbiters is planned for launch in 2022 and will carry a new class of visible and IR imager, METimage (Wallner et al., 2017) and the Infrared Atmospheric Sounding Interferometer - New Generation, IASI-NG (Bermudo et al., 2014; Crevoisier et al., 2014), both being significant developments of their predecessors on the Metop series. METimage will have 20 spectral channels, including a set of IR bands that correspond to those of MODIS for SST_{skin} retrievals, but with 500 m surface resolution at nadir with a 2670 km swath. IASI-NG will have improved spectral resolution and better radiometric accuracy than the IASI, but will have the same surface resolution of 12 km. Complementing the AHI, ABI and AMI on Japanese, US, and Korean geostationary satellites, EUMETSAT will launch the first of Meteosat Third Generation-Imaging (MTG-I1) three-axis stabilized satellites in 2021 with the Combined Flexible Imager (CFI) as part of its payload. CFI will have 16 channels, with surface resolution of 1 km in the visible and near-IR, and 2 km in the IR, including SST channels at $\lambda = 3.8\,\mu m$, $10.5\,\mu m$, and $12.3\,\mu m$ (Ouaknine et al., 2013; Durand et al., 2015). Full Disc Scans will have a basic repeat cycle of 10 min, and a European Regional-Rapid-Scan will have a repeat cycle of 2.5 min. When the CFI becomes operational, the globe will be sampled from geostationary orbit by new generation imagers at 2 km resolution at nadir and 10-minute temporal resolution. The constellation of satellites with microwave sensors with SST capability remains fragile and vulnerable to instrument failure. A major breakthrough would be the development of a high-resolution microwave sensor, such as the Copernicus Imaging Microwave Radiometer (CIMR) which is a candidate mission within the European Copernicus Expansion program (Kilic et al., 2018). The proposed CIMR would have channels at 1.4, 6.9, 10.65, 18.7, and 36.5 GHz giving it sensitivity to SST and also SSS, wind speed and sea ice concentration. The CIMR design is a conically scanning microwave radiometer with 7 m antenna, giving a spatial resolution of 15 km, about three times better than that of AMSR-2, and an ability to retrieve SST within 35 km of the coast.

15.2. Validating sensors

The drifting buoy array used in the validation of satellite-derived SSTs has evolved during the last three decades. At first, the common drifter type was based on the ARGOS system for geo-location and data transmission, SST resolution was 0.1 K and position and SST measurements were asynchronous. The migration to a new drifter type, called HRSST-1, began around 2010 and is almost completed. HRSST-1 buoys transmit their data through Iridium satellites, are geo-located by GPS, SST resolution is 0.01 K and position and SST measurements are synchronous. Simultaneously, another drifter type, called HRSST-2, characterized by a better calibrated, digital SST probe, has been developed and tested. HRSST-2 buoys are not all the same, some of them have additional improvements such as two SST probes, at 0.17 m and 0.48 m, or a careful insulation of the SST sensor from anything other than sea water (Poli et al., 2018). HRSST-2 buoys provide a more accurate SST and information on its representativeness, which is very useful when comparing satellite and buoy SST. With > 60 buoys deployed so far and 100 buoys expected in the next three years, HRSST-2 buoys are not sufficient by themselves for satellite SST operational validation, but they will significantly contribute to the validation of future instruments.

It is hoped that the current suite of ship-radiometers (Section 6) will continue to be deployed to provide SI-traceable assessments of the satellite-derived SST_{skin} accuracy and thereby contribute to the SST CDR. The fact that reliable, well-calibrated ship-board radiometers capable of providing SST_{skin} values are few in number, but slowly increasing, means that in the foreseeable future the data for assessing the accuracy of satellite-derived SST_{skin} will be comparatively sparse. Efforts are made to mount the radiometers on research ships for cruises in areas where conditions are particularly challenging for the cloud-screening and atmospheric correction algorithms (e.g. Minnett, 2010). Examples are at high latitudes where the atmospheric conditions are extreme in the global distributions of atmospheric temperature and humidity and where drifting buoys are few, or upwelling regions where air-sea temperature differences are generally different from the global distribution and from where the surface divergence tends to advect drifters. Additionally, atmospheric aerosols pose particular challenges to the algorithms (Díaz et al., 2001; Bogdanoff et al., 2015; Luo et al., 2019) and areas with frequent contamination by aerosols, such as Saharan dust outflows over the tropical and equatorial north-east and south-east Atlantic Ocean and Arabian Sea (Prospero and Carlson, 1972; Prospero, 1999; Prospero et al., 2002), or smoke from forest fires, such as off southwest Africa (Adebiyi et al., 2015) and around Indonesia require further investigation. There is an additional imperative to studying the effects of aerosols on the accuracies of infrared-derived SST_{skin} as the reduction in surface insolation resulting from aerosol scattering of sunlight reduces the SST and near-surface heat content (Delworth et al., 2005; Rajeev et al., 2008; Martínez Avellaneda et al., 2010). The activities of those operating ship-board radiometers are coordinated through the International SST Fiducial Reference Measurement (FRM) Radiometer Network (ISFRN; see http://www.shipborne-radiometer.org/), which issues guidelines on the specifications of ship-board radiometers, on best practices to mount instruments on ships, and the preferred format of data to facilitate easy data exchange (Ships4SST, 2019). It is in this format, referred to as L2R, that radiometer measurements should be submitted to the ESA Felyx system (Taberner et al., 2013) for generating match-ups with satellite radiometer measurements.

The recent, rapid development of reliable and stable unmanned aerial vehicles (UAVS, commonly referred to as “drones”) has introduced a new potential method for validating satellite-derived SST_{skin}. This has spurred the recent development of lightweight miniaturized self-calibrating radiometers with low power requirements, such as the Ball Experimental Sea Surface Temperature (BESST) Radiometer (Emery et al., 2014). Such radiometers offer a cost-effective method of validating satellite data in remote or rarely accessed areas. The BESST was installed on a Boeing ScanEagle UAV (https://en.wikipedia.org/wiki/Boeing_Insitu_ScanEagle) for the MIZOPEX study in the Arctic Marginal Ice Zone and the measurements have been analyzed to quantify SST_{skin} variability within individual MODIS pixels (Castro et al., 2017).

A further recent development that is contributing to the validation of satellite-derived SSTs is the growing use of robotic Autonomous Surface Vehicles, such as Saildrones (Voosen, 2018) and Wave Gliders (Manley and Willcox, 2010) as many are fitted with near-surface thermometers. In a recent deployment, from April 11, 2018–June 11, 2018, of a Saildrone off California and Mexico (Fig. 28), additional self-recording thermometers were installed on the hull and keel. The great advantage of such approaches is the possibility of post-cruise calibration of the sensors, and since they are not disposable platforms, more expensive and accurate sensors can be deployed than are usually used on drifting buoys. A comparison between subsurface temperatures measured by a SeaBird 56 temperature sensor on the Saildrone and L2 SST_{skin} derived from measurements from MODIS on Terra and Aqua, and from VIIRS on Suomi-NPP produced very promising results (Gentemann et al., 2019). The SSTs measured by the Saildrone CTD at 0.6 m depth throughout the deployment are shown in Fig. 28, along with differences between these temperatures and those in three widely-used GHRSST L4 SST products: MUR (Chin et al., 2017), OSTIA (Donlon et al., 2012b), and CMC (Brasnett, 1997; Brasnett and Surcel-Colan, 2016). Such co-located satellite-derived SSTs and Saildrone measurements provide estimates of mean differences, root mean square differences (RMSD) and correlations (Table 4). Overall, the differences were

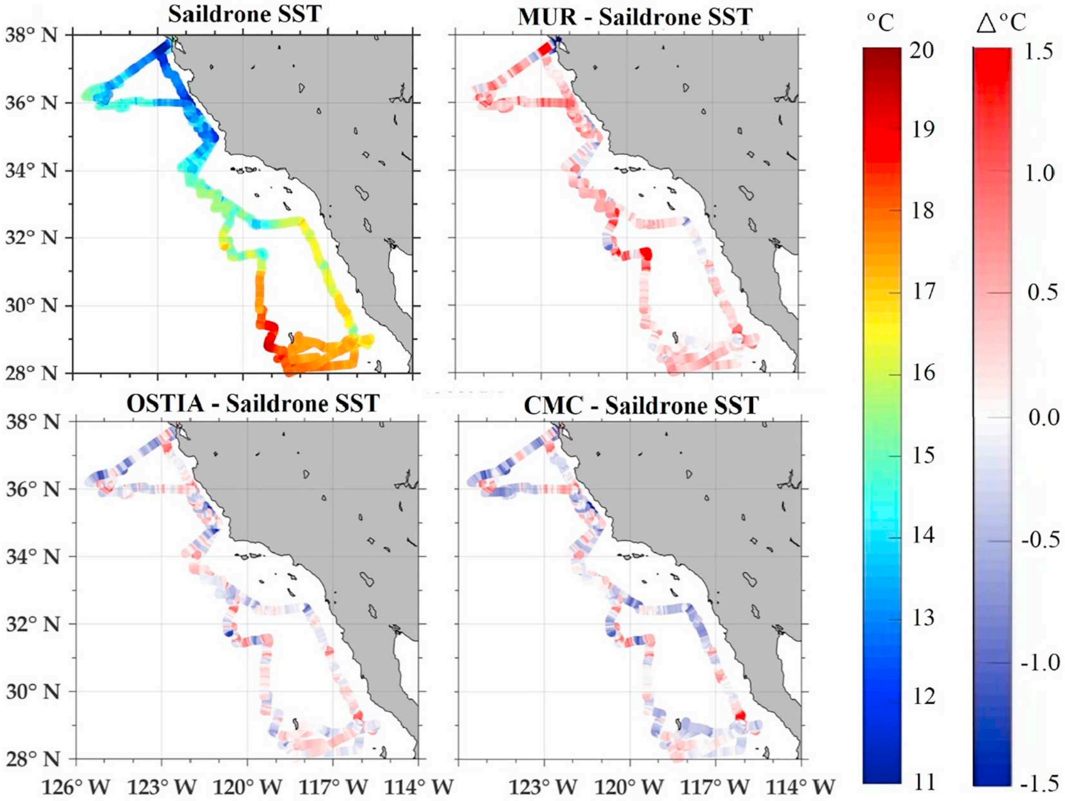

Fig. 28. The track of the Saildrone deployment from April 11, 2018–June 11, 2018 (top left), colored by the measured SST, as indicated by the temperature scale at right. Other panels show the differences between three L4 satellite-derived SST fields and the Saildrone measurements, colored according to the temperature difference scale at far right. After Vazquez-Cuervo et al. (2019).

Table 4
Statistics of differences between L4 satellite-derived SST fields and Saildrone measurements (after Vazquez-Cuervo et al., 2019).

Parameter	Bias (K)	RMSD (K)	Correlation (R)	Signal-to-noise ratio
CMC	−0.03	0.43	0.97	4.3
OSTIA	0.04	0.39	0.98	5.0
MUR	0.32	0.42	0.97	4.4

The signal to noise ratio indicates that the signal, as defined by each of the satellite derived data sets, is significantly larger than the noise, as defined by the differences between the satellite derived product and Saildrone.

close to zero, except for the MUR data which shows warm biases offshore. The high correlations of 0.96 and greater are consistent with the L4 fields reproducing a significant part of the coastal variability in this area.

In the summer of 2019, a fleet of six Saildrones was deployed in the Alaskan sector of the Arctic Ocean in a collaboration between NOAAs Pacific Marine Environmental Laboratory (PMEL) and a NASA-sponsored component of a US National Oceanographic Partnership Program (NOPP) project called the Multi-sensor Improved Sea-Surface Temperature (MISST). As with the 2018 Saildrone deployment, the two MISST Saildrones carry additional sub-surface thermometers, and also a pair of infrared radiometers, one viewing the sea-surface ahead of the Saildrone, and the other viewing the sky to provide data for the correction of reflected sky radiation to permit the retrieval of SST_{skin} from the Saildrone. It is anticipated that similar Saildrone deployments will be made in the summers of the next several years.

As with UAVs carrying radiometers, ASVs can make high-resolution measurements along their track.

15.3. Gridded SST analyses

For the gridded (L3 and L4) SST analyses in the near future, wider availability of 1-km and higher spatial resolution L2 input data sets such as VIIRS, SGLI, SLSTR, and METimage, and new-generation geostationary imagery could lead to new practices in data interpolation. The analysis interval would need to be shortened to a sub-daily level to avoid aliasing of the sub-10 km scale SST features which tend to evolve faster than their mesoscale counterparts.

The current NOAA 5 km Geostationary-Polar SST Analyses are generated on a daily basis for day and night, nighttime and diurnally corrected L4 products (Maturi et al., 2017). The availability of new, rapidly-sampled SST retrievals from geostationary satellites complemented by high latitude sampling from the new polar-orbiting sensors will support the development of a unified methodology to investigate the global characteristics of diurnal variability. This will support the optimal integration of diurnal variability in operational modelling systems, leading to improved L4 SST analyses products that resolve the daily cycle. The analysis methodology could build on that used in the current Geo-Polar Blended SST analysis (Maturi et al., 2017) but applied at a higher resolution. This will provide detection of high resolution spatial and temporal variability in coastal regions for the protection, restoration and management of coastal and ocean resources through ecosystem-based management, and contribute a better understanding of climate variability and change.

Another aspect related to the generation of L4 SST fields, in addition to diurnal temperature effects, is the drastic difference in L2 sample density between areas with and without sensor coverage and this will need to be dealt with, perhaps by determining inter-sample correlations, to avoid interpolation artifacts of numerical origin. The geolocation information in the L2 data sets would also need to be fully accounted for, without truncating its sub-grid portion, to represent SST features, such as front locations, with higher fidelity.

15.4. Ocean heat contents and severe storms

To improve our ability to resolve the sources and sinks of OHC in all ocean basins, at least three radar altimeter missions are needed for sea surface height anomalies (SSHA) for adequate daily sampling and to provide a realistic product for mesoscale oceanography needed for improved forecasting of severe storms. Given that only 17-years of OHC are currently available, such applied research efforts must continue over the next decade to build an evaluated data base, useful also for climate studies. While OHC has been principally used during tropical cyclone seasons, daily mapping also provides valuable data to address key science questions related to climate, such as the extent of warming (or cooling) in the warm pools of the Atlantic and Pacific Oceans, thermodynamic processes in the equatorial wave guides associated with eastward propagating Kelvin Waves, and linkages to the Madden-Julian Oscillation across the tropics.

In the coastal regime, connections to the nation-wide array of high frequency surface current radars and glider technologies will allow the derivation OHC closer to the coast. Thus, a more complete picture will emerge of OHC variability for use in basic and applied research as well as operations such as forecasting hurricane intensity change.

Anticipated benefits include new understanding of upper ocean thermodynamics, dynamics and air-sea processes relevant to tropical cyclone intensity forecasting, climate variability (e.g., SST anomalies and OHC anomalies over various time and spatial scales), fisheries, coral reef bleaching and air-sea fluxes. Over the longer term, the benefits will be for understanding climate variability including SST and OHC anomalies across the ocean basins.

15.5. Data distribution

In terms of data archive and distribution, the primary challenges for the future include allowing access and manipulation to larger amounts of data over longer periods of time, developing cloud technologies that allow users to implement their own processing algorithms (for example cloud masking/optimal interpolation), and visualization and extraction tools for near real time applications. Data quality standards should be measured by two issues: 1) Adherence to metadata standards that allow for interoperability, while maximizing implementation across a wide range of tools and services and 2) access to validation (matchup databases) that allow users to assess the quality of the data in their area of interest. Cloud technologies must be adopted cautiously, as it will require major paradigm shifts in both accessing data and information. An associated issue is ensuring that the user community is aware of new SST products, and of their strengths and weaknesses, so that new data sets that meet the users' requirements can be appropriately exploited. Some further evolving aspects of data centers have already been discussed in Section 14.

Acknowledgements

PJM acknowledges support from the NASA Physical Oceanography Program. The contributions by TMC and JV to this paper were carried out at the Jet Propulsion Laboratory (JPL), California Institute of Technology, under a contract with the National Aeronautics and Space Administration (NASA). MAS acknowledges support from ONR N00014-17-1-2545, NSF OPP-1751363, and NASA 80NSSC18K0837. IK is supported by the Copernicus & Mercator-Ocean through the Service Evolution Call 2 project DIVOST-COM.

The authors thank Dr. C. J. Merchant for providing a preprint of the paper (Merchant et al., 2019) to support the description (in Section 5.1.2) of the generation of the AVHRR time series of consistent SSTs.

Authors affiliated with NOAA state that their views, opinions, and findings contained in this paper are their own and should not be construed as an official NOAA or U.S. Government position, policy, or decision.

Apologies to those whose work was not included here, even though it may have made a significant contribution to the progress in the field, but were simply a casualty of limited space.

The authors acknowledge with thanks the suggestions and comments from three reviewers as these have resulted in an improved paper.

Declaration of competing interest

None.

References

Aagaard, K., Carmack, E.C., 1989. The role of sea ice and other fresh water in the Arctic circulation. J. Geophys. Res. 94, 14485–14498.

Adebiyi, A.A., Zuidema, P., Abel, S.J., 2015. The convolution of dynamics and moisture with the presence of shortwave absorbing aerosols over the Southeast Atlantic. J. Clim. 28, 1997–2024. https://doi.org/10.1175/jcli-d-14-00352.1.

Albuisson, M., Pontier, L., Wald, L., 1979. A comparison between sea surface temperature measurements from satellite NOAA 4 and from airborne radiometer ARIES. Oceanol. Acta 2, 1–4.

Allison, L.J., Kennedy, J.S., 1967. An evaluation of sea surface temperature as measured by the Nimbus I high resolution infrared radiometer. In: NASA Technical Note. NASA TN D-4078 NASA, Washington DC, USA 26 pp. Available at. https://ntrs.nasa.gov/archive/nasa/casi.ntrs.nasa.gov/19680000754.pdf.

Alvera-Azcárate, A., Barth, A., Rixen, M., Beckers, J.M., 2005. Reconstruction of incomplete oceanographic data sets using empirical orthogonal functions: application to the Adriatic Sea surface temperature. Ocean Model. 9, 325–346. https://doi.org/10.1016/j.ocemod.2004.08.001.

Alvera-Azcárate, A., Barth, A., Beckers, J.-M., Weisberg, R.H., 2007. Multivariate reconstruction of missing data in sea surface temperature, chlorophyll, and wind satellite fields. Journal of Geophysical Research: Oceans 112. https://doi.org/10.1029/2006JC003660.

Alvera-Azcárate, A., Barth, A., Sirjacobs, D., Beckers, J.M., 2009. Enhancing temporal correlations in EOF expansions for the reconstruction of missing data using DINEOF. Ocean Sci. 5, 475–485. https://doi.org/10.5194/os-5-475-2009.

Aminou, D.M.A., 2002. MSG's SEVIRI instrument. ESA Bull. 11, 15–17.

Anding, D., Kauth, R., 1970. Estimation of sea-surface temperature from space. Remote Sens. Environ. 1, 217–220.

Arribas, A., Glover, M., Maidens, A., Peterson, K., Gordon, M., MacLachlan, C., Graham, R., Fereday, D., Camp, J., Scaife, A.A., Xavier, P., McLean, P., Colman, A., Cusack, S., 2011. The GloSea4 ensemble prediction system for seasonal forecasting. Mon. Weather Rev. 139, 1891–1910. https://doi.org/10.1175/2010mwr3615.1.

Atkinson, C.P., Rayner, N.A., Kennedy, J.J., Good, S.A., 2014. An integrated database of ocean temperature and salinity observations. Journal of Geophysical Research: Oceans 119, 7139–7163. https://doi.org/10.1002/2014JC010053.

Aumann, H.H., Pagano, T.S., 2008. Using AIRS and IASI data to evaluate absolute radiometric accuracy and stability for climate applications. In: Proceedings of Optical Engineering + Applications, 7085. SPIE. https://doi.org/10.1117/12.795225. 5 pp.

Aumann, H.H., Chahine, M.T., Gautier, C., Goldberg, M.D., Kalnay, E., McMillin, L.M., Revercomb, H., Rosenkranz, P.W., Smith, W.L., Staelin, D.H., Strow, L.L., Susskind, J., 2003. AIRS/AMSU/HSB on the aqua mission: design, science objectives, data products, and processing systems. IEEE Transactions Geoscience and Remote Sensing 41, 253–264.

Banzon, V.F., Reynolds, R.W., Stokes, D., Xue, Y., 2014. A 1/4°-spatial-resolution daily sea surface temperature climatology based on a blended satellite and in situ analysis. J. Clim. 27, 8221–8228. https://doi.org/10.1175/JCLI-D-14-00293.1.

Barsi, J.A., Markham, B.L., Czapla-Myers, J.S., Helder, D.L., Hook, S.J., Schott, J.R., Haque, M.O., 2016. Landsat-7 ETM+ radiometric calibration status. In: Proceedings of SPIE Earth Observing Systems XXI. 9972 SPIE. https://doi.org/10.1117/12.2238625. 12 pp.

Barton, I.J., 1985. Transmission model and ground truth investigation of satellite derived sea surface temperatures. J. Climate and Appl. Met. 24, 508–516.

Barton, I.J., 1989. Digitization effects in AVHRR and MCSST data. Remote Sens. Environ. 29, 87–89. https://doi.org/10.1016/0034-4257(89)90081-3.

Barton, I.J., 1995. Satellite-derived sea surface temperatures: current status. J. Geophys. Res. 100, 8777–8790.

Barton, I.J., Minnett, P.J., Donlon, C.J., Hook, S.J., Jessup, A.T., Maillet, K.A., Nightingale, T.J., 2004. The Miami2001 infrared radiometer calibration and intercomparison: 2. Ship comparisons. J. Atmos. Ocean. Technol. 21, 268–283.

Bates, J.J., Smith, W.L., 1985. Sea surface temperature: observations from geostationary satellites. Journal of Geophysical Research: Oceans 90, 11609–11618. https://doi.org/10.1029/JC090iC06p11609.

Beggs, H., 2010. Use of TIR from space in operational systems. In: Barale, V., Gower, J.F.R., Alberotanza, L. (Eds.), Oceanography from Space Revisited. Springer Science +Business Media B.V, Dordrecht, 978-90-481-8681-5, pp. 249–271. https://doi.org/

10.1007/978-90-481-8681-5.

Behrenfeld, M.J., Falkowski, P.G., 1997. Photosynthetic rates derived from satellite-based chlorophyll concentration. Limnol. Oceanogr. 21, 1–20.

Behrenfeld, M.J., O'Malley, R.T., Siegel, D.A., McClain, C.R., Sarmiento, J.L., Feldman, G.C., Milligan, A.J., Falkowski, P.G., Letelier, R.M., Boss, E.S., 2006. Climate-driven trends in contemporary ocean productivity. Nature 444, 752. https://doi.org/10.1038/nature05317. https://www.nature.com/articles/nature05317#supplementary-information.

Bell, M.J., Forbes, R.M., Hines, A., 2000. Assessment of the FOAM global data assimilation system for real-time operational ocean forecasting. J. Mar. Syst. 25, 1–22.

Bell, M.J., Lefèbvre, M., Le Traon, P.-Y., Smith, N., Wilmer-Becker, K., 2009. GODAE: the global ocean data assimilation experiment. Oceanography 22, 14. https://doi.org/10.5670/oceanog.2009.62.

Bellenger, H., Duvel, J.-P., 2009. An analysis of tropical ocean diurnal warm layers. J. Clim. 22, 3629–3646. https://doi.org/10.1175/2008JCLI2598.1.

Bentamy, A., Katsaros, K., Queffeulou, P., 2011. Satellite air – sea fluxes. In: Tang, D. (Ed.), Remote Sensing of the Changing Oceans. Springer, Berlin Heidelberg, pp. 141–168. https://doi.org/10.1007/978-3-642-16541-2_8. 978-3-642-16540-5.

Bentamy, A., Piollé, J.F., Grouazel, A., Danielson, R., Gulev, S., Paul, F., Azelmat, H., Mathieu, P.P., von Schuckmann, K., Sathyendranath, S., Evers-King, H., Esau, I., Johannessen, J.A., Clayson, C.A., Pinker, R.T., Grodsky, S.A., Bourassa, M., Smith, S.R., Haines, K., Valdivieso, M., Merchant, C.J., Chapron, B., Anderson, A., Hollmann, R., Josey, S.A., 2017. Review and assessment of latent and sensible heat flux accuracy over the global oceans. Remote Sens. Environ. 201, 196–218. https://doi.org/10.1016/j.rse.2017.08.016.

Bermudo, F., Rousseau, S., Pequignot, E., Bernard, F., 2014. IASI-NG program: a new generation of infrared atmospheric sounding interferometer. In: Proceedings of 2014 IEEE Geoscience and Remote Sensing Symposium, https://doi.org/10.1109/IGARSS.2014.6946690. 1373–1376 pp.

Berry, D., Corlett, G., Embury, O., Merchant, C., 2018. Stability assessment of the (A)ATSR sea surface temperature climate dataset from the European Space Agency climate change initiative. Remote Sens. 10, 126.

Bertie, J.E., Lan, Z.D., 1996. Infrared intensities of liquids XX: the intensity of the OH stretching band revisited, and the best current values of the optical constants of H_2O (l) at 25 °C between 15,000 and $1\ \mathrm{cm}^{-1}$. App. Spectroscopy 50, 1047–1057.

Bessho, K., Date, K., Hayashi, M., Ikeda, A., Imai, T., Inoue, H., Kumagai, Y., Miyakawa, T., Murata, H., Ohno, T., Okuyama, A., Oyama, R., Sasaki, Y., Shimazu, Y., Shimoji, K., Sumida, Y., Suzuki, M., Taniguchi, H., Tsuchiyama, H., Uesawa, D., Yokota, H., Yoshida, R., 2016. An introduction to Himawari-8/9 - Japan's new-generation geostationary meteorological satellites. Journal of the Meteorological Society of Japan. Ser. II 94, 151–183. https://doi.org/10.2151/jmsj.2016-009.

Bhatt, R., Doelling, D.R., Scarino, B.R., Gopalan, A., Haney, C.O., Minnis, P., Bedka, K.M., 2016. A consistent AVHRR visible calibration record based on multiple methods applicable for the NOAA degrading orbits. Part I: methodology. J. Atmos. Ocean. Technol. 33, 2499–2515. https://doi.org/10.1175/jtech-d-16-0044.1.

Blumstein, D., Chalon, G., Carlier, T., Buil, C., Hebert, P., Maciaszek, T., Ponce, G., Phulpin, T., Tournier, B., Simeoni, D., Astruc, P., Clauss, A., Kayal, G., Jegou, R., 2004. IASI instrument: technical overview and measured performances. In: Strojnik, M. (Ed.), Proceedings of Proceedings of Infrared Spaceborne Remote Sensing XII, SPIE. vol. 5543. SPIE, Bellingham, WA, pp. 5543. 196–207. https://doi.org/10.1117/12.560907.

Bogdanoff, A.S., Westphal, D.L., Campbell, J.R., Cummings, J.A., Hyer, E.J., Reid, J.S., Clayson, C.A., 2015. Sensitivity of infrared sea surface temperature retrievals to the vertical distribution of airborne dust aerosol. Remote Sens. Environ. 159, 1–13. https://doi.org/10.1016/j.rse.2014.12.002.

Böhm, E., Marullo, S., Santoleri, R., 1991. AVHRR visible-IR detection of diurnal warming events in the western Mediterranean Sea. Int. J. Remote Sensing. 12, 695–701.

Bojinski, S., Verstraete, M., Peterson, T.C., Richter, C., Simmons, A., Zemp, M., 2014. The concept of essential climate variables in support of climate research, applications, and policy. Bull. Am. Meteorol. Soc. 95, 1431–1443. https://doi.org/10.1175/bams-d-13-00047.1.

Boussidi, B., Cornillon, P., Puggioni, G., Gentemann, C., 2019. Determining the AMSR-E SST footprint from co-located MODIS SSTs. Remote Sens. 11, 715.

Brando, V.E., Braga, F., Zaggia, L., Giardino, C., Bresciani, M., Matta, E., Bellafiore, D., Ferrarin, C., Maicu, F., Benetazzo, A., Bonaldo, D., Falcieri, F.M., Coluccelli, A., Russo, A., Carniel, S., 2015. High-resolution satellite turbidity and sea surface temperature observations of river plume interactions during a significant flood event. Ocean Sci. 11, 909–920. https://doi.org/10.5194/os-11-909-2015.

Brasnett, B., 1997. A global analysis of sea surface temperature for numerical weather prediction. J. Atmos. Ocean. Technol. 14, 925–937. https://doi.org/10.1175/1520-0426(1997)014<0925:Agaoss>2.0.Co;2.

Brasnett, B., 2008. The impact of satellite retrievals in a global sea-surface-temperature analysis. Q. J. R. Meteorol. Soc. 134, 1745–1760. https://doi.org/10.1002/qj.319.

Brasnett, B., Surcel-Colan, D., 2016. Assimilating retrievals of sea surface temperature from VIIRS and AMSR2. J. Atmos. Ocean. Technol. 33, 361–375. https://doi.org/10.1175/jtech-d-15-0093.1.

Broecker, W.S., 1991. The great ocean conveyor. Oceanography 42, 79–89.

Brown, O.B., Brown, J.W., Evans, R.H., 1985. Calibration of advanced very high resolution radiometer infrared observations. Journal of Geophysical Research: Oceans 90, 11667–11677. https://doi.org/10.1029/JC090iC06p11667.

Bulgin, C.E., Embury, O., Corlett, G., Merchant, C.J., 2016. Independent uncertainty estimates for coefficient based sea surface temperature retrieval from the along-track scanning radiometer instruments. Remote Sens. Environ. 178, 213–222. https://doi.org/10.1016/j.rse.2016.02.022.

Bulgin, C.E., Mittaz, J.P.D., Embury, O., Eastwood, S., Merchant, C.J., 2018. Bayesian cloud detection for 37 years of advanced very high resolution radiometer (AVHRR) global area coverage (GAC) data. Remote Sens. 10, 97.

Buongiorno Nardelli, B., Larnicol, G., D'Acunzo, E., Santoleri, R., Marullo, S., Le Traon, P.Y., 2003. Near real time SLA and SST products during 2-years of MFS pilot project: processing, analysis of the variability and of the coupled patterns. Ann. Geophys. 21, 103–121.

Buongiorno Nardelli, B., Marullo, S., Santoleri, R., 2005. Diurnal variations in AVHRR SST fields: a strategy for removing warm layer effects from daily images. Remote Sens. Environ. 47–56.

Buongiorno Nardelli, B., Tronconi, C., Pisano, A., Santoleri, R., 2013. High and ultra-high resolution processing of satellite sea surface temperature data over Southern European seas in the framework of MyOcean project. Remote Sens. Environ. 129, 1–16. https://doi.org/10.1016/j.rse.2012.10.012.

Buongiorno Nardelli, B., Pisano, A., Tronconi, C., Santoleri, R., 2015. Evaluation of different covariance models for the operational interpolation of high resolution satellite sea surface temperature data over the Mediterranean Sea. Remote Sens. Environ. 164, 334–343. https://doi.org/10.1016/j.rse.2015.04.025.

Buongiorno Nardelli, B., Droghei, R., Santoleri, R., 2016. Multi-dimensional interpolation of SMOS sea surface salinity with surface temperature and in situ salinity data. Remote Sens. Environ. 180, 392–402. https://doi.org/10.1016/j.rse.2015.12.052.

Carnes, M.R., Teague, W.J., Mitchell, J.L., 1994. Inference of subsurface thermohaline structure from fields measurable by satellite. J. Atmos. Ocean. Technol. 11, 551–566. https://doi.org/10.1175/1520-0426(1994)011<0551:Iostsf>2.0.Co;2.

Casey, K.S., Cornillon, P., 2001. Global and regional sea surface temperature trends. J. Clim. 14, 3801–3818.

Casey, K.S., Brandon, T.B., Cornillon, P., Evans, R., 2010. The past, present, and future of the AVHRR pathfinder SST program. In: Barale, V., Gower, J.F.R., Alberotanza, L. (Eds.), Oceanography from Space: Revisited. Springer Netherlands, Dordrecht, pp. 273–287. https://doi.org/10.1007/978-90-481-8681-5_16. 978-90-481-8681-5.

Castro, S.L., Wick, G.A., Emery, W.J., 2012. Evaluation of the relative performance of sea surface temperature measurements from different types of drifting and moored buoys using satellite-derived reference products. J. Geophys. Res. 117, C02029. https://doi.org/10.1029/2011jc007472.

Castro, S.L., Wick, G.A., Buck, J.J.H., 2014. Comparison of diurnal warming estimates from unpumped Argo data and SEVIRI satellite observations. Remote Sens. Environ. 140, 789–799. https://doi.org/10.1016/j.rse.2013.08.042.

Castro, S.L., Wick, G.A., Steele, M., 2016. Validation of satellite sea surface temperature analyses in the Beaufort Sea using UpTempO buoys. Remote Sens. Environ. 187, 458–475. https://doi.org/10.1016/j.rse.2016.10.035.

Castro, S., Emery, W., Wick, G., Tandy, W., 2017. Submesoscale sea surface temperature variability from UAV and satellite measurements. Remote Sens. 9, 1089. https://doi.org/10.3390/rs9111089.

Castro, S.L., Monzon, L.A., Wick, G.A., Lewis, R.D., Beylkin, G., 2018. Subpixel variability and quality assessment of satellite sea surface temperature data using a novel High Resolution Multistage Spectral Interpolation (HRMSI) technique. Remote Sens. Environ. 217, 292–308. https://doi.org/10.1016/j.rse.2018.08.019.

Cavalieri, D.J., Parkinson, C.L., 2012. Arctic sea ice variability and trends, 1979–2010. Cryosphere 6, 881–889. https://doi.org/10.5194/tc-6-881-2012.

Cazenave, A., Nerem, R.S., 2004. Present-day sea level change: observations and causes. Rev. Geophys. 42. https://doi.org/10.1029/2003RG000139.

Chassignet, E.P., Xu, X., 2017. Impact of horizontal resolution (1/12° to 1/50°) on Gulf Stream separation, penetration, and variability. J. Phys. Oceanogr. 47, 1999–2021. https://doi.org/10.1175/jpo-d-17-0031.1.

Cheng, X., Qi, Y., Zhou, W., 2008. Trends of sea level variations in the Indo-Pacific warm pool. Glob. Planet. Chang. 63, 57–66. https://doi.org/10.1016/j.gloplacha.2008.06.001.

Chin, T.M., Vazquez-Cuervo, J., Armstrong, E.M., 2014. On "gridless" interpolation and subgrid data density. J. Atmos. Ocean. Technol. 31, 1642–1652. https://doi.org/10.1175/jtech-d-13-00219.1.

Chin, T.M., Vazquez-Cuervo, J., Armstrong, E.M., 2017. A multi-scale high-resolution analysis of global sea surface temperature. Remote Sens. Environ. 200, 154–169. https://doi.org/10.1016/j.rse.2017.07.029.

Cho, Y.-M., Youn, H.-S., 2006. Characteristics of COMS meteorological imager. In: Proceedings of SPIE Remote Sensing. SPIE, pp. 6361 8 pp.

Clayson, C.A., Bogdanoff, A.S., 2013. The effect of Diurnal Sea surface temperature warming on climatological air–sea fluxes. J. Clim. 26, 2546–2556. https://doi.org/10.1175/JCLI-D-12-00062.1.

Clayson, C.A., Curry, J.A., 1996. Determination of surface turbulent fluxes for the tropical ocean-global atmosphere response experiment: comparison of satellite retrievals and in situ measurements. J. Geophys. Res. 101 (28), 515–528.

Clayson, C.A., Weitlich, D., 2007. Variability of tropical diurnal sea surface temperature. J. Clim. 20, 334–352. https://doi.org/10.1175/JCLI3999.1.

Clough, S.A., Shephard, M.W., Mlawer, E.J., Delamere, J.S., Iacono, M.J., Cady-Pereira, K., Boukabara, S., Brown, P.D., 2005. Atmospheric radiative transfer modeling: a summary of the AER codes. J. Quant. Spectrosc. Radiat. Transf. 91, 233–244. https://doi.org/10.1016/j.jqsrt.2004.05.058.

CMEMS, 2017. CMEMS requirements for the evolution of the Copernicus Satellite Component - Mercator Ocean and CMEMS partners. pp. 9. Available at. http://marine.copernicus.eu/wp-content/uploads/2019/01/CMEMS-requirements-satellites.pdf.

Coll, C., Caselles, V., Valor, E., 1993. Atmospheric correction and determination of sea surface temperature in midlatitudes from NOAA-AVHRR data. Atmos. Res. 30, 233–250. https://doi.org/10.1016/0169-8095(93)90026-K.

Corlett, G.K., Merchant, C.J., Minnett, P.J., Donlon, C.J., 2014. Assessment of long-term satellite derived sea surface temperature records. In: Zibordi, G., Donlon, C.J., Parr, A.C. (Eds.), Experimental Methods in the Physical Sciences, Vol 47, Optical Radiometry for Ocean Climate Measurements. Academic Press, pp. 639–677. https://

doi.org/10.1016/B978-0-12-417011-7.00021-0. 1079-4042.

Cornillon, P., Stramma, L., 1985. The distribution of diurnal sea surface warming events in the Western Sargasso Sea. J. Geophys. Res. 90 (11), 811–811, 815.

Cornillon, P., Pan, G., Schloesser, F., 2014. The submesoscale from VIIRS imagery-band (375 m) sea surface temperature fields. In: Presented at AGU Fall Meeting, San Francisco, CA, USA, . https://agu.confex.com/agu/fm14/webprogram/Paper4205.html.

Cotroneo, Y., Aulicino, G., Ruiz, S., Pascual, A., Budillon, G., Fusco, G., Tintoré, J., 2016. Glider and satellite high resolution monitoring of a mesoscale eddy in the Algerian basin: effects on the mixed layer depth and biochemistry. J. Mar. Syst. 162, 73–88. https://doi.org/10.1016/j.jmarsys.2015.12.004.

Cox, C., Munk, W., 1954. Statistics of the sea surface derived from sun glitter. J. Mar. Res. 13, 198–227.

Cracknell, A.P., 1997. The Advanced Very High Resolution Radiometer. CRC Press, Taylor and Francis, London, UK9780748402090.

Crépon, M., Wald, L., Monget, J.-M., 1982. Low-frequency waves in the Ligurian Sea during December 1977. Journal of Geophysical Research: Oceans 87, 595–600.

Crevoisier, C., Clerbaux, C., Guidard, V., Phulpin, T., Armante, R., Barret, B., Camy-Peyret, C., Chaboureau, J.P., Coheur, P.F., Crépeau, L., Dufour, G., Labonnote, L., Lavanant, L., Hadji-Lazaro, J., Herbin, H., Jacquinet-Husson, N., Payan, S., Péquignot, E., Pierangelo, C., Sellitto, P., Stubenrauch, C., 2014. Towards IASI-new generation (IASI-NG): impact of improved spectral resolution and radiometric noise on the retrieval of thermodynamic, chemistry and climate variables. Atmos. Meas. Tech. 7, 4367–4385. https://doi.org/10.5194/amt-7-4367-2014.

Dalu, G., Viola, A., Marullo, S., 1985. Sea surface temperature from AVHRR-2 data. Il Nuovo Cimento C 8, 793–804. https://doi.org/10.1007/bf02558011.

Danabasoglu, G., Large, W.G., Tribbia, J.J., Gent, P.R., Briegleb, B.P., McWilliams, J.C., 2006. Diurnal coupling in the tropical oceans of CCSM3. J. Clim. 19, 2347–2365.

Dash, P., Ignatov, A., Kihai, Y., Sapper, J., 2010. The SST quality monitor (SQUAM). J. Atmos. Ocean. Technol. 27, 1899–1917. https://doi.org/10.1175/2010jtecho756.1.

Dash, P., Ignatov, A., Martin, M., Donlon, C., Brasnett, B., Reynolds, R.W., Banzon, V., Beggs, H., Cayula, J.-F., Chao, Y., Grumbine, R., Maturi, E., Harris, A., Mittaz, J., Sapper, J., Chin, T.M., Vazquez-Cuervo, J., Armstrong, E.M., Gentemann, C., Cummings, J., Piollé, J.-F., Autret, E., Roberts-Jones, J., Ishizaki, S., Høyer, J.L., Poulter, D., 2012. Group for High Resolution Sea Surface Temperature (GHRSST) analysis fields inter-comparisons—part 2: near real time web-based level 4 SST quality monitor (L4-SQUAM). Deep-Sea Res. II Top. Stud. Oceanogr. 77–80, 31–43. https://doi.org/10.1016/j.dsr2.2012.04.002.

Dee, D.P., Uppala, S.M., Simmons, A.J., Berrisford, P., Poli, P., Kobayashi, S., Andrae, U., Balmaseda, M.A., Balsamo, G., Bauer, P., Bechtold, P., Beljaars, A.C.M., van de Berg, L., Bidlot, J., Bormann, N., Delsol, C., Dragani, R., Fuentes, M., Geer, A.J., Haimberger, L., Healy, S.B., Hersbach, H., Hólm, E.V., Isaksen, L., Kållberg, P., Köhler, M., Matricardi, M., McNally, A.P., Monge-Sanz, B.M., Morcrette, J.J., Park, B.K., Peubey, C., de Rosnay, P., Tavolato, C., Thépaut, J.N., Vitart, F., 2011. The ERA-interim reanalysis: configuration and performance of the data assimilation system. Q. J. R. Meteorol. Soc. 137, 553–597. https://doi.org/10.1002/qj.828.

Delworth, T.L., Ramaswamy, V., Stenchikov, G.L., 2005. The impact of aerosols on simulated ocean temperature and heat content in the 20th century. Geophys. Res. Lett. 32. https://doi.org/10.1029/2005gl024457.

Deschamps, P.Y., Frouin, R., 1984. Large diurnal heating of the sea surface observed by the HCMR experiment. J. Phys. Oceanogr. 14, 177–184.

Desnos, Y., Borgeaud, M., Doherty, M., Rast, M., Liebig, V., 2014. The European Space Agency's earth observation program. IEEE Geoscience and Remote Sensing Magazine 2, 37–46. https://doi.org/10.1109/MGRS.2014.2319270.

Díaz, J.P., Arbelo, M., Expósito, F.J., Podestá, G., Prospero, J.M., Evans, R., 2001. Relationship between errors in AVHRR-derived sea surface temperature and the TOMS Aerosol Index. Geophys. Res. Lett. 28, 1989–1992.

Dong, B., Dai, A., Vuille, M., Timm, O.E., 2018. Asymmetric modulation of ENSO teleconnections by the interdecadal Pacific oscillation. J. Clim. 31, 7337–7361. https://doi.org/10.1175/jcli-d-17-0663.1.

Donlon, C.J., Nightingale, T.J., 2000. The effect of atmospheric radiance errors in radiometric sea-surface skin temperature measurements. Appl. Opt. 39, 2387–2392.

Donlon, C.J., Minnett, P.J., Gentemann, C., Nightingale, T.J., Barton, I.J., Ward, B., Murray, J., 2002. Toward improved validation of satellite sea surface skin temperature measurements for climate research. J. Clim. 15, 353–369. https://doi.org/10.1175/1520-0442(2002)015<0353:TIVOSS>2.0.CO;2.

Donlon, C.J., Robinson, I., Casey, K.S., Vazquez-Cuervo, J., Armstrong, E., Arino, O., Gentemann, C., May, D., LeBorgne, P., Piollé, J., Barton, I., Beggs, H., Poulter, D.J.S., Merchant, C.J., Bingham, A., Heinz, S., Harris, A., Wick, G., Emery, B., Minnett, P., Evans, R., Llewellyn-Jones, D., Mutlow, C., Reynolds, R.W., Kawamura, H., Rayner, N., 2007. The global ocean data assimilation experiment high-Resolution sea surface temperature pilot project. Bull. Am. Meteorol. Soc. 88, 1197–1213.

Donlon, C., Robinson, I.S., Reynolds, M., Wimmer, W., Fisher, G., Edwards, R., Nightingale, T.J., 2008. An infrared sea surface temperature autonomous radiometer (ISAR) for deployment aboard volunteer observing ships (VOS). J. Atmos. Ocean. Technol. 25, 93–113.

Donlon, C.J., Casey, K.S., Robinson, I.S., Gentemann, C.L., Reynolds, R.W., Barton, I., Arino, O., Stark, J., Rayner, N., LeBorgne, P., Poulter, D., Vazquez-Cuervo, J., Armstrong, E., Beggs, H., Llewellyn-Jones, D., Minnett, P.J., Merchant, C.J., Evans, R., 2009. The GODAE high-resolution sea surface temperature pilot project. Oceanography 22, 34–45.

Donlon, C.J., Berruti, B., Buongiorno, A., Ferreira, M.H., Féménias, P., Frerick, J., Goryl, P., Klein, U., Laur, H., Mavrocordatos, C., Nieke, J., Rebhan, H., Seitz, B., Stroede, J., Sciarra, R., 2012a. The Global Monitoring for Environment and Security (GMES) Sentinel-3 mission. Remote Sens. Environ. 120, 37–57. https://doi.org/10.1016/j.rse.2011.07.024.

Donlon, C.J., Martin, M., Stark, J., Roberts-Jones, J., Fiedler, E., Wimmer, W., 2012b. The operational sea surface temperature and sea ice analysis (OSTIA) system. Remote Sens. Environ. 116, 140–158. https://doi.org/10.1016/j.rse.2010.10.017.

Donlon, C.J., Minnett, P.J., Jessup, A., Barton, I., Emery, W., Hook, S., Wimmer, W., Nightingale, T.J., Zappa, C., 2014. Ship-borne thermal infrared radiometer systems. In: Zibordi, G., Donlon, C.J., Parr, A.C. (Eds.), Experimental Methods in the Physical Sciences. Optical Radiometry for Ocean Climate Measurements 47. Academic Press, pp. 305–404. https://doi.org/10.1016/B978-0-12-417011-7.00011-8. 1079-4042.

Draper, D.W., Newell, D.A., Wentz, F.J., Krimchansky, S., Skofronick-Jackson, G.M., 2015. The global precipitation measurement (GPM) microwave imager (GMI): instrument overview and early on-orbit performance. IEEE Journal of Selected Topics in Applied Earth Observations and Remote Sensing 8, 3452–3462. https://doi.org/10.1109/JSTARS.2015.2403303.

Drinkwater, M.R.H., Le Traon, P.Y., Phalippou, L., Cotton, D., Johannesen, J., Ruffini, G., Bahurel, P., Bell, M., Chapron, B., Pinardi, N., Robinson, I., Santoleri, L., Stammer, D., 2005. Roadmap for a GMES operational oceanography mission. Proceedings of MERIS (A)ATSR Workshop, ESRIN, Frascati, Italy, H. Lacoste (ESA SP-597, 10 pp.).

Drinkwater, M.R., Kerr, Y., Font, J., Berger, M., 2009. The soil moisture and ocean salinity (SMOS) mission. Bulletin of the European Space Agency 137, 7–15.

Dubock, P., Spoto, F., Simpson, J., Spencer, D., Schutte, E., Sontag, H., 2001. The Envisat satellite and its integration. ESA Bull. 106, 26–45.

Dudhia, A., 1989. Noise characteristics of the AVHRR infrared channels. Int. J. Remote Sens. 10, 637–644. https://doi.org/10.1080/01431168908903904.

Durand, Y., Hallibert, P., Wilson, M., Lekouara, M., Grabarnik, S., Aminou, D., Blythe, P., Napierala, B., Canaud, J.-L., Pigouche, O., Ouaknine, J., Verez, B., 2015. The flexible combined imager onboard MTG: from design to calibration. In: Proceedings of SPIE Remote Sensing. 9639 SPIE. https://doi.org/10.1117/12.2196644. 14 pp.

Eastwood, S., Le Borgne, P., Péré, S., Poulter, D., 2011. Diurnal variability in sea surface temperature in the Arctic. Remote Sens. Environ. 115, 2594–2602. https://doi.org/10.1016/j.rse.2011.05.015.

Embury, O., Merchant, C.J., 2012. A reprocessing for climate of sea surface temperature from the along-track scanning radiometers: a new retrieval scheme. Remote Sens. Environ. 116, 47–61. https://doi.org/10.1016/j.rse.2010.11.020.

Embury, O., Merchant, C.J., Filipiak, M.J., 2012. A reprocessing for climate of sea surface temperature from the along-track scanning radiometers: basis in radiative transfer. Remote Sens. Environ. 116, 32–46. https://doi.org/10.1016/j.rse.2010.10.016.

Emery, W.J., Good, W.S., Tandy, W., Izaguirre, M.A., Minnett, P.J., 2014. A microbolometer airborne calibrated infrared radiometer: the Ball Experimental Sea Surface Temperature (BESST) radiometer. Geoscience and Remote Sensing, IEEE Transactions on 52, 7775–7781. https://doi.org/10.1109/TGRS.2014.2318683.

Entekhabi, D., Njoku, E.G., Neill, P.E.O., Kellogg, K.H., Crow, W.T., Edelstein, W.N., Entin, J.K., Goodman, S.D., Jackson, T.J., Johnson, J., Kimball, J., Piepmeier, J.R., Koster, R.D., Martin, N., McDonald, K.C., Moghaddam, M., Moran, S., Reichle, R., Shi, J.C., Spencer, M.W., Thurman, S.W., Tsang, L., Zyl, J.V., 2010. The Soil Moisture Active Passive (SMAP) mission. Proc. IEEE 98, 704–716. https://doi.org/10.1109/JPROC.2010.2043918.

Esaias, W.E., Abbott, M.R., Barton, I., Brown, O.B., Campbell, J.W., Carder, K.L., Clark, D.K., Evans, R.H., Hoge, F.E., Gordon, H.R., Balch, W.M., Letelier, R., Minnett, P.J., 1998. An overview of MODIS capabilities for ocean science observations. IEEE Trans. Geosci. Remote Sens. 36, 1250–1265. https://doi.org/10.1109/36.701076.

European Space Agency, 1999. Meteosat Second Generation: The Satellite Development. ESA BR-153, (55 pp.). ESA ESTEC, Noordwijk, The Netherlands Available at. http://www.esa.int/esapub/br/br153/br153.pdf.

Ezer, T., 2016. Revisiting the problem of the Gulf Stream separation: on the representation of topography in ocean models with different types of vertical grids. Ocean Model. 104, 15–27. https://doi.org/10.1016/j.ocemod.2016.05.008.

Fairall, C., Bradley, E., Godfrey, J., Wick, G., Edson, J., Young, G., 1996. Cool-skin and warm-layer effects on sea surface temperature. J. Geophys. Res. 101, 1295–1308.

Fallmann, J., Lewis, H., Castillo, J.M., Arnold, A., Ramsdale, S., 2017. Impact of sea surface temperature on stratiform cloud formation over the North Sea. Geophys. Res. Lett. 44, 4296–4303. https://doi.org/10.1002/2017GL073105.

Feng, Z., Ji, R., Ashjian, C., Campbell, R., Zhang, J., 2018. Biogeographic responses of the copepod Calanus glacialis to a changing Arctic marine environment. Glob. Chang. Biol. 24, e159–e170. https://doi.org/10.1111/gcb.13890.

Fiedler, E.K., McLaren, A., Banzon, V., Brasnett, B., Ishizaki, S., Kennedy, J., Rayner, N., Roberts-Jones, J., Corlett, G., Merchant, C.J., Donlon, C., 2019. Intercomparison of long-term sea surface temperature analyses using the GHRSST Multi-Product Ensemble (GMPE) system. Remote Sens. Environ. 222, 18–33. https://doi.org/10.1016/j.rse.2018.12.015.

Filipiak, M., Merchant, C., Kettle, H., Le Borgne, P., 2010. A statistical model for sea surface diurnal warming driven by numerical weather prediction fluxes and winds. Ocean Science Discussions 7.

Flament, P., Firing, M., Sawyer, M., Trefois, C., 1994. Amplitude and horizontal structure of a large diurnal sea surface warming event during the coastal ocean dynamics experiment. J. Phys. Oceanogr. 24, 124–139.

Fox, N.P., 2010. QA4EO Guide: A Guide to Establish a Quality Indicator on a Satellite Sensor Derived Data Product (Version 4.0). QA4EO-QAEO-GEN-DQK-001 (7 pp.) Available at. http://qa4eo.org/docs/QA4EO-QAEO-GEN-DQK-001_v4.0.pdf, Accessed date: 28 November 2018.

Franklin, B., Folger, T., Wright, E., Halley, E., Moll, H., 1768. Franklin-Folger Chart of the Gulf Stream. Mount and Page, London. https://www.loc.gov/item/88696412/ (Retrieved from the Library of Congress. Accessed November 1, 2017).

Freund, Y., & Mason, L. (1999). The alternating decision tree learning algorithm. Proceedings of Proceeding of the Sixteenth International Conference on Machine Learning, Bled, Slovenia, I. Bratko, & S. Dzeroski, 124–133 pp. Avialable at http://perun.pmf.uns.ac.rs/radovanovic/dmsem/cd/install/Weka/doc/classifiers-papers/

trees/ADTree/atrees.pdf.

Fuglister, F.C., 1955. Alternative analyses of current surveys. Deep Sea Research (1953) 2, 213–229. https://doi.org/10.1016/0146-6313(55)90026-5.

Fuglister, F.C., 1963. Gulf Stream '60. Prog. Oceanogr. 1, 265–373. https://doi.org/10.1016/0079-6611(63)90007-7.

Gaiser, P.W., St Germain, K.M., Twarog, E.M., Poe, G.A., Purdy, W., Richardson, D., Grossman, W., Jones, W.L., Spencer, D., Golba, G., Cleveland, J., Choy, L., Bevilacqua, R.M., Chang, P.S., 2004. The WindSat spaceborne polarimetric microwave radiometer: sensor description and early orbit performance. Geoscience and Remote Sensing, IEEE Transactions on 42, 2347–2361. https://doi.org/10.1109/TGRS.2004.836867.

Geer, A.J., Lonitz, K., Weston, P., Kazumori, M., Okamoto, K., Zhu, Y., Liu, E.H., Collard, A., Bell, W., Migliorini, S., Chambon, P., Fourrié, N., Kim, M.-J., Köpken-Watts, C., Schraff, C., 2018. All-sky satellite data assimilation at operational weather forecasting centres. Q. J. R. Meteorol. Soc. 144, 1191–1217. https://doi.org/10.1002/qj.3202.

Gentemann, C.L., 2014. Three way validation of MODIS and AMSR-E sea surface temperatures. Journal of Geophysical Research: Oceans 119, 2583–2598. https://doi.org/10.1002/2013JC009716.

Gentemann, C.L., Hilburn, K.A., 2015. In situ validation of sea surface temperatures from the GCOM-W1 AMSR2 RSS calibrated brightness temperatures. Journal of Geophysical Research: Oceans 120, 3567–3585. https://doi.org/10.1002/2014JC010574.

Gentemann, C.L., Minnett, P.J., 2008. Radiometric measurements of ocean surface thermal variability. J. Geophys. Res. 113 (C08017). https://doi.org/10.1029/2007JC004540.

Gentemann, C.L., Donlon, C.J., Stuart-Menteth, A., Wentz, F.J., 2003. Diurnal signals in satellite sea surface temperature measurements. Geophys. Res. Lett. 30, 1140–1143.

Gentemann, C.L., Minnett, P.J., LeBorgne, P., Merchant, C.J., 2008. Multi-satellite measurements of large diurnal warming events. Geophys. Res. Lett. 35, L22602. https://doi.org/10.1029/2008GL035730.

Gentemann, C.L., Minnett, P.J., Ward, B., 2009. Profiles of Ocean Surface Heating (POSH): a new model of upper ocean diurnal thermal variability. Journal of Geophysical Research 114, C07017. https://doi.org/10.1029/2008JC004825.

Gentemann, C.L., Meissner, T., Wentz, F.J., 2010. Accuracy of satellite sea surface temperatures at 7 and 11 GHz. IEEE Trans. Geosci. Remote Sens. 48, 1009–1018. https://doi.org/10.1109/TGRS.2009.2030322.

Gentemann, C., Mazzini, P., Pianca, P., Scott, J.P., Akella, S., Minnett, P.J., Cornillon, P., Cetinić, I., Chin, T.M., Gomez-Valdes, Vazquez, J., Tsontos, V., Jenkins, R., De Halleux, S., Peacock, D., Mattias, T., Cohen, N., 2019. Saildrone: adaptively sampling the marine environment. Bull. Amer. Met. Soc (In review).

Giering, R., Quast, R., Mittaz, J.P.D., Hunt, S.E., Harris, P.M., Woolliams, E.R., Merchant, C.J., 2019. A novel framework to harmonise satellite data series for climate applications. Remote Sens. 11, 1002.

Gladkova, I., Ignatov, A., Shahriar, F., Kihai, Y., Hillger, D., Petrenko, B., 2016. Improved VIIRS and MODIS SST imagery. Remote Sens. 8, 79.

Gloersen, P., Barath, F.T., 1977. A scanning multichannel microwave radiometer for Nimbus-G and SeaSat-A. IEEE Journal of Oceanic Engineering OE (2), 172–178.

Gloersen, P., Cavalieri, D.J., Chang, A.T.C., Wilheit, T.T., Campbell, W.J., Johannessen, O.M., Katsaros, K.B., Kunzi, K.F., Ross, D.B., Staelin, D., Windsor, E.P.L., Barath, F.T., Gudmandsen, P., Langham, E., Ramseier, R.O., 1984. A summary of results from the first Nimbus-7 SMMR observations. J. Geophys. Res. 89, 5335–5344.

Goldberg, M., Ohring, G., Butler, J., Cao, C., Datla, R., Doelling, D., Gärtner, V., Hewison, T., Iacovazzi, B., Kim, D., Kurino, T., Lafeuille, J., Minnis, P., Renaut, D., Schmetz, J., Tobin, D., Wang, L., Weng, F., Wu, X., Yu, F., Zhang, P., Zhu, T., 2011. The global space-based inter-calibration system. Bull. Am. Meteorol. Soc. 92, 467–475. https://doi.org/10.1175/2010bams2967.1.

González-Haro, C., Isern-Fontanet, J., 2014. Global ocean current reconstruction from altimetric and microwave SST measurements. Journal of Geophysical Research: Oceans 119, 3378–3391. https://doi.org/10.1002/2013JC009728.

Good, S.A., Corlett, G.K., Remedios, J.J., Noyes, E.J., Llewellyn-Jones, D.T., 2007. The global trend in sea surface temperature from 20 years of advanced very high resolution radiometer data. J. Clim. 20, 1255–1264. https://doi.org/10.1175/JCLI4049.1.

Griffiths, P.R., de Haseth, J.A., 1986. Fourier Transform Infrared Spectrometry. John Wiley & Sons, New York (0-471-09902-3).

Haine, T.W.N., Martin, T., 2017. The Arctic-Subarctic sea ice system is entering a seasonal regime: implications for future Arctic amplification. Sci. Rep. 7 (4618). https://doi.org/10.1038/s41598-017-04573-0.

Hall, M., Frank, E., Holmes, G., Pfahringer, B., Reutemann, P., Witten, I.H., 2009. The WEKA data mining software: an update. SIGKDD Explor. Newsl. 11, 10–18. https://doi.org/10.1145/1656274.1656278.

Hallsworth, S., 2005. Modelling the Diurnal-Variation of Sea Surface Temperature Using a One-Dimensional Ocean Turbulence Model (Ph.D. Thesis). School of GeoSciences. University of Edinburgh, Edinburgh, United Kingdom, pp. 187 pp.

Halpern, D., Reed, R.K., 1976. Heat budget of the upper ocean under light winds. J. Phys. Oceanogr. 6, 972–975. https://doi.org/10.1175/1520-0485(1976)006<0972:Hbotuo>2.0.Co;2.

Ham, Y.-G., Kug, J.-S., Kang, I.-S., Jin, F.-F., Timmermann, A., 2010. Impact of diurnal atmosphere–ocean coupling on tropical climate simulations using a coupled GCM. Clim. Dyn. 34, 905–917. https://doi.org/10.1007/s00382-009-0586-8.

Hamad, N., Millot, C., Taupier-Letage, I., 2005. A new hypothesis about the surface circulation in the eastern basin of the Mediterranean Sea. Prog. Oceanogr. 66, 287–298. https://doi.org/10.1016/j.pocean.2005.04.002.

Han, Y., van Delst, P., Liu, Q., Weng, F., Yan, B., Treadon, R., Derber, J., 2006. JCSDA Community Radiative Transfer Model (CRTM)—Version 1. NOAA Tech. Rep. NESDIS 122 NOAA, Camp Springs, MD. 40 pp. Available at. ftp.library.noaa.gov/noaa_documents.lib/NESDIS/TR_NESDIS/TR_NESDIS_122.pdf.

Han, W., Meehl, G.A., Rajagopalan, B., Fasullo, J.T., Hu, A., Lin, J., Large, W.G., Wang, J.-w., Quan, X.-W., Trenary, L.L., Wallcraft, A., Shinoda, T., Yeager, S., 2010. Patterns of Indian Ocean sea-level change in a warming climate. Nat. Geosci. 3, 546. https://doi.org/10.1038/ngeo901. https://www.nature.com/articles/ngeo901#supplementary-information.

Hanafin, J.A., Minnett, P.J., 2001. Cloud forcing of surface radiation in the north water polynya. Atmosphere-Ocean 39, 239–255.

Hanafin, J.A., Minnett, P.J., 2005. Infrared-emissivity measurements of a wind-roughened sea surface. Appl. Opt. 44, 398–411.

Harris Corporation, 2018. GOES-R Series Product Definition and Users' Guide (720 pp.) Available at. https://www.goes-r.gov/products/docs/PUG-L2+-vol5.pdf.

Hedley, J., Roelfsema, C., Chollett, I., Harborne, A., Heron, S., Weeks, S., Skirving, W., Strong, A., Eakin, C., Christensen, T., Ticzon, V., Bejarano, S., Mumby, P., 2016. Remote sensing of coral reefs for monitoring and management: a review. Remote Sens. 8, 118. https://doi.org/10.3390/rs8020118.

Hewison, T.J., König, M., 2008. Inter-calibration of Meteosat imagers and IASI. In: Proceedings of Proc. 2008 EUMETSAT Meteorological Satellite Conf, 52–59 pp. Available at. https://pdfs.semanticscholar.org/6b2c/24d2bb175030a6cbd103d329ab34ff542eb1.pdf.

Hewison, T.J., Wu, X., Yu, F., Tahara, Y., Hu, X., Kim, D., Koenig, M., 2013. GSICS inter-calibration of infrared channels of geostationary imagers using Metop/IASI. IEEE Trans. Geosci. Remote Sens. 51, 1160–1170.

Heygster, G., Kachi, M., Kelly, R., Liu, G., 2017. Guest editorial the global change observation mission—water: contributions to global water cycle science from the advanced microwave scanning radiometer–2. IEEE Journal of Selected Topics in Applied Earth Observations and Remote Sensing 10, 3835–3838. https://doi.org/10.1109/JSTARS.2017.2751758.

Hihara, T., Kubota, M., Okuro, A., 2015. Evaluation of sea surface temperature and wind speed observed by GCOM-W1/AMSR2 using in situ data and global products. Remote Sens. Environ. 164, 170–178. https://doi.org/10.1016/j.rse.2015.04.005.

Hilburn, K., 2009. Including temperature effects in the F15 RADCAL correction. In: Remote Sensing Systems Tech. Rep. 51209 (11 pp.) Available at. ftp://rain.atmos.colostate.edu/FCDR/doc/F15/Hilburn_09_Including_Temp_Effects_in_the_F15_RADCAL_Corr_RSS_TechRep051209.pdf.

Hong, X., Chang, S.W., Raman, S., Shay, L.K., Hodur, R., 2000. The interaction between hurricane opal (1995) and a warm core ring in the Gulf of Mexico. Mon. Weather Rev. 128, 1347–1365.

Hook, S.J., Vaughan, R.G., Tonooka, H., Schladow, S.G., 2007. Absolute radiometric in-flight validation of mid infrared and thermal infrared data from ASTER and MODIS on the Terra spacecraft using the Lake Tahoe, CA/NV, USA, automated validation site. Geoscience and Remote Sensing, IEEE Transactions on 45, 1798–1807. https://doi.org/10.1109/TGRS.2007.894564.

Høyer, J.L., Karagali, I., Dybkjær, G., Tonboe, R., 2012. Multi sensor validation and error characteristics of Arctic satellite sea surface temperature observations. Remote Sens. Environ. 121, 335–346. https://doi.org/10.1016/j.rse.2012.01.013.

Hulley, G.C., Hook, S.J., 2018. ECOsystem Spaceborne Thermal Radiometer Experiment on Space Station Level-2 Land Surface Temperature and Emissivity Algorithm Theoretical Basis Document (ATBD). JPL D-94643, (96 pp.). Jet Propulsion Laboratory, California Institute of Technology, Pasadena, CA, USA Available at. https://ecostress.jpl.nasa.gov/downloads/atbd/ECOSTRESS_L2_ATBD_LSTE_2018-03-08.pdf.

Hulley, G., Hook, S., Radocinski, R., Cawse-Nicholson, K., 2019. Stage-1 Validation of the ECOSTRESSS Level-2 Land Surface Temperature and Emissivity Products. (In preparation).

Hursen, K.A., Ross, R., 1996. GOES imager: overview and evolutionary development. In: Proceedings of SPIE's 1996 International Symposium on Optical Science, Engineering, and Instrumentation. 2812 SPIE. https://doi.org/10.1117/12.254064. 14 pp.

Imaoka, K., Kachi, M., Fujii, H., Murakami, H., Hori, M., Ono, A., Igarashi, T., Nakagawa, K., Oki, T., Honda, Y., Shimoda, H., 2010. Global change observation mission (GCOM) for monitoring carbon, water cycles, and climate change. Proc. IEEE 98, 717–734. https://doi.org/10.1109/JPROC.2009.2036869.

Jha, B., Hu, Z.-Z., Kumar, A., 2014. SST and ENSO variability and change simulated in historical experiments of CMIP5 models. Clim. Dyn. 42, 2113–2124. https://doi.org/10.1007/s00382-013-1803-z.

Jiang, G., Yan, H., Ma, L., 2009. Intercalibration of SVISSR/FY-2C infrared channels against MODIS/terra and AIRS/aqua channels. IEEE Trans. Geosci. Remote Sens. 47, 1548–1558. https://doi.org/10.1109/TGRS.2008.2005200.

Kachi, M., Maeda, T., Tsutsui, H., Ono, N., Kasahara, M., Mokuno, M., 2017. Five years observations of global water cycle by GCOM-W/AMSR2. In: Proceedings of 2017 IEEE International Geoscience and Remote Sensing Symposium (IGARSS), https://doi.org/10.1109/IGARSS.2017.8128285. 5641–5643 pp.

Kaiser, J.A.C., 1978. Heat balance of the upper ocean under light winds. J. Phys. Oceanogr. 8, 1–12. https://doi.org/10.1175/1520-0485(1978)008<0001:Hbotuo>2.0.Co;2.

Kannenberg, R., Palluconi, F., 1998. Joint Rosenstiel School of Marine and Atmospheric Science (RSMAS) Committee on Earth Observation Satellites (CEOS) validation workshop. The Earth Observer 10, 38–42.

Kantha, L.H., Clayson, C.A., 1994. An improved mixed layer model for geophysical applications. Journal of Geophysical Research: Oceans 99, 25235–25266. https://doi.org/10.1029/94JC02257.

Kaplan, A., Kushnir, Y., Cane, M.A., Blumenthal, M.B., 1997. Reduced space optimal analysis for historical data sets: 136 years of Atlantic sea surface temperatures. Journal of Geophysical Research: Oceans 102, 27835–27860. https://doi.org/10.1029/97jc01734.

Kaplan, A., Cane, M.A., Kushnir, Y., 2003. Reduced space approach to the optimal analysis interpolation of historical marine observations: accomplishments, difficulties, and prospects. In: Advances in the Applications of Marine Climatology: The Dynamic Part of the WMO Guide to the Applications of Marine Climatology. World Meteorological Organization, Geneva, Switzerland 199–216 pp.

Karagali, I., Høyer, J.L., 2013. Observations and modeling of the diurnal SST cycle in the North and Baltic seas. Journal of Geophysical Research: Oceans 118, 4488–4503. https://doi.org/10.1002/jgrc.20320.

Karagali, I., Høyer, J.L., 2014. Characterisation and quantification of regional diurnal SST cycles from SEVIRI. Ocean Sci. 10, 745–758. https://doi.org/10.5194/os-10-745-2014.

Karagali, I., Høyer, J., Hasager, C., 2012. SST diurnal variability in the North Sea and the Baltic Sea. Remote Sens. Environ. 121, 159–170. https://doi.org/10.1016/j.rse.2012.01.016.

Karagali, I., Høyer, J.L., Donlon, C.J., 2017. Using a 1-D model to reproduce the diurnal variability of SST. Journal of Geophysical Research: Oceans 122, 2945–2959. https://doi.org/10.1002/2016JC012542.

Karlsson, K.-G., Håkansson, N., Mittaz, J.P.D., Hanschmann, T., Devasthale, A., 2017. Impact of AVHRR channel 3b noise on climate data records: filtering method applied to the CM SAF CLARA-A2 data record. Remote Sens. 9, 568.

Kawai, H., 1998. A brief history of recognition of the Kuroshio. Prog. Oceanogr. 41, 505–578. https://doi.org/10.1016/S0079-6611(98)00024-X.

Kawai, Y., Kawamura, H., 2002. Evaluation of the diurnal warming of sea surface temperatures using satellite-derived marine meteorological data. J. Oceanogr. 58, 805–814.

Kawanishi, T., Sezai, T., Ito, Y., Imaoka, K., Takeshima, T., Ishido, Y., Shibata, A., Miura, M., Inahata, H., Spencer, R.W., 2003. The advanced microwave scanning radiometer for the earth observing system (AMSR-E), NASDA's contribution to the EOS for global energy and water cycle studies. Geoscience and Remote Sensing, IEEE Transactions on 41, 184–194. https://doi.org/10.1109/TGRS.2002.808331.

Kilic, L., Prigent, C., Aires, F., Boutin, J., Heygster, G., Tonboe, R.T., Roquet, H., Jimenez, C., Donlon, C., 2018. Expected performances of the Copernicus imaging microwave radiometer (CIMR) for an all-weather and high spatial resolution estimation of ocean and sea ice parameters. Journal of Geophysical Research: Oceans 123, 7564–7580. https://doi.org/10.1029/2018JC014408.

Kilpatrick, K.A., Podestá, G.P., Evans, R.H., 2001. Overview of the NOAA/NASA pathfinder algorithm for sea surface temperature and associated matchup database. J. Geophys. Res. 106, 9179–9198.

Kilpatrick, K.A., Podestá, G., Walsh, S., Williams, E., Halliwell, V., Szczodrak, M., Brown, O.B., Minnett, P.J., Evans, R., 2015. A decade of sea surface temperature from MODIS. Remote Sens. Environ. 165, 27–41. https://doi.org/10.1016/j.rse.2015.04.023.

Kilpatrick, K.A., Podestá, G., Williams, E., Walsh, S., Minnett, P.J., 2019. Alternating decision trees for cloud masking in MODIS and VIIRS NASA sea surface temperature products. J. Atmos. Ocean. Technol. 36, 387–407. https://doi.org/10.1175/jtech-d-18-0103.1.

Klaes, K.D., Holmlund, K., 2014. EUMETSAT programmes and plans. In: Proc. SPIE 9218, Earth Observing Systems XIX, 92181D (September 25, 2014), https://doi.org/10.1117/12.2061020.

Klaes, D.K., Cohen, M., Buhler, Y., Schluessel, P., Munro, R., Luntama, J.-P., Engeln, A.v., Clerigh, E., Bonekamp, H., Ackermann, J., Schmetz, J., 2007. An introduction to the EUMETSAT polar system. Bull. Am. Meteorol. Soc. 88, 1085–1096.

Knudsen, P., Andersen, O.B., Knudsen, T., 1996. ATSR sea surface temperature data in a global analysis with TOPEX/POSEIDON altimetry. Geophys. Res. Lett. 23, 821–824. https://doi.org/10.1029/96GL00618.

Koner, P.K., Drummond, J.R., 2008. Atmospheric trace gases profile retrievals using the nonlinear regularized total least squares method. J. Quant. Spectrosc. Radiat. Transf. 109, 2045–2059. https://doi.org/10.1016/j.jqsrt.2008.02.014.

Koner, P., Harris, A., 2016. Improved quality of MODIS sea surface temperature retrieval and data coverage using physical deterministic methods. Remote Sens. 8, 454.

Koner, P.K., Harris, A., Maturi, E., 2015. A physical deterministic inverse method for operational satellite remote sensing: an application for sea surface temperature retrievals. IEEE Trans. Geosci. Remote Sens. 53, 5872–5888. https://doi.org/10.1109/TGRS.2015.2424219.

Kummerow, C., Barnes, W., Kozu, T., Shiue, J., Simpson, J., 1998. The Tropical Rainfall Measuring Mission (TRMM) sensor package. J. Atmos. Ocean. Technol. 15, 809–817.

Kurihara, Y., Murakami, H., Kachi, M., 2016. Sea surface temperature from the new Japanese geostationary meteorological Himawari-8 satellite. Geophys. Res. Lett. 43, 1234–1240. https://doi.org/10.1002/2015GL067159.

Lacombe, H., Gascard, J., Gonella, J., Bethoux, J., 1981. Response of the Mediterranean to the water and energy fluxes across its surface, on seasonal and interannual scales. Oceanol. Acta 4, 247–255.

Lacouture, J., 1995. The Gulf Stream charts of Benjamin Franklin and Timothy Folger. Historic Nantucket 44, 82–86.

Lagerloef, G., Colomb, F.R., Vine, D.L., Wentz, F., Yueh, S., Ruf, C., Lilly, J., Gunn, J., Chao, Y., deCharon, A., Feldman, G., Swift, C., 2008. The aquarius/SAC-D mission: designed to meet the salinity remote-sensing challenge. Oceanography 21, 68–81. https://doi.org/10.5670/oceanog.2008.68.

Lautenbacher, C.C., 2006. The global earth observation system of systems: science serving society. Space Policy 22, 8–11. https://doi.org/10.1016/j.spacepol.2005.12.004.

LaViolette, P.E., Chabot, P.L., 1968. Nimbus II satellite sea surface temperatures versus historical data in a selected region: a comparative study. Deep-Sea Res. Oceanogr. Abstr. 15, 617–622. https://doi.org/10.1016/0011-7471(68)90068-5.

Le Borgne, P., Legendre, G., Péré, S., 2012a. Comparison of MSG/SEVIRI and drifting buoy derived diurnal warming estimates. Remote Sens. Environ. 124, 622–626. https://doi.org/10.1016/j.rse.2012.06.015.

Le Borgne, P., Marsouin, A., Orain, F., Roquet, H., 2012b. Operational sea surface temperature bias adjustment using AATSR data. Remote Sens. Environ. 116, 93–106. https://doi.org/10.1016/j.rse.2010.02.023.

Le Traon, P.Y., Antoine, D., Bentamy, A., Bonekamp, H., Breivik, L.A., Chapron, B., Corlett, G., Dibarboure, G., DiGiacomo, P., Donlon, C., Faugère, Y., Font, J., Girard-Ardhuin, F., Gohin, F., Johannessen, J.A., Kamachi, M., Lagerloef, G., Lambin, J., Larnicol, G., Le Borgne, P., Leuliette, E., Lindstrom, E., Martin, M.J., Maturi, E., Miller, L., Mingsen, L., Morrow, R., Reul, N., Rio, M.H., Roquet, H., Santoleri, R., Wilkin, J., 2015. Use of satellite observations for operational oceanography: recent achievements and future prospects. Journal of Operational Oceanography 8, s12–s27. https://doi.org/10.1080/1755876X.2015.1022050.

Le Traon, P.Y., Reppucci, A., Alvarez Fanjul, E., Aouf, L., Behrens, A., Belmonte, M., Bentamy, A., Bertino, L., Brando, V.E., Kreiner, M.B., Benkiran, M., Carval, T., Ciliberti, S.A., Claustre, H., Clementi, E., Coppini, G., Cossarini, G., De Alfonso Alonso-Muñoyerro, M., Delamarche, A., Dibarboure, G., Dinessen, F., Drevillon, M., Drillet, Y., Faugere, Y., Fernández, V., Fleming, A., Garcia-Hermosa, M.I., Sotillo, M.G., Garric, G., Gasparin, F., Giordan, C., Gehlen, M., Gregoire, M.L., Guinehut, S., Hamon, M., Harris, C., Hernandez, F., Hinkler, J.B., Hoyer, J., Karvonen, J., Kay, S., King, R., Lavergne, T., Lemieux-Dudon, B., Lima, L., Mao, C., Martin, M.J., Masina, S., Melet, A., Buongiorno Nardelli, B., Nolan, G., Pascual, A., Pistoia, J., Palazov, A., Piolle, J.F., Pujol, M.I., Pequignet, A.C., Peneva, E., Pérez Gómez, B., Petit de la Villeon, L., Pinardi, N., Pisano, A., Pouliquen, S., Reid, R., Remy, E., Santoleri, R., Siddorn, J., She, J., Staneva, J., Stoffelen, A., Tonani, M., Vandenbulcke, L., von Schuckmann, K., Volpe, G., Wettre, C., Zacharioudaki, A., 2019. From observation to information and users: the Copernicus marine service perspective. Front. Mar. Sci. 6. https://doi.org/10.3389/fmars.2019.00234.

Lean, K., Saunders, R.W., 2013. Validation of the ATSR Reprocessing for Climate (ARC) dataset using data from drifting buoys and a three-way error analysis. J. Clim. 26, 4758–4772. https://doi.org/10.1175/JCLI-D-12-00206.1.

L'Ecuyer, T.S., Jiang, J.H., 2010. Touring the atmosphere aboard the A-Train. Phys. Today 63, 36–41.

Legeckis, R., 1975. Application of synchronous meteorological satellite data to the study of time dependent sea surface temperature changes along the boundary of the Gulf Stream. Geophys. Res. Lett. 2, 435–438. https://doi.org/10.1029/GL002i010p00435.

Legeckis, R., 1977. Long waves in the eastern equatorial Pacific Ocean: a view from a geostationary satellite. Science 197, 1179–1181. https://doi.org/10.1126/science.197.4309.1179.

Legeckis, R., 1978. A survey of worldwide sea surface temperature fronts detected by environmental satellites. Journal of Geophysical Research: Oceans 83, 4501–4522. https://doi.org/10.1029/JC083iC09p04501.

Legeckis, R.V., 1979. Satellite observations of the influence of bottom topography on the seaward deflection of the Gulf Stream off Charleston, South Carolina. J. Phys. Oceanogr. 9, 483–497. https://doi.org/10.1175/1520-0485(1979)009<0483:sootio>2.0.co;2.

Legeckis, R., Gordon, A.L., 1982. Satellite observations of the Brazil and Falkland currents—1975 1976 and 1978. Deep Sea Research Part A. Oceanographic Research Papers 29, 375–401. https://doi.org/10.1016/0198-0149(82)90101-7.

Lei, G., Cong, M., 2013. Sea surface temperature from HY-1B COCTS. In: Proceedings of Geoscience and Remote Sensing Symposium (IGARSS), 2013 IEEE International, https://doi.org/10.1109/IGARSS.2013.6721241. 652–655.

Lellouche, J.M., Greiner, E., Le Galloudec, O., Garric, G., Regnier, C., Drevillon, M., Benkiran, M., Testut, C.E., Bourdalle-Badie, R., Gasparin, F., Hernandez, O., Levier, B., Drillet, Y., Remy, E., Le Traon, P.Y., 2018. Recent updates to the Copernicus marine service global ocean monitoring and forecasting real-time 1/12° high-resolution system. Ocean Sci. 14, 1093–1126. https://doi.org/10.5194/os-14-1093-2018.

Li, Y., He, R., 2014. Spatial and temporal variability of SST and ocean color in the Gulf of Maine based on cloud-free SST and chlorophyll reconstructions in 2003–2012. Remote Sens. Environ. 144, 98–108. https://doi.org/10.1016/j.rse.2014.01.019.

Li, X., Derber, J., Moorthi, S., Collard, C.A., 2019. Sea surface temperature analysis within the NCEP GFS. In: National Centers for Environmental Prediction Office Notes. 496 NCEP To be available at. https://www.lib.ncep.noaa.gov/ncepofficenotes/.

Liu, Y., Minnett, P.J., 2015. Evidence linking satellite-derived sea-surface temperature signals to changes in the Atlantic meridional overturning circulation. Remote Sens. Environ. 169, 150–162. https://doi.org/10.1016/j.rse.2015.08.014.

Liu, Y., Minnett, P.J., 2016. Sampling errors in satellite-derived infrared sea-surface temperatures. Part I: global and regional MODIS fields. Remote Sens. Environ. 177, 48–64. https://doi.org/10.1016/j.rse.2016.02.026.

Liu, Y., Chin, T.M., Minnett, P.J., 2017. Sampling errors in satellite-derived infrared sea-surface temperatures. Part II: sensitivity and parameterization. Remote Sens. Environ. 198, 297–309. https://doi.org/10.1016/j.rse.2017.06.011.

Llewellyn-Jones, D.T., Minnett, P.J., Saunders, R.W., Zavody, A.M., 1984. Satellite multichannel infrared measurements of sea surface temperature of the N.E. Atlantic Ocean using AVHRR/2. Q. J. R. Meteorol. Soc. 110, 613–631. https://doi.org/10.1002/qj.49711046504.

Louet, J., Bruzzi, S., 1999. ENVISAT mission and system. In: Proceedings of IEEE 1999 International Geoscience and Remote Sensing Symposium. IGARSS'99 (Cat. No.99CH36293). 3https://doi.org/10.1109/IGARSS.1999.772059.

Luo, J., Ault, J.S., Shay, L.K., Hoolihan, J.P., Prince, E.D., Brown, C.A., Rooker, J.R., 2015. Ocean heat content reveals secrets of fish migrations. PLoS One 10, e0141101. https://doi.org/10.1371/journal.pone.0141101.

Luo, B., Minnett, P.J., Gentemann, C., Szczodrak, G., 2019. Improving satellite retrieved night-time infrared sea surface temperatures in aerosol contaminated regions. Remote Sens. Environ. 223, 8–20. https://doi.org/10.1016/j.rse.2019.01.009.

Malkus, J.S., Riehl, H., 1960. On the dynamics and energy transformations in steady-state hurricanes. Tellus 12, 1–20. https://doi.org/10.3402/tellusa.v12i1.9351.

Manley, J., Willcox, S., 2010. The wave glider: a persistent platform for ocean science. In: Proceedings of OCEANS'10 IEEE SYDNEY, https://doi.org/10.1109/OCEANSSYD.2010.5603614. 5 pp.

Markham, B.L., Boncyk, W.C., Helder, D.L., Barker, J.L., 1997. Landsat-7 enhanced thematic mapper plus radiometric calibration. Can. J. Remote. Sens. 23, 318–332. https://doi.org/10.1080/07038992.1997.10855218.

Marsouin, A., Le Borgne, P., Legendre, G., Péré, S., Roquet, H., 2015. Six years of OSI-SAF METOP-A AVHRR sea surface temperature. Remote Sens. Environ. 159, 288–306. https://doi.org/10.1016/j.rse.2014.12.018.

Martin, S., 2014. An Introduction to Ocean Remote Sensing, 2 ed. Cambridge University Press, Cambridge. https://doi.org/10.1017/CBO9781139094368. 9781107019386.

Martin, M., Dash, P., Ignatov, A., Banzon, V., Beggs, H., Brasnett, B., Cayula, J.-F., Cummings, J., Donlon, C., Gentemann, C., Grumbine, R., Ishizaki, S., Maturi, E., Reynolds, R.W., Roberts-Jones, J., 2012. Group for high resolution sea surface temperature (GHRSST) analysis fields inter-comparisons. Part 1: a GHRSST multi-product ensemble (GMPE). Deep-Sea Res. II Top. Stud. Oceanogr. 77–80, 21–30. https://doi.org/10.1016/j.dsr2.2012.04.013.

Martínez Avellaneda, N., Serra, N., Minnett, P., Stammer, D., 2010. Response of the eastern subtropical Atlantic SST to Saharan dust: a modeling and observational study. Journal of Geophysical Research: Oceans (1978–2012) 115.

Marullo, S., Salusti, E., Viola, A., 1985. Observations of a small-scale baroclinic eddy in the Ligurian Sea. Deep Sea Research Part A. Oceanographic Research Papers 32, 215–222. https://doi.org/10.1016/0198-0149(85)90029-9.

Marullo, S., Santoleri, R., Malanotte-Rizzoli, P., Bergamasco, A., 1999a. The sea surface temperature field in the Eastern Mediterranean from advanced very high resolution radiometer (AVHRR) data: part I. Seasonal variability. J. Mar. Syst. 20, 63–81. https://doi.org/10.1016/S0924-7963(98)00071-2.

Marullo, S., Santoleri, R., Malanotte-Rizzoli, P., Bergamasco, A., 1999b. The sea surface temperature field in the Eastern Mediterranean from advanced very high resolution radiometer (AVHRR) data: part II. Interannual variability. J. Mar. Syst. 20, 83–112. https://doi.org/10.1016/S0924-7963(98)00072-4.

Marullo, S., Buongiorno Nardelli, B., Guarracino, M., Santoleri, R., 2007. Observing the Mediterranean Sea from space: 21 years of pathfinder-AVHRR sea surface temperatures (1985 to 2005): re-analysis and validation. Ocean Sci. 3, 299–310. https://doi.org/10.5194/os-3-299-2007.

Marullo, S., Santoleri, R., Banzon, V., Evans, R.H., Guarracino, M., 2010. A diurnal-cycle resolving sea surface temperature product for the tropical Atlantic. Journal of Geophysical Research: Oceans 115, C05011. https://doi.org/10.1029/2009JC005466.

Marullo, S., Minnett, P., Santoleri, R., Tonani, M., Pinardi, N., 2014a. SST diurnal cycle and heat budget estimates over the Mediterranean Sea. In: Proceedings of Earth Observation for Ocean-Atmosphere Interactions Science 2014, Responding to the New Scientific Challenges of SOLAS. 28th–31st October 2014, European Space Research Institute, Frascati, Italy. European Space Agency 8 pp.

Marullo, S., Santoleri, R., Ciani, D., Le Borgne, P., Péré, S., Pinardi, N., Tonani, M., Nardone, G., 2014b. Combining model and geostationary satellite data to reconstruct hourly SST field over the Mediterranean Sea. Remote Sens. Environ. 146, 11–23. https://doi.org/10.1016/j.rse.2013.11.001.

Marullo, S., Minnett, P.J., Santoleri, R., Tonani, M., 2016. The diurnal cycle of sea-surface temperature and estimation of the heat budget of the Mediterranean Sea. Journal of Geophysical Research: Oceans 121. https://doi.org/10.1002/2016jc012192.

Matsuoka, Y., Kawamura, H., Sakaida, F., Hosoda, K., 2011. Retrieval of high-resolution sea surface temperature data for Sendai Bay, Japan, using the Advanced Spaceborne Thermal Emission and Reflection Radiometer (ASTER). Remote Sens. Environ. 115, 205–213. https://doi.org/10.1016/j.rse.2010.08.018.

Maturi, E., Harris, A., Merchant, C., Mittaz, J., Potash, B., Meng, W., Sapper, J., 2008. NOAA's sea surface temperature products from operational geostationary satellites. Bull. Am. Meteorol. Soc. 89, 1877–1888.

Maturi, E., Harris, A., Mittaz, J., Sapper, J., Wick, G., Zhu, X., Dash, P., Koner, P., 2017. A new high-resolution sea surface temperature blended analysis. Bull. Am. Meteorol. Soc. 98, 1015–1026. https://doi.org/10.1175/bams-d-15-00002.1.

Mauri, E., Poulain, P.-M., 2001. Northern Adriatic Sea surface circulation and temperature/pigment fields in September and October 1997. J. Mar. Syst. 29, 51–67. https://doi.org/10.1016/S0924-7963(01)00009-4.

McClain, E.P., 1980. Passive radiometry of the ocean from space—an overview. Bound.-Layer Meteorol. 18, 7–24. https://doi.org/10.1007/bf00117908.

McClain, E.P., Pichel, W.G., Walton, C.C., 1985. Comparative performance of AVHRR-based multichannel sea surface temperatures. J. Geophys. Res. 90, 11587–11601.

McGranahan, G., Balk, D., Anderson, B., 2007. The rising tide: assessing the risks of climate change and human settlements in low elevation coastal zones. Environ. Urban. 19, 17–37. https://doi.org/10.1177/0956247807076960.

McMillin, L., 1975. Estimation of sea-surface temperatures from two infrared window measurements with different absorption. J. Geophys. Res. 80, 5113–5117.

McMillin, L., Crosby, D.S., 1984. Theory and validation of the multiple window sea surface temperature technique. J. Geophys. Research 89, 3655–3661.

McMillin, L., Crosby, D.S., 1985. Some physical interpretations of statistically derived coefficients for split-window corrections to satellite derived sea surface temperatures. Quart. J. Royal Meteorological Soc. 111, 867–871.

McPhaden, M.J., 2012. A 21st century shift in the relationship between ENSO SST and warm water volume anomalies. Geophys. Res. Lett. 39. https://doi.org/10.1029/2012GL051826.

McPhaden, M.J., Zhang, X., Hendon, H.H., Wheeler, M.C., 2006. Large scale dynamics and MJO forcing of ENSO variability. Geophys. Res. Lett. 33. https://doi.org/10.1029/2006GL026786.

McPhaden, M.J., Ando, K., Bourlès, B., Freitag, H.P., Lumpkin, R., Masumoto, Y., Murty, V.S.N., Nobre, P., Ravichandran, M., Vialard, J., Vousden, D., Yu, W., 2010. The global tropical moored buoy array. In: Hall, J., Harrison, D.E., Stammer, D. (Eds.), Proceedings of OceanObs'09: Sustained Ocean Observations and Information for Society (Vol 2), Venice, Italy, 21–25 September 2009. European Space Agency. https://doi.org/10.5270/OceanObs09.cwp.61. ESA Publication WPP-306, (16 pp.).

Meissner, T., Wentz, F., 2007. High quality sea surface temperature from the windsat radiometer: algorithm and validation. In: Proceedings of 2007 IEEE International Geoscience and Remote Sensing Symposium, Barcelona, Spain. IEEE, Barcelona, Spain. https://doi.org/10.1109/IGARSS.2007.4422933. 862–864 pp.

Meissner, T., Wentz, F.J., 2012. The emissivity of the ocean surface between 6 and 90 GHz over a large range of wind speeds and earth incidence angles. IEEE Trans. Geosci. Remote Sens. 50, 3004–3026. https://doi.org/10.1109/TGRS.2011.2179662.

Menzel, W.P., Purdom, J.F.W., 1994. Introducing GOES-I: the first of a new generation of geostationary operational environmental satellites. Bull. Am. Meteorol. Soc. 75, 757–781. https://doi.org/10.1175/1520-0477(1994)075<0757:IGITFO>2.0.CO;2.

Menzel, W.P., Smith, W.L., Herman, L.D., 1981. Visible infrared spin–scan radiometer atmospheric sounder radiometric calibration: an inflight evaluation from intercomparisons with HIRS and radiosonde measurements. Appl. Opt. 20, 3641–3644. https://doi.org/10.1364/AO.20.003641.

Merchant, C.J., Harris, A.R., 1999. Toward the elimination of bias in satellite retrievals of skin sea surface temperature. 2: comparison with in situ measurements. J. Geophys. Res. 104, 23579–23590.

Merchant, C.J., Harris, A.R., Maturi, E., MacCallum, S., 2005. Probabilistic physically based cloud screening of satellite infrared imagery for operational sea surface temperature retrieval. Q. J. R. Meteorol. Soc. 131, 2735–2755. https://doi.org/10.1256/qj.05.15.

Merchant, C.J., Filipiak, M.J., Le Borgne, P., Roquet, H., Autret, E., Piollé, J.F., Lavender, S., 2008a. Diurnal warm-layer events in the western Mediterranean and European shelf seas. Geophys. Res. Lett. 35, L04601. https://doi.org/10.1029/2007GL033071.

Merchant, C.J., LeBorgne, P., Marsouin, A., Roquet, H., 2008b. Optimal estimation of sea surface temperature from split-window observations. Remote Sens. Environ. 112, 2469–2484.

Merchant, C.J., Harris, A.R., Maturi, E., Embury, O., MacCallum, S.N., Mittaz, J., Old, C.P., 2009a. Sea surface temperature estimation from the Geostationary Operational Environmental Satellite-12 (GOES-12). J. Atmos. Ocean. Technol. 26, 570–581. https://doi.org/10.1175/2008jtecho596.1.

Merchant, C.J., Harris, A.R., Roquet, H., Le Borgne, P., 2009b. Retrieval characteristics of non-linear sea surface temperature from the advanced very high resolution radiometer. Geophys. Res. Lett. 36. https://doi.org/10.1029/2009gl039843.

Merchant, C.J., Le Borgne, P., Roquet, H., Marsouin, A., 2009c. Sea surface temperature from a geostationary satellite by optimal estimation. Remote Sens. Environ. 113, 445–457.

Merchant, C.J., Embury, O., Rayner, N.A., Berry, D.I., Corlett, G.K., Lean, K., Veal, K.L., Kent, E.C., Llewellyn-Jones, D.T., Remedios, J.J., Saunders, R., 2012. A 20 year independent record of sea surface temperature for climate from along track scanning radiometers. Journal of Geophysical Research 117. https://doi.org/10.1029/2012JC008400.

Merchant, C.J., Le Borgne, P., Roquet, H., Legendre, G., 2013. Extended optimal estimation techniques for sea surface temperature from the Spinning Enhanced Visible and Infra-Red Imager (SEVIRI). Remote Sens. Environ. 131, 287–297. https://doi.org/10.1016/j.rse.2012.12.019.

Merchant, C.J., Mittaz, J., Corlett, G.K., 2014. Climate Data Record Technical Advisory Group: Climate Data Assessment Framework, GHRSST Document, CDR-TAG_CDAF v 1.0.5 (24 pp.) Available at. https://www.ghrsst.org/wp-content/uploads/2018/01/CDR-TAG_CDAF-v1.0.5.pdf.

Merchant, C.J., Embury, O., Bulgin, C.E., Block, T., Corlett, G., Fiedler, E., Good, S.A., Mittaz, J., Rayner, N.A., Berry, D., Eastwood, S., Taylor, M., Tsushima, Y., Waterfall, A., Wilson, R., Donlon, C., 2019. Satellite-based time-series of sea-surface temperature since 1981 for climate applications. Scientific Data (In Press).

Merrill, R.T., 1988. Environmental influences on hurricane intensification. J. Atmos. Sci. 45, 1678–1687. https://doi.org/10.1175/1520-0469(1988)045<1678:Eiohi>2.0.Co;2.

Meyers, P.C., Shay, L.K., Brewster, J.K., 2014. Development and analysis of the systematically merged Atlantic regional temperature and salinity climatology for oceanic heat content estimates. J. Atmos. Ocean. Technol. 31, 131–149. https://doi.org/10.1175/jtech-d-13-00100.1.

Michelson, A.A., Morely, E.W., 1887. On the relative motion of the earth and the luminiferous ether. Am. J. Sci. 35, 333–345.

Miller, B.I., 1958. On the maximum intensity of hurricanes. J. Meteorol. 15, 184–195. https://doi.org/10.1175/1520-0469(1958)015<0184:Otmioh>2.0.Co;2.

Miller, A.J., Collins, M., Gualdi, S., Jensen, T.G., Misra, V., Pezzi, L.P., Pierce, D.W., Putrasahan, D., Seo, H., Tseng, Y.-H., 2017. Coupled ocean-atmosphere modeling and predictions. J. Mar. Res. 75, 361–402. https://doi.org/10.1357/002224017821836770.

Millot, C., Taupier-Letage, I., 2005. Circulation in the Mediterranean Sea. In: Saliot, A. (Ed.), The Mediterranean Sea. Springer Berlin Heidelberg, Berlin, Heidelberg, pp. 29–66. https://doi.org/10.1007/b107143. 978-3-540-31492-9.

Millot, C., Wald, L., 1980. The effect of Mistral wind on the Ligurian current near Provence. Oceanol. Acta 3, 399–402.

Minnett, P.J., 1986. A numerical study of the effects of anomalous North Atlantic atmospheric conditions on the infrared measurement of sea-surface temperature from space. Journal of Geophysical Research 91, 8509–8521.

Minnett, P.J., 1990. The regional optimization of infrared measurements of sea-surface temperature from space. J. Geophys. Res. 95 (13), 497–413,510.

Minnett, P.J., 1991. Consequences of sea surface temperature variability on the validation and applications of satellite measurements. Journal of Geophysical Research 96, 18,475–418,489.

Minnett, P.J., 1995. Measurements of the summer surface heat budget of the Northeast Water Polynya in 1992. J. Geophys. Res. 100, 4309–4322.

Minnett, P.J., 1999. The influence of solar zenith angle and cloud type on cloud radiative forcing at the surface in the Arctic. J. Clim. 12, 147–158.

Minnett, P.J., 2003. Radiometric measurements of the sea-surface skin temperature - the competing roles of the diurnal thermocline and the cool skin. Int. J. Remote Sens. 24, 5033–5047.

Minnett, P.J., 2010. The validation of sea surface temperature retrievals from spaceborne infrared radiometers. In: Barale, V., Gower, J.F.R., Alberotanza, L. (Eds.), Oceanography From Space, Revisited. Springer Science + Business Media B.V, 978-90-481-8681-5, pp. 273–295. https://doi.org/10.1007/978-90-481-8681-5.

Minnett, P.J., Corlett, G.K., 2012. A pathway to generating climate data records of sea-surface temperature from satellite measurements. Deep-Sea Res. II Top. Stud. Oceanogr. 77–80, 44–51. https://doi.org/10.1016/j.dsr2.2012.04.003.

Minnett, P.J., Kaiser-Weiss, A.K., 2012. Group for High Resolution Sea-Surface Temperature Discussion Document: Near-Surface Oceanic Temperature Gradients (7 pp.) Available at. https://www.ghrsst.org/wp-content/uploads/2016/10/SSTDefinitionsDiscussion.pdf.

Minnett, P.J., Smith, D.L., 2014. Postlaunch calibration and stability: thermal infrared satellite radiometers. In: Zibordi, G., Donlon, C.J., Parr, A.C. (Eds.), Experimental Methods in the Physical Sciences, Vol 47, Optical Radiometry for Ocean Climate Measurements. Academic Press, pp. 201–243. https://doi.org/10.1016/B978-0-12-417011-7.00008-8. 1079-4042.

Minnett, P.J., Eyre, J.R., Pescod, R.W., 1987. The variability of the North Atlantic marine atmosphere and its relevance to remote sensing. Int. J. Remote Sens. 8, 871–880. https://doi.org/10.1080/01431168708948695.

Minnett, P.J., Knuteson, R.O., Best, F.A., Osborne, B.J., Hanafin, J.A., Brown, O.B., 2001. The Marine-Atmospheric Emitted Radiance Interferometer (M-AERI), a high-accuracy, sea-going infrared spectroradiometer. J. Atmos. Ocean. Technol. 18, 994–1013.

Minnett, P.J., Smith, M., Ward, B., 2011. Measurements of the oceanic thermal skin effect. Deep-Sea Res. II Top. Stud. Oceanogr. 58, 861–868. https://doi.org/10.1016/j.dsr2.2010.10.024.

Minobe, S., Kuwano-Yoshida, A., Komori, N., Xie, S.-P., Small, R.J., 2008. Influence of the Gulf Stream on the troposphere. Nature 452, 206. https://doi.org/10.1038/nature06690. https://www.nature.com/articles/nature06690#supplementary-information.

Mittaz, J., Merchant, C.J., Woolliams, E.R., 2019. Applying principles of metrology to historical earth observations from satellites. Metrologia 56, 032002. https://doi.org/10.1088/1681-7575/ab1705.

Miyazawa, Y., Varlamov, S.M., Miyama, T., Guo, X., Hihara, T., Kiyomatsu, K., Kachi, M., Kurihara, Y., Murakami, H., 2017. Assimilation of high-resolution sea surface temperature data into an operational nowcast/forecast system around Japan using a multi-scale three-dimensional variational scheme. Ocean Dyn. 67, 713–728. https://doi.org/10.1007/s10236-017-1056-1.

Mollo-Christensen, E., Cornillon, P., Mascarenhas, A.D.S., 1981. Method for estimation of ocean current velocity from satellite images. Science 212, 661–662. https://doi.org/10.1126/science.212.4495.661.

Montanaro, M., Lunsford, A., Tesfaye, Z., Wenny, B., Reuter, D., 2014. Radiometric calibration methodology of the Landsat 8 thermal infrared sensor. Remote Sens. 6, 8803–8821.

Montenbruck, O., Gill, E., 2000. Satellite Orbits - Models, Methods and Applications. Springer978-3-540-67280-7https://doi.org/10.1007/978-3-642-58351-3.

Mumby, P.J., Skirving, W., Strong, A.E., Hardy, J.T., LeDrew, E.F., Hochberg, E.J., Stumpf, R.P., David, L.T., 2004. Remote sensing of coral reefs and their physical environment. Mar. Pollut. Bull. 48, 219–228. https://doi.org/10.1016/j.marpolbul.2003.10.031.

Muraleedharan, P.M., Pankajakshan, T., Harikrishnan, M., 2004. Validation of multi-channel scanning microwave radiometer on-board Oceansat-I. Curr. Sci. 87, 370–376.

Murtugudde, R., Wang, L., Hackert, E., Beauchamp, J., Christian, J., Busalacchi, A.J., 2004. Remote sensing of the Indo-Pacific region: ocean colour, sea level, winds and sea surface temperatures. Int. J. Remote Sens. 25, 1423–1435. https://doi.org/10.1080/01431160310001592391.

Nalli, N.R., Minnett, P.J., Maddy, E., McMillan, W.W., Goldberg, M.D., 2008a. Emissivity and reflection model for calculating unpolarized isotropic water surface-leaving radiance in the infrared. 2: validation using Fourier transform spectrometers. Appl. Opt. 47, 4649–4671. https://doi.org/10.1364/AO.47.004649.

Nalli, N.R., Minnett, P.J., van Delst, P., 2008b. Emissivity and reflection model for calculating unpolarized isotropic water surface-leaving radiance in the infrared. I: theoretical development and calculations. Appl. Opt. 47, 3701–3721. https://doi.org/10.1364/AO.47.003701.

Nerem, R.S., Beckley, B.D., Fasullo, J.T., Hamlington, B.D., Masters, D., Mitchum, G.T., 2018. Climate-change–driven accelerated sea-level rise detected in the altimeter era. Proc. Natl. Acad. Sci. 115, 2022–2025. https://doi.org/10.1073/pnas.1717312115.

Neumann, B., Vafeidis, A.T., Zimmermann, J., Nicholls, R.J., 2015. Future coastal population growth and exposure to sea-level rise and coastal flooding - a global assessment. PLoS One 10, e0118571. https://doi.org/10.1371/journal.pone.0118571.

Nicholls, R.J., Cazenave, A., 2010. Sea-level rise and its impact on coastal zones. Science 328, 1517–1520. https://doi.org/10.1126/science.1185782.

Nielsen-Englyst, P., L Høyer, J., Toudal Pedersen, L., L Gentemann, C., Alerskans, E., Block, T., Donlon, C., 2018. Optimal estimation of sea surface temperature from AMSR-E. Remote Sens. 10, 229.

Njoku, E.G., Abrams, M.J., Asrar, G., Marzano, F.S., Minnett, P., Salomonson, V.V., Singhroy, V., Turk, J. (Eds.), 2014. Encyclopedia of Remote Sensing, 1st ed. Springer-Verlag, New York978-0-387-36698-2, .

NRC, 2000. Issues in the Integration of Research and Operational Satellite Systems for Climate Research: II. Implementation. National Academy of Sciences, Washington, DC, USA, 0-309-06994-7pp. 82.

Nykjaer, L., 2009. Mediterranean Sea surface warming 1985–2006. Climate Research 39, 11 pp..

O'Carroll, A.G., Eyre, J.R., Saunders, R.W., 2008. Three-way error analysis between AATSR, AMSR-E, and in situ sea surface temperature observations. J. Atmos. Ocean. Technol. 25, 1197–1207.

O'Carroll, A.G., August, T., Le Borgne, P., Marsouin, A., 2012. The accuracy of SST retrievals from Metop-A IASI and AVHRR using the EUMETSAT OSI-SAF matchup dataset. Remote Sens. Environ. 126, 184–194. https://doi.org/10.1016/j.rse.2012.08.006.

O'Carroll, A.G., Armstrong, E.M., Beggs, H.M., Bouali, M., Casey, K.S., Corlett, G.K., Dash, P., Donlon, C.J., Gentemann, C.L., Hoeyer, J., Ignatov, A., Kabobah, K., Kachi, M., Kurihara, Y., Karagali, I., Maturi, E., Merchant, C.J., Marullo, S., Minnett, P.J., Pennybacker, M., Ramakrishnan, B., Ramsankaran, R., Santoleri, R., Sunder, S., Picart, S.S., Vázquez-Cuervo, J., Wimmer, W., 2019. Observational needs of sea surface temperature. Front. Mar. Sci. 6https://doi.org/10.3389/fmars.2019.00420. (Accepted, July 5, 2019).

Oddo, P., Adani, M., Pinardi, N., Fratianni, C., Tonani, M., Pettenuzzo, D., 2009. A nested Atlantic-Mediterranean Sea general circulation model for operational forecasting. Ocean Sci. 461–473.

Ohring, G., Wielicki, B., Spencer, R., Emery, B., Datla, R., 2005. Satellite instrument calibration for measuring global climate change: report of a workshop. Bull. Am. Meteorol. Soc. 86, 1303–1313.

Olmedo, E., Taupier-Letage, I., Turiel, A., Alvera-Azcárate, A., 2018. Improving SMOS sea surface salinity in the Western Mediterranean Sea through multivariate and multifractal analysis. Remote Sens. 10, 485.

Olsen, A., Triñanes, J., Wanninkhof, R., 2004. Sea-air flux of CO_2 in the Caribbean Sea estimated using in situ and remote sensing data. Remote Sens. Environ. 89, 309–325.

O'Neill, L.W., Esbensen, S.K., Thum, N., Samelson, R.M., Chelton, D.B., 2010. Dynamical analysis of the boundary layer and surface wind responses to mesoscale SST perturbations. J. Clim. 23, 559–581.

Ouaknine, J., Gode, S., Napierala, B., Viard, T., Foerster, U., Fray, S., Peacoke, P., Hartl, M., Hallibert, P., Durand, Y., 2013. MTG flexible combined imager optical design and performances. In: Proceedings of SPIE Optical Engineering + Applications. 8866 SPIE. https://doi.org/10.1117/12.2023078. 14 pp.

Palmen, E., 1948. On the formation and structure of tropical hurricanes. Geophysica 3, 26–38.

Parekh, A., Sharma, R., Sarkar, A., 2007. A comparative assessment of surface wind speed and sea surface temperature over the Indian Ocean by TMI, MSMR, and ERA-40. J. Atmos. Ocean. Technol. 24, 1131–1142. https://doi.org/10.1175/jtech2021.1.

Park, E.-B., Han, K.-S., Yeom, J.-M., Lee, C.-S., Ryu, J.-H., Kim, H., Kim, D.-H., 2015. Effects of GSICS correction on estimation of sea surface temperature using COMS data. Int. J. Remote Sens. 36, 1026–1037. https://doi.org/10.1080/01431161.2015.1007249.

Parkinson, C., Ward, A., King, M., 2006. Earth Science Reference Handbook: A Guide to NASA's Earth Science Program and Earth Observing Satellite Missions. National Aeronautics and Space Administration 277 pp.

Pascual, A., Ruiz, S., Olita, A., Troupin, C., Claret, M., Casas, B., Mourre, B., Poulain, P.-M., Tovar-Sanchez, A., Capet, A., Mason, E., Allen, J.T., Mahadevan, A., Tintoré, J., 2017. A multiplatform experiment to unravel meso- and submesoscale processes in an intense front (AlborEx). Front. Mar. Sci. 4. https://doi.org/10.3389/fmars.2017.00039.

Pastor, F., Valiente, J.A., Palau, J.L., 2018. Sea surface temperature in the Mediterranean: trends and spatial patterns (1982–2016). Pure Appl. Geophys. 175, 4017–4029. https://doi.org/10.1007/s00024-017-1739-z.

Pearson, K., Merchant, C., Embury, O., Donlon, C., 2018. The role of advanced microwave scanning radiometer 2 channels within an optimal estimation scheme for sea surface temperature. Remote Sens. 10, 90.

Peralta-Ferriz, C., Woodgate, R.A., 2015. Seasonal and interannual variability of pan-Arctic surface mixed layer properties from 1979 to 2012 from hydrographic data, and the dominance of stratification for multiyear mixed layer depth shoaling. Prog. Oceanogr. 134, 19–53. https://doi.org/10.1016/j.pocean.2014.12.005.

Perlin, N., de Szoeke, S.P., Chelton, D.B., Samelson, R.M., Skyllingstad, E.D., O'Neill, L.W., 2014. Modeling the atmospheric boundary layer wind response to mesoscale sea surface temperature perturbations. Mon. Weather Rev. 142, 4284–4307. https://doi.org/10.1175/mwr-d-13-00332.1.

Petrenko, B., Ignatov, A., Kihai, Y., Stroup, J., Dash, P., 2014. Evaluation and selection of SST regression algorithms for JPSS VIIRS. Journal of Geophysical Research: Atmospheres 119https://doi.org/10.1002/2013JD020637. 2013JD020637.

Piepmeier, J.R., Focardi, P., Horgan, K.A., Knuble, J., Ehsan, N., Lucey, J., Brambora, C., Brown, P.R., Hoffman, P.J., French, R.T., Mikhaylov, R.L., Kwack, E., Slimko, E.M., Dawson, D.E., Hudson, D., Peng, J., Mohammed, P.N., Amici, G.D., Freedman, A.P., Medeiros, J., Sacks, F., Estep, R., Spencer, M.W., Chen, C.W., Wheeler, K.B., Edelstein, W.N., O'Neill, P.E., Njoku, E.G., 2017. SMAP L-band microwave radiometer: instrument design and first year on orbit. IEEE Trans. Geosci. Remote Sens. 55, 1954–1966. https://doi.org/10.1109/TGRS.2016.2631978.

Pinardi, N., Coppini, G., 2010. Preface "operational oceanography in the Mediterranean Sea: the second stage of development". Ocean Sci. 6, 263–267. https://doi.org/10.5194/os-6-263-2010.

Pinardi, N., Woods, J., 2002. Ocean Forecasting: Conceptual Basis and Applications. Springer Science & Business Media, Berlin, Germany, 3540679642pp. 472.

Pinardi, N., Allen, I., Demirov, E., De Mey, P., Korres, G., Lascaratos, A., Le Traon, P.-Y., Maillard, C., Manzella, G., Tziavos, C., 2003. The Mediterranean Ocean forecasting system: first phase of implementation (1998–2001). Ann. Geophys. 21, 3–20.

Pisano, A., Buongiorno Nardelli, B., Tronconi, C., Santoleri, R., 2016. The new

Mediterranean optimally interpolated pathfinder AVHRR SST dataset (1982–2012). Remote Sens. Environ. 176, 107–116. https://doi.org/10.1016/j.rse.2016.01.019.

Poli, P., Lucas, M., O'Carroll, A., Le Menn, M., David, A., Corlett, G.K., Blouch, P., Meldrum, D., Merchant, C.J., Belbeoch, M., Herklotz, K., 2018. The Copernicus surface velocity platform drifter with barometer and reference sensor for temperature (SVP-BRST): genesis, design, and initial results. Ocean Sci. Discuss. 2018, 1–34. https://doi.org/10.5194/os-2018-109.

Prabhakara, C., Wang, I., Chang, A.T.C., Gloersen, P., 1983. A statistical examination of Nimbus-7 SMMR data and remote sensing of sea surface temperature, liquid water content in the atmosphere and surface wind speed. J. Clim. Appl. Meteorol. 22, 2023–2037. https://doi.org/10.1175/1520-0450(1983)022<2023:Aseons>2.0.Co;2.

Prata, A.J., Cechet, R.P., Barton, I.J., Llewellyn-Jones, D.T., 1990. The along-track scanning radiometer for ERS-1 - scan geometry and data simulation. IEEE Trans. Geosci. Remote Sens. 28, 3–13.

Price, J.F., Weller, R.A., Pinkel, R., 1986. Diurnal cycling: observations and models of the upper ocean response to diurnal heating, cooling and wind mixing. J. Geophys. Res. 91, 8411–8427.

Price, J.F., Weller, R.A., Bowers, C.M., Briscoe, M.G., 1987. Diurnal response of sea surface temperature observed at the Long-Term Upper Ocean Study (37oN, 70oW) in the Sargasso Sea. J. Geophys. Research 92 (14), 480–14490.

Prospero, J.M., 1999. Long-range transport of mineral dust in the global atmosphere: impact of African dust on the environment of the southeastern United States. Proceedings of the National Academy of Science USA 96, 3396–3403.

Prospero, J.M., Carlson, T.N., 1972. Vertical and areal distribution of Saharan dust over the western Equatorial North Atlantic Ocean. J. Geophys. Res. 77, 5255–5265.

Prospero, J.M., Ginoux, P., Torres, O., Nicholson, S.E., Gill, T.E., 2002. Environmental characterization of global sources of atmospheric soil dust identified with the Nimbus 7 Total Ozone Mapping Spectrometer (TOMS) absorbing aerosol product. Rev. Geophys. 40.

Puschell, J.J., Lowe, H.A., Jeter, J.W., Kus, S.M., Hurt, W.T., Gilman, D., Rogers, D.L., Hoelter, R.L., Ravella, R., 2002. Japanese advanced meteorological imager: a next-generation GEO imager for MTSAT-1R. In: Proceedings of International Symposium on Optical Science and Technology, Earth Observing Systems VII., Seattle, WA, USA, 4814. SPIE. https://doi.org/10.1117/12.453755. 152–161 pp.

Rabe, B., Karcher, M., Schauer, U., Toole, J.M., Krishfield, R.A., Pisarev, S., Kauker, F., Gerdes, R., Kikuchi, T., 2011. An assessment of Arctic Ocean freshwater content changes from the 1990s to the 2006–2008 period. Deep-Sea Res. I Oceanogr. Res. Pap. 58, 173–185. https://doi.org/10.1016/j.dsr.2010.12.002.

Rajeev, K., Parameswaran, K., Nair, S.K., Meenu, S., 2008. Observational evidence for the radiative impact of Indonesian smoke in modulating the sea surface temperature of the equatorial Indian Ocean. J. Geophys. Res. 113. https://doi.org/10.1029/2007jd009611.

Ramage, C.S., 1974. The typhoons of October 1970 in the South China Sea: intensification, decay and ocean interaction. J. Appl. Meteorol. 13, 739–751. https://doi.org/10.1175/1520-0450(1974)013<0739:Ttooit>2.0.Co;2.

Randelhoff, A., Fer, I., Sundfjord, A., 2017. Turbulent upper-ocean mixing affected by meltwater layers during Arctic summer. J. Phys. Oceanogr. 47, 835–853. https://doi.org/10.1175/jpo-d-16-0200.1.

Rappaport, E.N., Franklin, J.L., Schumacher, A.B., DeMaria, M., Shay, L.K., Gibney, E.J., 2010. Tropical cyclone intensity change before U.S. Gulf Coast landfall. Weather Forecast. 25, 1380–1396. https://doi.org/10.1175/2010waf2222369.1.

Rayner, N.A., Brohan, P., Parker, D.E., Folland, C.K., Kennedy, J.J., Vanicek, M., Ansell, T.J., Tett, S.F.B., 2006. Improved analyses of changes and uncertainties in sea surface temperature measured in situ since the mid-nineteenth century: the HadSST2 dataset. J. Clim. 19, 446–469.

Reul, N., Chapron, B., Lee, T., Donlon, C., Boutin, J., Alory, G., 2014. Sea surface salinity structure of the meandering Gulf Stream revealed by SMOS sensor. Geophys. Res. Lett. 41, 3141–3148. https://doi.org/10.1002/2014GL059215.

Reynolds, R.W., 1988. A real-time global sea surface temperature analysis. J. Clim. 1, 75–87. https://doi.org/10.1175/1520-0442(1988)001<0075:Artgss>2.0.Co;2.

Reynolds, R.W., Marsico, D.C., 1993. An improved real-time global sea surface temperature analysis. J. Clim. 6, 114–119. https://doi.org/10.1175/1520-0442(1993)006<0114:Airtgs>2.0.Co;2.

Reynolds, R.W., Smith, T.M., 1994. Improved global sea surface temperature analysis using optimum interpolation. J. Clim. 7, 929–948.

Rice, J.P., Butler, J.J., Johnson, B.C., Minnett, P.J., Maillet, K.A., Nightingale, T.J., Hook, S.J., Abtahi, A., Donlon, C.J., Barton, I.J., 2004. The Miami2001 infrared radiometer calibration and intercomparison: 1. Laboratory characterization of blackbody targets. J. Atmos. Ocean. Technol. 21, 258–267.

Richter-Menge, J.A., Perovich, D.K., Pegau, W.S., 2001. Summer ice dynamics during SHEBA and its effect on the ocean heat content. Ann. Glaciol. 33, 201–206. https://doi.org/10.3189/172756401781818176.

Rignot, E., Velicogna, I., van den Broeke, M.R., Monaghan, A., Lenaerts, J.T.M., 2011. Acceleration of the contribution of the Greenland and Antarctic ice sheets to sea level rise. Geophys. Res. Lett. 38. https://doi.org/10.1029/2011GL046583.

Rio, M.-H., Santoleri, R., 2018. Improved global surface currents from the merging of altimetry and sea surface temperature data. Remote Sens. Environ. 216, 770–785. https://doi.org/10.1016/j.rse.2018.06.003.

Rio, M.-H., Santoleri, R., Bourdalle-Badie, R., Griffa, A., Piterbarg, L., Taburet, G., 2016. Improving the altimeter-derived surface currents using high-resolution sea surface temperature data: a feasability study based on model outputs. J. Atmos. Ocean. Technol. 33, 2769–2784. https://doi.org/10.1175/jtech-d-16-0017.1.

Robinson, I.S., 2004. Measuring the Oceans From Space: The Principles and Methods of Satellite Oceanography. Springer Science & Business Media978-3-540-42647-9.

Robinson, I.S., 2010. Discovering the Ocean from Space. Springer-Verlag, Berlin Heidelberg978-3-540-24430-1https://doi.org/10.1007/978-3-540-68322-3.

Robinson, A.R., Golnaraghi, M., 1993. Circulation and dynamics of the Eastern Mediterranean Sea; quasi-synoptic data-driven simulations. Deep-Sea Res. II Top. Stud. Oceanogr. 40, 1207–1246. https://doi.org/10.1016/0967-0645(93)90068-X.

Rodgers, C.D., 2000. Inverse Methods for Atmospheric Sounding: Theory and Practice. World Scientific (ISBN 9789810227401).

Roemmich, D., Johnson, G., Riser, S., Davis, R., Gilson, J., Owens, W.B., Garzoli, S., Schmid, C., Ignaszewski, M., 2009. The Argo program: observing the global ocean with profiling floats. Oceanography 22, 34–43.

Santoleri, R., Marullo, S., Böhm, E., 1991. An objective analysis scheme for AVHRR imagery. Int. J. Remote Sens. 12, 681–693. https://doi.org/10.1080/01431169108929685.

Santoleri, R., Nardelli, B.B., Banzon, V., 2002. Sea surface characterization by combined data. In: Marzano, F.S., Visconti, G. (Eds.), Remote Sensing of Atmosphere and Ocean From Space: Models, Instruments and Techniques. Springer Netherlands, Dordrecht, pp. 201–214. https://doi.org/10.1007/0-306-48150-2_13. 978-0-306-48150-5.

Saunders, R.W., Blackmore, T.A., Candy, B., Francis, P.N., Hewison, T.J., 2013. Monitoring satellite radiance biases using NWP models. IEEE Trans. Geosci. Remote Sens. 51, 1124–1138. https://doi.org/10.1109/TGRS.2012.2229283.

Schiller, A., Godfrey, J.S., 2005. A diagnostic model of the diurnal cycle of sea surface temperature for use in coupled ocean-atmosphere models. J. Geophys. Res. 110, C11014.

Schmid, J., 2012. The SEVIRI Instrument (10 pp.). ESA ESTEC, Noordwijk, The Netherlands Available at. https://www.eumetsat.int/website/wcm/idc/groups/ops/documents/document/mday/mde1/~edisp/pdf_ten_msg_seviri_instrument.pdf.

von Schuckmann, K., Le Traon, P.-Y., Smith, N., Pascual, A., Brasseur, P., Fennel, K., Djavidnia, S., 2018. Copernicus marine service ocean state report. Journal of Operational Oceanography 11, S1–S142. https://doi.org/10.1080/1755876X.2018.1489208.

Schueler, C.F., Lee, T.F., Miller, S.D., 2013. VIIRS constant spatial-resolution advantages. Int. J. Remote Sens. 34, 5761–5777. https://doi.org/10.1080/01431161.2013.796102.

Screen, J.A., Simmonds, I., Deser, C., Tomas, R., 2013. The atmospheric response to three decades of observed Arctic Sea ice loss. J. Clim. 26, 1230–1248. https://doi.org/10.1175/jcli-d-12-00063.1.

Shaltout, M., Omstedt, A., 2014. Recent sea surface temperature trends and future scenarios for the Mediterranean Sea. Oceanologia 56, 411–443. https://doi.org/10.5697/oc.56-3.411.

Shay, L.K., Goni, G.J., Black, P.G., 2000. Effects of a warm oceanic feature on hurricane opal. Mon. Weather Rev. 128, 1366–1383.

Shibata, A., 2006. Features of ocean microwave emission changed by wind at 6 GHz. J. Oceanogr. 62, 321–330.

Shine, K.P., Ptashnik, I.V., Rädel, G., 2012. The water vapour continuum: brief history and recent developments. Surv. Geophys. 33, 535–555. https://doi.org/10.1007/s10712-011-9170-y.

Ships4SST, 2019. The recommended ISFRN L2R data specification and user manual (52 pp.) Available at. http://www.shipborne-radiometer.org/sites/shipborne-radiometer/files/documents/Recommended%20ISFRN%20L2R%20Data%20Specification%20and%20User%20Manual%20v1.2%20rev0.pdf.

Simeoni, D., Astruc, P., Miras, D., Alis, C., Andreis, O., Scheidel, D., Degrelle, C., Nicol, P., Bailly, B., Guiard, P., Clauss, A., Blumstein, D., Maciaszek, T., Chalon, G., Carlier, T., Kayal, G., 2004. Design and development of IASI instrument. In: Proceedings of Optical Science and Technology, the SPIE 49th Annual Meeting. 5543 SPIE. https://doi.org/10.1117/12.561090. 12 pp.

Simpson, J.J., Yhann, S.R., 1994. Reduction of noise in AVHRR channel 3 data with minimum distortion. IEEE Trans. Geosci. Remote Sens. 32, 315–328. https://doi.org/10.1109/36.295047.

Skliris, N., Sofianos, S., Gkanasos, A., Mantziafou, A., Vervatis, V., Axaopoulos, P., Lascaratos, A., 2012. Decadal scale variability of sea surface temperature in the Mediterranean Sea in relation to atmospheric variability. Ocean Dyn. 62, 13–30. https://doi.org/10.1007/s10236-011-0493-5.

Small, R.J., deSzoeke, S.P., Xie, S.P., O'Neill, L., Seo, H., Song, Q., Cornillon, P., Spall, M., Minobe, S., 2008. Air–sea interaction over ocean fronts and eddies. Dynamics of Atmospheres and Oceans 45, 274–319. https://doi.org/10.1016/j.dynatmoce.2008.01.001.

Smedsrud, L.H., Esau, I., Ingvaldsen, R.B., Eldevik, T., Haugan, P.M., Li, C., Lien, V.S., Olsen, A., Omar, A.M., Otterå, O.H., Risebrobakken, B., Sandø, A.B., Semenov, V.A., Sorokina, S.A., 2013. The role of the Barents Sea in the Arctic climate system. Rev. Geophys. 51, 415–449. https://doi.org/10.1002/rog.20017.

Smith, N., Koblinsky, C., 2001. The ocean observing system for the 21st century, a consensus statement. In: Observing the Oceans in the 21st Century, pp. 1–25 (ISBN: 0642706182).

Smith, W.L., Knuteson, R.O., Revercomb, H.E., Feltz, W., Howell, H.B., Menzel, W.P., Nalli, N., Brown, O., Brown, J., Minnett, P., McKeown, W., 1996. Observations of the infrared radiative properties of the ocean - implications for the measurement of sea surface temperature via satellite remote sensing. Bull. Am. Meteorol. Soc. 77, 41–51.

Smith, E.A., Asrar, G., Furuhama, Y., Ginati, A., Mugnai, A., Nakamura, K., Adler, R.F., Chou, M.-D., Desbois, M., Durning, J.F., 2007. International global precipitation measurement (GPM) program and mission: an overview. In: Measuring Precipitation From Space. Springer, pp. 611–653 (1402058349).

Smith, D., Mutlow, C., Delderfield, J., Watkins, B., Mason, G., 2012. ATSR infrared radiometric calibration and in-orbit performance. Remote Sens. Environ. 116, 4–16. https://doi.org/10.1016/j.rse.2011.01.027.

Smith, D.L., Nightingale, T.J., Mortimer, H., Middleton, K., Edeson, R., Cox, C.V., Mutlow, C.T., Maddison, B.J., Coppo, P., 2014. Calibration approach and plan for the sea and land surface temperature radiometer. J. Appl. Remote. Sens. 8https://doi.org/10.

1117/1.JRS.8.084980. 084980-084980.

Smith, M., Stammerjohn, S., Persson, O., Rainville, L., Liu, G., Perrie, W., Robertson, R., Jackson, J., Thomson, J., 2018. Episodic reversal of autumn ice advance caused by release of ocean heat in the Beaufort Sea. Journal of Geophysical Research: Oceans 123, 3164–3185. https://doi.org/10.1002/2018JC013764.

Smyth, T.J., Miller, P.I., Groom, S.B., Lavender, S.J., 2001. Remote sensing of sea surface temperature and chlorophyll during Lagrangian experiments at the Iberian margin. Prog. Oceanogr. 51, 269–281. https://doi.org/10.1016/S0079-6611(01)00070-2.

Soloviev, A.V., Lukas, R., 2014. The Near-Surface Layer of the Ocean: Structure, Dynamics, and Applications, Second edition. Springer, New York978-94-007-7620-3https://doi.org/10.1007/978-94-007-7621-0.

Song, Q., Cornillon, P., Hara, T., 2006. Surface wind response to oceanic fronts. Journal of Geophysical Research: Oceans 111. https://doi.org/10.1029/2006jc003680.

Steele, M., Dickinson, S., 2016. The phenology of Arctic Ocean surface warming. Journal of Geophysical Research: Oceans 121, 6847–6861. https://doi.org/10.1002/2016JC012089.

Steele, M., Ermold, W., 2015. Loitering of the retreating sea ice edge in the Arctic seas. Journal of Geophysical Research: Oceans 120, 7699–7721. https://doi.org/10.1002/2015JC011182.

Steele, M., Ermold, W., Zhang, J., 2008. Arctic Ocean surface warming trends over the past 100 years. Geophys. Res. Lett. 35. https://doi.org/10.1029/2007GL031651.

Steele, M., Zhang, J., Ermold, W., 2010. Mechanisms of summertime upper Arctic Ocean warming and the effect on sea ice melt. Journal of Geophysical Research: Oceans 115. https://doi.org/10.1029/2009JC005849.

Stommel, H., Saunders, K., Simmons, W., Cooper, J., 1969. Observations of the diurnal thermocline. Deep Sea Research Supplement 16, 269–284.

Stramma, L., Cornillon, P., Weller, R.A., Price, J.F., Briscoe, M.G., 1986. Large diurnal sea surface temperature variability: satellite and in situ measurements. J. Phys. Oceanogr. 16, 827–837.

Stroeve, J.C., Crawford, A.D., Stammerjohn, S., 2016. Using timing of ice retreat to predict timing of fall freeze-up in the Arctic. Geophys. Res. Lett. 43, 6332–6340. https://doi.org/10.1002/2016GL069314.

Strong, A.E., McClain, E.P., 1984. Improved ocean surface temperatures from space - comparisons with drifting buoys. Bull. Am. Meteorol. Soc. 65, 138–142.

Strong, C., Rigor, I.G., 2013. Arctic marginal ice zone trending wider in summer and narrower in winter. Geophys. Res. Lett. 40, 4864–4868. https://doi.org/10.1002/grl.50928.

Stuart, V., Platt, T., Sathyendranath, S., 2011. The future of fisheries science in management: a remote-sensing perspective. ICES J. Mar. Sci. 68, 644–650. https://doi.org/10.1093/icesjms/fsq200.

Stuart-Menteth, A., Robinson, I.S., Challenor, P.G., 2003. A global study of diurnal warming using satellite-derived sea surface temperature. J. Geophys. Res. 108, 3155.

Stuart-Menteth, A.C., Robinson, I.S., Donlon, C.J., 2005a. Sensitivity of the diurnal warm layer to meteorological fluctuations. Part 2: a new parameterisation for diurnal warming. Journal of Atmospheric and Ocean Science 10, 209–234.

Stuart-Menteth, A.C., Robinson, I.S., Welller, R.A., Donlon, C.J., 2005b. Sensitivity of the diurnal warm layer to meteorological fluctuations part 1: observations. Journal of Atmospheric and Ocean Science 10, 193–208.

Sykes, P., While, J., Sellar, A., Martin, M., 2011. Diurnal variability in sea surface temperature: observation and model assessment. In: Forecasting Research Technical Report. 556 UK Met Office, Exeter, UK 42 pp.

Szczodrak, M., Minnett, P.J., Evans, R.H., 2014. The effects of anomalous atmospheres on the accuracy of infrared sea-surface temperature retrievals: dry air layer intrusions over the tropical ocean. Remote Sens. Environ. 140, 450–465. https://doi.org/10.1016/j.rse.2013.09.010.

Szekielda, K.-H., Salomonson, V., Allison, L.J., 1972. Rapid variations of sea surface temperature in the Persian Gulf as recorded by Nimbus 2 HRIR. Limnol. Oceanogr. 17, 307–309. https://doi.org/10.4319/lo.1972.17.2.0307.

Taberner, M., Shutler, J., Walker, P., Poulter, D., Piolle, J., Donlon, C., Guidetti, V., 2013. The ESA FELYX high resolution diagnostic data set system design and implementation. ISPRS-International Archives of the Photogrammetry, Remote Sensing and Spatial Information Sciences 243–249. https://doi.org/10.5194/isprsarchives-XL-7-W2-243-2013.

Tanaka, K., Okamura, Y., Mokuno, M., Amano, T., Yoshida, J., 2018. First year on-orbit calibration activities of SGLI on GCOM-C satellite. In: Proceedings of SPIE Asia-Pacific Remote Sensing, Honolulu, Hawaii, USA. 10781 SPIE. https://doi.org/10.1117/12.2324703. 10 pp.

Tandeo, P., Chapron, B., Ba, S.O., Autret, E., Fablet, R., 2014. Segmentation of mesoscale ocean surface dynamics using satellite SST and SSH observations. IEEE Trans. Geoscience and Remote Sensing 52, 4227–4235.

Taylor, B.N., Thompson, A., 2008. The International System of Units (SI), 8th edition. National Institute of Standards and Technology, Washington DC, USA.

Theocharous, E., Fox, N.P., Barker-Snook, I., Niclòs, R., Santos, V.G., Minnett, P.J., Göttsche, F.M., Poutier, L., Morgan, N., Nightingale, T., Wimmer, W., Høyer, J., Zhang, K., Yang, M., Guan, L., Arbelo, M., Donlon, C.J., 2019. The 2016 CEOS infrared radiometer comparison: part II: laboratory comparison of radiation thermometers. J. Atmos. Ocean. Technol. 36, 1079–1092. https://doi.org/10.1175/jtech-d-18-0032.1.

Thiébaux, J., Rogers, E., Wang, W., Katz, B., 2003. A new high-resolution blended real-time global sea surface temperature analysis. Bull. Am. Meteorol. Soc. 84, 645–656. https://doi.org/10.1175/bams-84-5-645.

Thomas, A.C., Blanco, J.L., Carr, M.E., Strub, P.T., Osses, J., 2001. Satellite-measured chlorophyll and temperature variability off northern Chile during the 1996–1998 La Niña and El Niño. Journal of Geophysical Research: Oceans 106, 899–915. https://doi.org/10.1029/1999JC000052.

Thomas, A.C., Ted Strub, P., Weatherbee, R.A., James, C., 2012. Satellite views of Pacific chlorophyll variability: comparisons to physical variability, local versus nonlocal influences and links to climate indices. Deep-Sea Res. II Top. Stud. Oceanogr. 77-80, 99–116. https://doi.org/10.1016/j.dsr2.2012.04.008.

Tonooka, H., Palluconi, F.D., Hook, S.J., Matsunaga, T., 2005. Vicarious calibration of ASTER thermal infrared bands. IEEE Trans. Geosci. Remote Sens. 43, 2733–2746. https://doi.org/10.1109/TGRS.2005.857885.

Trinh, R.C., Fichot, C.G., Gierach, M.M., Holt, B., Malakar, N.K., Hulley, G., Smith, J., 2017. Application of Landsat 8 for monitoring impacts of wastewater discharge on coastal water quality. Front. Mar. Sci. 4. https://doi.org/10.3389/fmars.2017.00329.

Trishchenko, A.P., Fedosejevs, G., Li, Z., Cihlar, J., 2002. Trends and uncertainties in thermal calibration of AVHRR radiometers onboard NOAA-9 to NOAA-16. Journal of Geophysical Research: Atmospheres 107, 4778. https://doi.org/10.1029/2002JD002353.

Tyagi, G., Babu, K.N., Mathur, A.K., Solanki, H.A., 2018. INSAT-3D and MODIS retrieved sea surface temperature validation and assessment over waters surrounding the Indian subcontinent. Int. J. Remote Sens. 39, 1575–1592. https://doi.org/10.1080/01431161.2017.1407051.

Uma, S.B., Donald, A.W., Martha, K.R., Peter, A.B., Howard, E.E., Josefino, C.C., Jorge, E.P., Compton, J.T., Michael, S., Wendy, E., Jinlun, Z., 2017. Changing seasonality of panarctic tundra vegetation in relationship to climatic variables. Environ. Res. Lett. 12, 055003.

Vazquez-Cuervo, J., Font, J., Martinez-Benjamin, J.J., 1996. Observations on the circulation in the Alboran Sea using ERSI altimetry and sea surface temperature data. J. Phys. Oceanogr. 26, 1426–1439. https://doi.org/10.1175/1520-0485(1996)026<1426:Ootcit>2.0.Co;2.

Vazquez-Cuervo, J., Gomez-Valdes, J., Bouali, M., Miranda, L.E., Van der Stocken, T., Tang, W., Gentemann, C., 2019. Using saildrones to validate satellite-derived sea surface salinity and sea surface temperature along the California/Baja Coast. Remote Sensing 11 (1964). https://doi.org/10.3390/rs11171964. (In reveiw).

Vincent, R.F., Marsden, R.F., Minnett, P.J., Buckley, J.R., 2008a. Arctic waters and marginal ice zones: part 2 - an investigation of Arctic atmospheric infrared absorption for AVHRR sea surface temperature estimates. J. Geophys. Res. 113, C08044. https://doi.org/10.1029/2007JC004354.

Vincent, R.F., Marsden, R.F., Minnett, P.J., Creber, K.A.M., Buckley, J.R., 2008b. Arctic waters and marginal ice zones: a composite Arctic Sea surface temperature algorithm using satellite thermal data. J. Geophys. Res. 113, C04021. https://doi.org/10.1029/2007JC004353.

Voosen, P., 2018. Saildrone fleet could help replace aging buoys. Science 359, 1082. https://doi.org/10.1126/science.359.6380.1082.

Wald, L., Nihous, G., 1980. Ligurian Sea: annual variation of the sea surface thermal structure as detected by satellite NOAA-5. Oceanol. Acta 3, 465–469.

Wallner, O., Reinert, T., Straif, C., 2017. METIMAGE: a spectro-radiometer for the VII mission onboard METOP-SG. In: Cugny, Bruno, Karafolas, Nikos, Sodnik, Z. (Eds.), Proceedings of International Conference on Space Optics — ICSO 2016, Biarritz, France. 10562 SPIE. https://doi.org/10.1117/12.2296103. 8 pp.

Walton, C.C., 2016. A review of differential absorption algorithms utilized at NOAA for measuring sea surface temperature with satellite radiometers. Remote Sens. Environ. 187, 434–446. https://doi.org/10.1016/j.rse.2016.10.011.

Walton, C.C., Pichel, W.G., Sapper, J.F., May, D.A., 1998. The development and operational application of nonlinear algorithms for the measurement of sea surface temperatures with the NOAA polar-orbiting environmental satellites. J. Geophys. Res. 103 (27), 999–928,012.

Wang, Y., Ientilucci, E., 2018. A practical approach to Landsat 8 TIRS stray light correction using multi-sensor measurements. Remote Sens. 10, 589.

Wang, S., Cui, P., Zhang, P., Ran, M., Lu, F., Wang, W., 2014. FY-3C/VIRR SST algorithm and cal/val activities at NSMC/CMA. In: Proceedings of SPIE Asia-Pacific Remote Sensing. 9261 SPIE. https://doi.org/10.1117/12.2068773. 8 pp.

Wang, D., Pan, D., Wei, J.-A., Gong, F., Zhu, Q., Chen, P., 2016. Monitoring thermal discharge from a nuclear plant through Landsat 8. In: Proceedings of SPIE Remote Sensing of the Ocean, Sea Ice, Coastal Waters, and Large Water Regions. 9999 SPIE. https://doi.org/10.1117/12.2242253. 9 pp.

Wang, Y., Ientilucci, E.J., Raqueno, N.G., Schott, J.R., 2017. Landsat 8 TIRS calibration with external sensors. In: Proceedings of SPIE Earth Observing Systems XXII, San Diego, CA, USA. 10402 SPIE. https://doi.org/10.1117/12.2272766. 11 pp.

Wanninkhof, R., Asher, W.E., Ho, D.T., Sweeney, C., McGillis, W.R., 2009. Advances in quantifying air-sea gas exchange and environmental forcing. Annu. Rev. Mar. Sci. 1, 213–244. https://doi.org/10.1146/annurev.marine.010908.163742.

Wanninkhof, R., Park, G.H., Takahashi, T., Sweeney, C., Feely, R., Nojiri, Y., Gruber, N., Doney, S.C., McKinley, G.A., Lenton, A., Le Quéré, C., Heinze, C., Schwinger, J., Graven, H., Khatiwala, S., 2013. Global Ocean carbon uptake: magnitude, variability and trends. Biogeosciences 10, 1983–2000. https://doi.org/10.5194/bg-10-1983-2013.

Ward, B., 2006. Near-surface ocean temperature. J. Geophys. Res. 111, C02005. https://doi.org/10.1029/2004JC002689.

Warnecke, G., Allison, L.J., McMillin, L.M., Szekielda, K.-H., 1971. Remote sensing of ocean currents and sea surface temperature changes derived from the Nimbus II satellite. J. Phys. Oceanogr. 1, 45–60. https://doi.org/10.1175/1520-0485(1971)001<0045:Rsooca>2.0.Co;2.

Warren, D., 1989. AVHRR channel-3 noise and methods for its removal. Int. J. Remote Sens. 10, 645–651. https://doi.org/10.1080/01431168908903905.

Webster, P.J., Clayson, C.A., Curry, J.A., 1996. Clouds, radiation, and the diurnal cycle of sea surface temperature in the tropical western Pacific. J. Clim. 9, 1712–1730.

While, J., Mao, C., Martin, M.J., Roberts-Jones, J., Sykes, P.A., Good, S.A., McLaren, A.J., 2017. An operational analysis system for the global diurnal cycle of sea surface temperature: implementation and validation. Q. J. R. Meteorol. Soc. 143, 1787–1803. https://doi.org/10.1002/qj.3036.

Wickramaratna, K., Kubat, M., Minnett, P., 2008. Discovering numeric laws, a case study: CO_2 fugacity in the ocean. Intelligent Data Analysis 12, 379–391.

Wilheit, T.T., 1979. A model for the microwave emissivity of the ocean's surface as a function of wind speed. IEEE Trans. Geosci. Electron. 17, 244–249. https://doi.org/10.1109/TGE.1979.294653.

Wimmer, W., Robinson, I.S., 2016. The ISAR instrument uncertainty model. J. Atmos. Ocean. Technol. 33, 2415–2433. https://doi.org/10.1175/jtech-d-16-0096.1.

Wong, E.W., Minnett, P.J., 2018. The response of the ocean thermal skin layer to variations in incident infrared radiation. Journal of Geophysical Research: Oceans 123, 19. https://doi.org/10.1002/2017JC013351.

Woods, J.D., Barkmann, W., 1986. The response of the upper ocean to solar heating. I: the mixed layer. Q. J. R. Meteorol. Soc. 112, 1–27. https://doi.org/10.1002/qj.49711247102.

Woods, J.D., Barkmann, W., Horch, A., 1984. Solar heating of the oceans - diurnal, seasonal and meridional variations. Q. J. R. Meteorol. Soc. 110, 633–686. https://doi.org/10.1002/qj.49711046505.

Worley, S.J., Woodruff, S.D., Reynolds, R.W., Lubker, S.J., Lott, N., 2005. ICOADS release 2.1 data and products. Int. J. Climatol. 25, 823–842. https://doi.org/10.1002/joc.1166.

Wu, F., Cornillon, P., Boussidi, B., Guan, L., 2017. Determining the pixel-to-pixel uncertainty in satellite-derived SST fields. Remote Sens. 9. https://doi.org/10.3390/rs9090877.

Xiong, X., Butler, J., Wu, A., Chiang, K.V., Efremova, B., Madhavan, S., McIntire, J., Oudrari, H., 2012. Comparison of MODIS and VIIRS onboard blackbody performance. In: Meynart, R., Neeck, S.P., Shimoda, H. (Eds.), Proceedings of Proc. SPIE 8533, Sensors, Systems, and Next-Generation Satellites XVI. 853318https://doi.org/10.1117/12.977560. 10 pp.

Xu, F., Ignatov, A., 2010. Evaluation of in situ sea surface temperatures for use in the calibration and validation of satellite retrievals. Journal of Geophysical Research: Oceans 115, C09022. https://doi.org/10.1029/2010JC006129.

Xu, F., Ignatov, A., 2014. In situ SST quality monitor (iQuam). J. Atmos. Ocean. Technol. 31, 164–180. https://doi.org/10.1175/JTECH-D-13-00121.1.

Yamaguchi, Y., Kahle, A.B., Tsu, H., Kawakami, T., Pniel, M., 1998. Overview of advanced spaceborne thermal emission and reflection radiometer (ASTER). IEEE Trans. Geosci. Remote Sens. 36, 1062–1071. https://doi.org/10.1109/36.700991.

Yamaguchi, Y., Fujisada, H., Kudoh, M., Kawakami, T., Tsu, H., Kahle, A.B., Pniel, M., 1999. ASTER instrument characterization and operation scenario. Adv. Space Res. 23, 1415–1424. https://doi.org/10.1016/S0273-1177(99)00293-8.

Yang, J., Zhang, Z., Wei, C., Lu, F., Guo, Q., 2017. Introducing the new generation of Chinese geostationary weather satellites, Fengyun-4. Bull. Am. Meteorol. Soc. 98, 1637–1658. https://doi.org/10.1175/bams-d-16-0065.1.

Závody, A.M., Mutlow, C.T., Llewellyn-Jones, D.T., 1995. A radiative transfer model for sea surface temperature retrieval for the along-track scanning radiometer. Journal of Geophysical Research: Oceans 100, 937–952. https://doi.org/10.1029/94JC02170.

Zeng, X., Beljaars, A., 2005. A prognostic scheme of sea surface skin temperature for modeling and data assimilation. Geophys. Res. Lett. 32, L14605. https://doi.org/10.1029/2005GL023030.

Zhang, H., Beggs, H., Majewski, L., Wang, X.H., Kiss, A., 2016a. Investigating sea surface temperature diurnal variation over the Tropical Warm Pool using MTSAT-1R data. Remote Sens. Environ. 183, 1–12.

Zhang, H., Beggs, H., Wang, X.H., Kiss, A.E., Griffin, C., 2016b. Seasonal patterns of SST diurnal variation over the Tropical Warm Pool region. Journal of Geophysical Research: Oceans 121, 8077–8094. https://doi.org/10.1002/2016JC012210.

Zhang, L., Shi, H., Du, H., Zhu, E., Zhang, Z., Fang, X., 2016c. Comparison of WindSat and buoy-measured ocean products from 2004 to 2013. Acta Oceanol. Sin. 35, 67–78. https://doi.org/10.1007/s13131-016-0798-9.

Zhang, H., Beggs, H., Merchant, C.J., Wang, X.H., Majewski, L., Kiss, A.E., Rodríguez, J., Thorpe, L., Gentemann, C., Brunke, M., 2018. Comparison of SST diurnal variation models over the Tropical Warm Pool region. Journal of Geophysical Research: Oceans 123, 3467–3488. https://doi.org/10.1029/2017jc013517.

Zhao, Y., Zhu, J., Lin, M., Chen, C., Huang, X., Wang, H., Zhang, Y., Peng, H., 2014. Assessment of the initial sea surface temperature product of the scanning microwave radiometer aboard on HY-2 satellite. Acta Oceanol. Sin. 33, 109–113. https://doi.org/10.1007/s13131-014-0402-0.

Zou, X., Zhuge, X., Weng, F., 2016. Characterization of bias of advanced Himawari imager infrared observations from NWP background simulations using CRTM and RTTOV. J. Atmos. Ocean. Technol. 33, 2553–2567. https://doi.org/10.1175/jtech-d-16-0105.1.